

















Cite this: DOI: 10.1039/d1qi00403d

New luminescent tetracoordinate boron complexes: an in-depth experimental and theoretical characterisation and their application in OLEDs†

Krishnamoorthy Paramasivam, ^{‡ a,h} Carina B. Fialho, ^{‡ a} Tiago F. C. Cruz, ^a Ana I. Rodrigues, ^a Bruno Ferreira, ^a Clara S. B. Gomes, ^{a,e,i} Diogo Vila-Viçosa, ^{§ c} Ana Charas, ^d José M. S. S. Esperança, ^e Luís F. Vieira Ferreira, ^f Maria José Calhorda, ^c António L. Maçanita, ^{a,b} Jorge Morgado ^{d,g} and Pedro T. Gomes ^{* a,b}

A group of new tetracoordinate mononuclear 2-(*N*-phenylformimino)pyrrolyl boron chelates [BX₂(κ²*N,N'*-NC₄H₃-2-C(H)=N-C₆H₅)] (X = F **3**; mesityl (2,4,6-trimethylphenyl, Mes) **4**; C₆F₅ **5**; X₂ = 1,1'-biphenyl-2,2'-diyl **6**) and the related binuclear complex [(C₆F₅)₂B(κ²*N,N'*-NC₄H₃-2-C(H)=N-C₆H₄-N=C(H)-C₄H₃-N-κ²*N,N'*)B(C₆F₅)₂] **7** were synthesised *via* metathetic exchange reactions of sodium 2-(*N*-phenylformimino)pyrrolyl with BF₃·Et₂O (**3**), BMes₂F (**4**) and 9-chloro-9-borfluorene (**6**), whereas **5** and **7** were obtained from the acid–base reactions between the corresponding neutral ligand precursors, respectively 2-(*N*-phenylformimino)pyrrole (**1**) and 1,4-(HNC₄H₃-C(H)=N)₂-C₆H₄ (**2**), with B(C₆F₅)₂OEt. These complexes were designed to evaluate the influence of the boron co-ligands on the molecular properties of the corresponding 2-iminopyrrolyl tetrahedral boron derivatives, particularly on luminescence. Compounds **3–7** were photophysically characterised in solution and in solid state, exhibiting blue to yellowish-green emissions and fluorescence quantum yields (ϕ_f) up to 0.40. The exception was complex **4**, which revealed full fluorescence quenching owing to a dynamic equilibrium involving the bidentate (tetracoordinate) 2-iminopyrrolyl boron complex and the corresponding monodentate (tricoordinate) species. DFT and TDDFT studies were carried out, considering the effect of solvent and also of dispersion forces, in order to elucidate the change in geometries of compounds **3–7** from the ground to the singlet excited state, to understand the dynamic equilibrium of **4**, to ascribe electronic transitions, and to rationalise the observed luminescence and also the main trends of thermal stabilities. These complexes were applied in organic light-emitting diodes (OLEDs), the ones based on complex **6** showing the best performances (maximum luminance of 170 cd m⁻² and electroluminescence efficiency of 0.037 cd A⁻¹).

Received 29th March 2021,

Accepted 10th May 2021

DOI: 10.1039/d1qi00403d

rsc.li/frontiers-inorganic

^aCentro de Química Estrutural, Instituto Superior Técnico, Universidade de Lisboa, Av. Rovisco Pais, 1049-001 Lisboa, Portugal. E-mail: pedro.t.gomes@tecnico.ulisboa.pt

^bDepartamento de Engenharia Química, Instituto Superior Técnico, Universidade de Lisboa, Av. Rovisco Pais, 1049-001 Lisboa, Portugal

^cBioISI - Biosystems & Integrative Sciences Institute, Departamento de Química e Bioquímica, Faculdade de Ciências, Universidade de Lisboa, Campo Grande, Ed. C8, 1749-016 Lisboa, Portugal

^dInstituto de Telecomunicações, Av. Rovisco Pais, 1049-001 Lisboa, Portugal

^eLAQV-REQUIMTE, Departamento de Química, Faculdade de Ciências e Tecnologia, Universidade NOVA de Lisboa, 2829-516 Caparica, Portugal

^fBSIRG – Biospectroscopy and Interfaces Research Group, IBB-Institute for Bioengineering and Biosciences, Instituto Superior Técnico, Universidade de Lisboa, 1049-001 Lisboa, Portugal

^gDepartment of Bioengineering, Instituto Superior Técnico, Universidade de Lisboa, Av. Rovisco Pais, 1049-001 Lisboa, Portugal

^hCentre for Environmental Research, Department of Chemistry, Kongu Engineering College, Perundurai, Erode 638 060, India

ⁱUCIBIO-REQUIMTE, Departamento de Química, Faculdade de Ciências e Tecnologia, Universidade NOVA de Lisboa, 2829-516 Caparica, Portugal

† Electronic supplementary information (ESI) available. CCDC 2073567–2073570. For ESI and crystallographic data in CIF or other electronic format see DOI: 10.1039/d1qi00403d

‡ These authors contributed equally.

§ Current address: Kinetikos, Coimbra, Portugal.

Introduction

The design of organic electroactive and photoactive materials has been greatly focussed on their potential applications in electronic and optoelectronic devices, which include thin film transistors, electroluminescent (EL) devices, such as organic-light emitting diodes (OLEDs), photovoltaic devices, solid-state lasers, *etc.*¹ Despite OLEDs being presently applied in commercially available flat panel displays and general lighting technology, there is a permanent search for improvements aiming at better stability, brightness, flexibility, and lower energy consumption and production costs.

The first studies on multi-layered OLEDs were carried out using AlQ₃ (HQ = 8-hydroxyquinoline) as emissive layer.² Subsequently, OLEDs based on phosphorescent or fluorescent chromophores, or the more recent generation of chromophores exhibiting thermally activated delayed fluorescence (TADF), have been developed.³ Among these emitters, tricoordinate boron complexes are an important class of luminescent chromophores.⁴ More recently, tetracoordinate boron complexes, containing bidentate *N,N*-, *N,O*-, *N,C*-, *C,C*-, *C,O*- and *O,O*-ligands, have also proved to be important luminescent chromophores.^{5,6}

Selected examples of tetracoordinate boron chromophores that have been used in emissive layers of OLEDs are presented in Chart 1. A series of bisphenyl boron 2-pyridyl-pyrrolyl derivatives (**A**, Chart 1) are notable examples of boron complexes containing bidentate *N,N*-ligands, having yielded OLEDs with maximum external quantum efficiencies (EQE_{max}) and luminances (*L*_{max}) as high as 0.5% and 5000 cd m⁻².^{5g} Bisphenyl boron complexes of *N,O*-chelates, such as 8-hydroxyquinolinate ligands reported by Slugovc *et al.* (**B**, Chart 1), exemplify tetracoordinate boron compounds that gave rise to OLEDs with *L*_{max} values as high as 1000 cd m⁻².⁷ Boron difluoride dipyrromethene (BODIPY) derivatives (**C**, Chart 1) have been applied as emissive layers of OLEDs, achieving EQE_{max} and *L*_{max} values as high as 2.3% and 3900 cd m⁻², respectively.⁸ Liu *et al.* described tetracoordinate bisfluoride boron compounds containing *N*-arylanilido-arylamine ligands (**D**, Chart 1), which were used in OLEDs exhibiting *L*_{max} values up to 1460 cd m⁻².⁹

The recent use of tetracoordinate boron chromophores exhibiting TADF have led to remarkable EQE_{max} values (between 4.8 and 26.6%),^{3z} the highest being determined for a boron compound containing an aryl-pyridine *N,C*-chelate framework (**E**, Chart 1).^{3w} By introducing aromatic amine *para*-

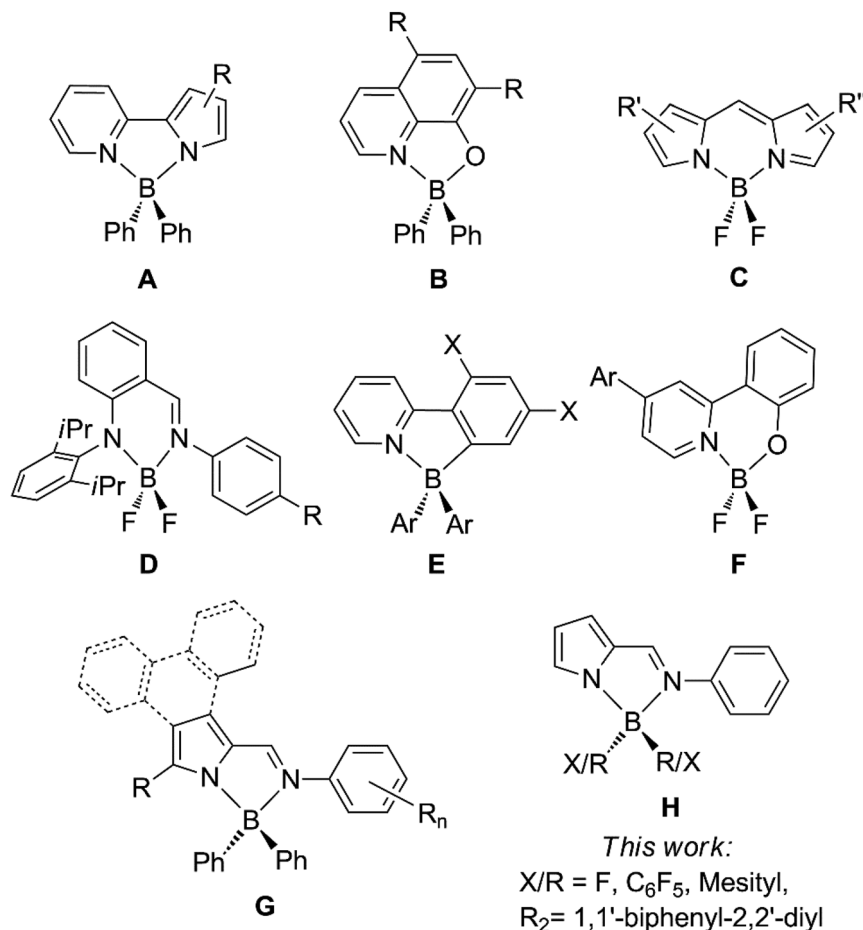


Chart 1 Selected examples of tetracoordinate boron complexes utilized as emissive layers of OLEDs.

substituents in the phenyl groups of the boron 2-pyridyl-pyrrolyl derivatives **A** mentioned above, the same authors (Chou and co-workers) could detect TADF behaviour while improving EQE_{max} values (as far as 13.5%).^{5m} Another example of multi-layered TADF-based OLEDs was reported by Deng and co-workers, which was fabricated with boron difluoride complexes of *N,O*-phenoxy-pyridyl chelating ligands as emitters (**F**, Chart 1), reaching EQE_{max} and *L*_{max} values such as 11.0% and 19 383 cd m⁻², respectively.^{6m}

Over the past few years, our group has been involved in the synthesis of a variety of metal complexes using 2-iminopyrrolyl derived *N,N*-chelating ligands, for which TADF was not identified. In particular, we reported luminescent zinc complexes containing the 2-formylphenanthro[9,10-*c*]pyrrole ligand precursor.¹⁰ Subsequently, we addressed the synthesis and luminescent properties of several tetracoordinate organoboron complexes containing 2-iminopyrrolyl ligands with varied electronic, skeletal and steric features reflected in their structures and properties (**G**, Chart 1).¹¹ The colour of emission of boron complexes bearing 2-iminopyrrolyl ligands could be tuned from violet-blue to orange, with quantum yields of emission as high as 71%. When used in emissive layers of OLEDs such compounds exhibited EQE_{max} and *L*_{max} values as high as 2.8% and 23 530 cd m⁻², respectively.

In the literature of common organoboron dyes, it was found that the presence of B-F bonds causes some instability under irradiation and sensitivity to polar solvents. Hence, many BODIPY derivatives have been prepared by replacing fluoride ligands with aryl, ethynylaryl, ethynylthienyl, *etc.* groups,¹² which improved their stability and produced large Stokes shifts. Chujo and co-workers¹³ found that bis(pentafluorophenyl)boron diketone analogues showed better photoluminescence performance than the respective simple bisphenyl boron derivatives. The 9-borafluorene rigid scaffold, considered to be a better Lewis acid than the B(C₆H₅)₂ fragment, may also improve thermal stability, emission quantum yield and charge carrier mobilities relative to the diphenylboron analogues.¹⁴

All our previously reported tetracoordinate 2-iminopyrrolyl boron molecules (**G**, Chart 1) were bisphenyl boron derivatives displaying relevant luminescent properties. In the present work, we modify the nature of the boron co-ligands and evaluate their influence on the molecular properties of the corresponding iminopyrrolyl boron derivatives, namely on luminescence. Thus, this paper reports the synthesis and structural characterisation of mononuclear 2-(*N*-phenylformimino)pyrrolyl organoboron complexes containing the highly electron-withdrawing fluoride and pentafluorophenyl co-ligands (BF₂ and B(C₆F₅)₂, respectively), the sterically hindered and electron-donating mesityl (2,4,6-trimethylphenyl, Mes) co-ligand (BMes₂) or the highly rigid and planar 1,1'-biphenyl-2,2'-diyl bidentate co-ligand (9-borafluorene-9-yl) (see **H**, Chart 1, and also Scheme 1). We also synthesised a binuclear bis(pentafluorophenyl)boron derivative containing two 2-iminopyrrolyl chelating fragments linked through a phen-1,4-diyl aromatic bridge. The thermal, photo- and electroluminescent properties

of these complexes were studied and compared with their previously reported analogues containing B(C₆H₅)₂ fragments.^{11a-d} DFT and TDDFT calculations helped to understand not only geometrical changes in solution or upon excitation from the ground to the singlet states, and the nature of the absorption and emission bands, but also the main trends of thermal stabilities.

Results and discussion

Synthesis and characterization of mono- and binuclear iminopyrrolyl boron complexes

New mono- and binuclear organoboron complexes containing 2-(*N*-phenylformimino)pyrrolyl ligands along with various co-ligands, such as bis(fluoride), bis(pentafluorophenyl), bis(mesityl) and 1,1'-biphenyl-2,2'-diyl were synthesised.

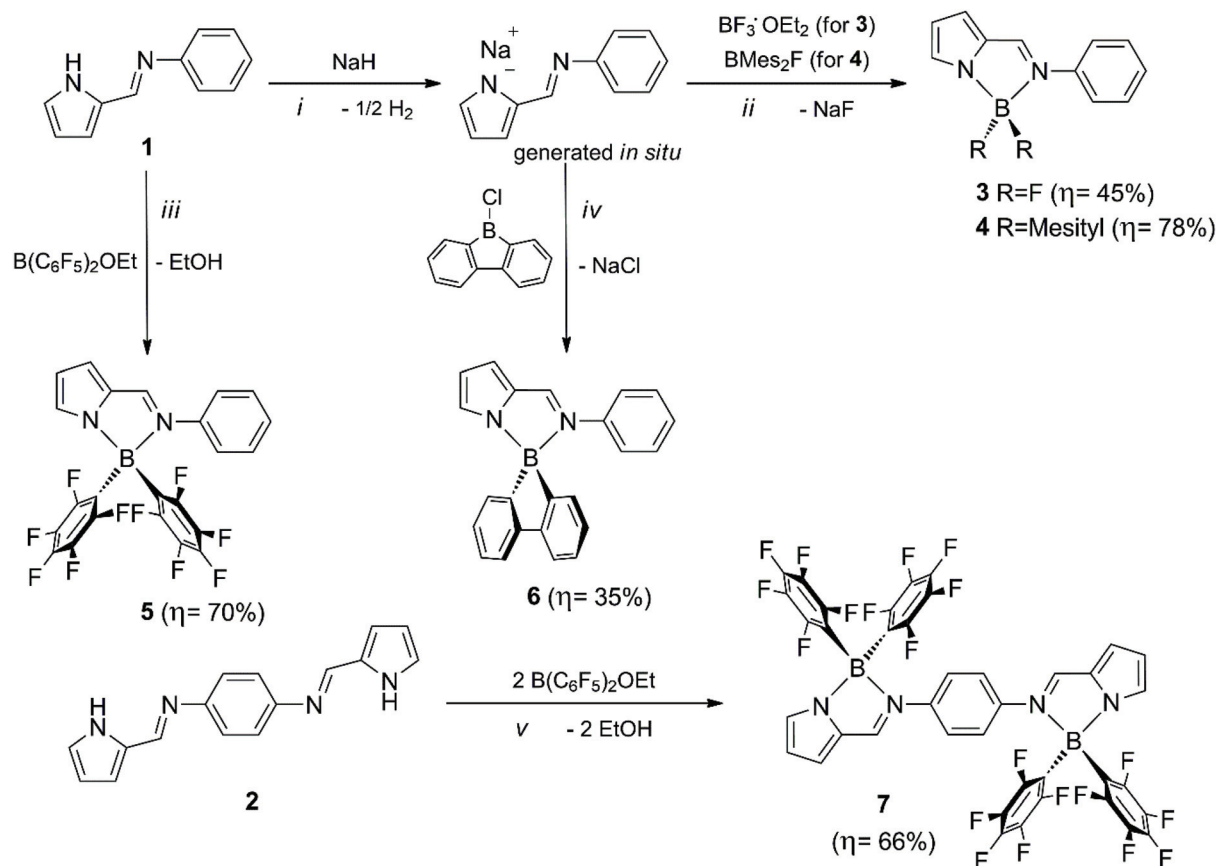
The target tetracoordinate boron compounds **3–7** were obtained by reaction of the 2-(*N*-phenylformimino)pyrrolyl ligand precursor **1**, or its corresponding pyrrolyl sodium salt, and the bis(2-formiminopyrrole) ligand precursor **2** with different boron starting materials (Scheme 1).

The synthesis of complexes **3**, **4** and **6** started with the *in situ* deprotonation of the NH proton of the 2-(*N*-phenylformimino)pyrrolyl, using an excess of sodium hydride, in THF, at room temperature (Scheme 1).¹⁵ Then, the monoanionic ligand precursor reacted with one equivalent of boron trifluoride etherate (BF₃·Et₂O), dimesitylboron fluoride (BMes₂F) and 9-chloro-9-borafluorene,¹⁶ in THF, at low temperature, leading to the desired products **3**, **4** and **6**, respectively, as shown in Scheme 1. The boron compounds **5** and **7** were obtained by refluxing the 2-iminopyrrolyl ligand precursors **1** and **2**, respectively, with bis(pentafluorophenyl)boron ethoxide (B(C₆F₅)₂OEt)¹⁷ in toluene (Scheme 1).

The new yellow- to orange-coloured compounds were obtained in moderate to good yields, being stable towards air and moisture when in the solid-state, and at room temperature, and only very slightly air- and/or moisture-sensitive, when in THF solution. The only exception was compound **3** that revealed instability in solution, either in air or even under nitrogen (decomposing in *ca.* 5 min or overnight, respectively), and considerable air-sensitivity in solid-state and when dispersed in ZEONEX films, typically decomposing overnight. The compounds were structurally characterised in solid-state by elemental analyses and, when single crystals were obtained, by single crystal X-ray diffraction.

Organoboron complexes **8** and **9** (Chart 2)^{11a,c,d} were employed as reference compounds, practically in all the studies performed throughout this work, for comparison with the properties of the new complexes **3–7**.

A series of 2-(*N*-arylformimino)-3,4,5-trialkylpyrrolyl difluoroboron compounds, with applications in biological fluorescence imaging, which are structurally related to complex **3**, were recently reported as being synthesised by a similar method but using DBU (1,8-diazabicyclo[5.4.0]undec-7-ene) as the base.^{6a} The alkyl substitutions at the 3, 4 and 5 pyrrolyl



Scheme 1 Synthesis of 2-iminopyrrolyl boron complexes **3–7**. Conditions: (i) THF, 1 h, rt; (ii) THF, ca. 12 h, -20°C to rt; (iii) toluene, reflux, ca. 12 h; (iv) toluene, reflux, ca. 12 h; (v) THF, ca. 12 h, -20°C to rt.

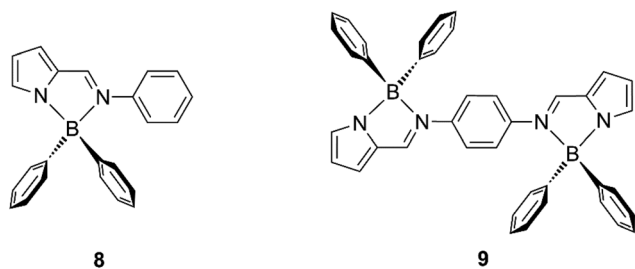


Chart 2 Mono- and binuclear diphenylboron compounds, **8**^{11a,c} and **9**^{11a,d} respectively, employed as reference compounds in this work.

ring positions seem to stabilise these BF_2 -based molecules in comparison to the unstable behaviour observed for complex **3** in the present work, both in solution and in solid-state. The NMR data are very similar to **3** but no X-ray characterization was presented.

Crystals suitable for single crystal X-ray diffraction studies were obtained for compounds **3**, **4** and **7**, their molecular structures being shown in Fig. 1 (the remaining molecules of the asymmetric unit are depicted in Fig. S1–S3 of the ESI[†] respectively). The molecular structure of **6** was also determined but, although it is the first crystalline structure of a mono-

nuclear 2-iminopyrrolyl organoboron complex containing a 9-borafluorenyl bidentate co-ligand, its diffraction data is of poor quality. The pictures displayed in Fig. S4 and S5 of the ESI[†] is a proof of its atom-bond connectivity (confirmed by DFT calculations). Selected bond distances (\AA) and angles ($^\circ$) of these four complexes are listed in Table S1 (ESI[†]), and crystal data and structure refinement parameters for the four compounds are presented in Table S2 of the ESI[†].

The coordination of the 2-(*N*-phenylformimino)pyrrolyl or bis[pyrrolyl-2-formimino-*N*]phen-1,4-diyl ligands *via* N1, N2 to the boron centres in a monoanionic fashion leads to five-membered chelate rings. The *N,N'*-2-iminopyrrolyl chelating ligands and the boron centre are co-planar, the corresponding co-ligands being located above and below that plane. The boron atoms in compounds **3** and **6** display almost perfect tetrahedral geometries, with dihedral angles between N1–B1–N2 and E1–B1–E2 planes (E1 = F1, C13 and E2 = F2, C19, in **3** and **6**, respectively) of $91.13(12)^\circ$, $90.4(3)^\circ$ and $89.2(3)^\circ$, for complexes **3** and **6**, molecule A and B, respectively (see dihedral angles $\omega_{(B1)}$ in Table S1, in ESI[†]). Consequently, the 2-(*N*-phenylformimino)pyrrolyl ligand in compound **6** is nearly orthogonal to its corresponding 9-borafluorenyl moiety. On the other hand, compounds **4** and **7** display considerable and slight tetrahedral distortions, respectively, with dihedral angles of

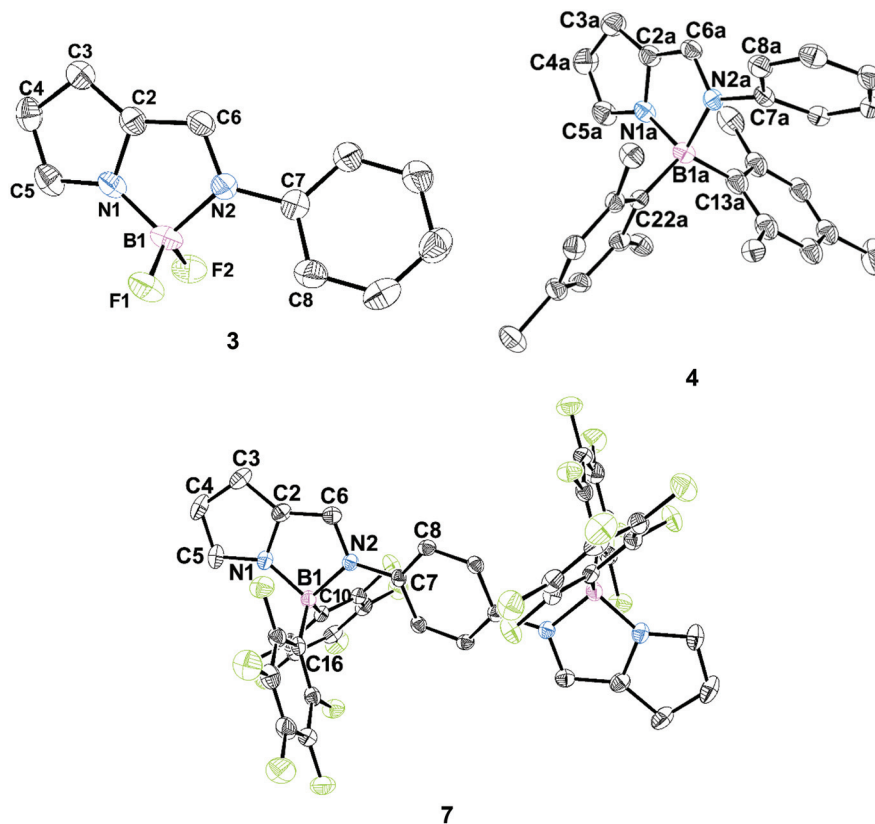


Fig. 1 Perspective views of the molecular structures of 2-iminopyrrolyl boron complexes **3**, **4** (molecule A) and **7**, using 50% probability level ellipsoids. All calculated hydrogen atoms and the diethyl ether solvent molecule of **7** were omitted for clarity.

77.27(8)–79.05(7)°, in **4**, and 85.81(6)°, in **7** (Table S1, in ESI†). The average bond distances between the boron centre and the two chemically different nitrogen atoms, B1–N1_{pyrrolyl} and B1–N2_{imine}, which range from 1.537(5)–1.592(10) Å and 1.602(2)–1.682(2) Å, respectively, reflect the bulkiness of the co-ligands (in the order **4** > **6** > **7** > **3**), the lowest values being quite comparable to those of the previously reported 2-iminopyrrolyl organoboron compounds (B1–N1_{pyrrolyl} with distances of 1.5687(18) and 1.562(3) Å, and B1–N2_{imine} bond lengths of 1.6327(19) and 1.632(3) Å, for compounds **8** and **9**^{11a}, respectively).¹¹ A remarkable feature in complex **4** is its B1–N2_{imine} bond distance, which is significantly longer (by 0.04–0.12 Å) than those observed for **3**, **6** and **7**, or for the other similar reported structures ($\Delta(\text{B1–N2}_{\text{imine}})$ of 0.02–0.05 Å for both compounds **8** and **9**^{11a}),¹¹ pointing to a much weaker chelation of the 2-iminopyrrolyl ligand to boron in this compound.

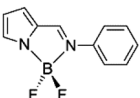
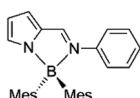
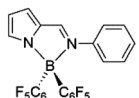
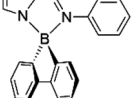
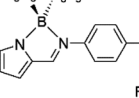
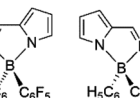
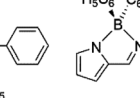
Moreover, the dihedral angles between the 2-formiminopyrrolyl fragment and the iminic *N*-phenyl ring, defined as C6–N2–C7–C12, are 24.0(5) for **3**, 19.3(10) and 22.6(11) for compound **6** (molecules A and B, respectively) and 14.9(2)° for the binuclear compound **7**, being much lower than those of compound **4**, and lying in the range *ca.* 52–61° (see C6–N2–C7–Cx, and also $\varphi(\text{Pyrr-Ph})$, in Table S1, in ESI†). These larger dihedral angles observed in **4** are due not only to the steric hindrance imposed by the mesityl groups, but also to the intra- and intermolecular interactions that generate the supramolecular

arrangement in the structure, consisting of intramolecular C–H⋯N and intra- and intermolecular C–H⋯ π short contacts.

Thermogravimetric analysis (TGA) was performed on the boron chelates **3–9** up to 500 °C affording the weight loss curves shown in Fig. S6 (compounds **3**, **4**, **5**, **6** and **8**) and S7 (binuclear compounds **7** and **9**), in ESI.† To evaluate the thermal stability of the boron compounds, two decomposition temperatures were calculated: $T_{\text{dec } 1\%}$, representing the temperature at which 1% of the initial mass is lost, and $T_{\text{dec } 5\%}$, the temperature at which 5% of the initial mass is lost. The calculated decomposition temperatures of the boron chelates **3–9** are presented in Table 1.

The decomposition temperatures $T_{\text{dec } 5\%}$ of the mononuclear compounds follow the order **4** < **3** < **6** < **8** < **5**, slightly different from the order of $T_{\text{dec } 1\%}$ values, due to the distinct decomposition patterns of the boron compounds studied. The experimental results indicate two-stage decomposition mechanisms for the BF₂ complex **3** (with loss of C₆H₅ and F fragments in the first and second stages, respectively), the dimesityl boron complex **4** (with loss of a BMe₂ fragment in the first stage), the binuclear B(C₆F₅)₂ complex **7**, and for the reference B(C₆H₅)₂ binuclear complex **9** (with loss of C₆H₅ and B(C₆H₅)₂ fragments in the first and second stages, respectively). Complexes **5**, **6** and reference B(C₆H₅)₂ mononuclear **8** follow a one-step degradation process.

Table 1 Decomposition temperatures ($T_{\text{dec } 1\%}$ and $T_{\text{dec } 5\%}$) of complexes 3–9

							
	3	4	5	6	7	8	9
$T_{\text{dec } 1\%}$ (°C)	106	104	163	102	216	121	99
$T_{\text{dec } 5\%}$ (°C)	127	117	206	168	278	187	104

The bis(pentafluorophenyl) boron ($\text{B}(\text{C}_6\text{F}_5)_2$) mononuclear complex 5 presents a decomposition temperature higher than the corresponding hydrogenated $\text{B}(\text{C}_6\text{H}_5)_2$ mononuclear reference complex 8, while the fluorinated binuclear complex 7 shows a marked increase in the decomposition temperature compared with the non-fluorinated binuclear boron complex 9. Hence, these results indicate that the bis(pentafluorophenyl) boron complexes are much more thermally stable than the simple bis(phenyl) substituted boron complexes. The BF_2 complex 3, containing simple fluorides as co-ligands and the boron complex 4, containing mesityl co-ligands, present much lower decomposition temperatures, while the boron complex 6 displays intermediate values. In most of the cases, except for the BF_2 complex 3 and the binuclear complexes 7 and 9, there is an almost complete weight loss (higher than 90%).

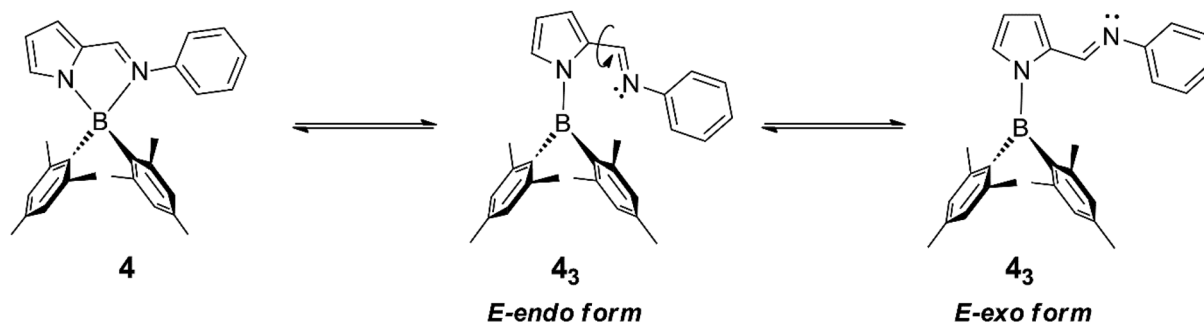
In order to interpret the previous trends, a study of the binding energies between the 2-iminopyrrolyl ligand and the boron diaryl fragment was carried out using DFT calculations and an Energy Decomposition Analysis.^{18,19} Complex 4 has the smallest binding energy in agreement with its fragmentation pattern described above. In all the other complexes, the higher binding energies probably lead to other decomposition pathways (for the complete analysis, see ESI, Table S3† and text).

In solution, the new 2-iminopyrrolyl boron complexes were characterised by multinuclear NMR spectroscopy (^1H , ^{13}C , ^{11}B , and ^{19}F), in CD_2Cl_2 (Fig. S8–S27, ESI†). The formation of the mono- and binuclear boron complexes was confirmed by the absence of NH proton resonances of the iminopyrrole precursors. The ^{11}B NMR spectra show resonances of compounds 3, 5, 6 and 7 in the range -1.4 to $+3.6$ ppm, consistent with those of other tetracoordinate boron derivatives,^{5,6,11,20} namely with those of reference compounds 8 (4.9 ppm^{11a,c}) and 9 (5.5 ppm^{11a,d}), since ^{11}B NMR resonances of tricoordinate boron complexes appear downfield shifted in the region *ca.* 25 ppm and above.^{4,20} However, the complex $[\kappa^2\text{N},\text{N}'\text{-}2\text{-(N-phenylformimino) pyrrolyl}]\text{BMe}_2$ (4) presents a broad resonance at 15.6 ppm ($\Delta\nu_{1/2} = 296$ Hz), in CD_2Cl_2 , considerably downfield shifted in relation to the normal range of tetracoordinate boron complexes, and located in between the values exhibited by tri- and tetracoordinate boron complexes. Contrasting with the other new complexes 3 and 5–7, a close inspection of the ^1H NMR spectrum reveals the presence of minor peaks of another 2-iminopyrrolyl boron dimesityl compound, the integration of

which corresponds to *ca.* 7 mol% of the mixture of minor and major species present in solution. This set of minor resonances appears in the ^1H NMR spectrum irrespective of using different preparative batches or recrystallisation attempts of 4, meaning they correspond to a different isomer of tetracoordinate complex 4, involved in an equilibrium process with the latter.

The interconversion between the two isomers was not clear-cut at first glance in a variable-temperature (VT) ^1H NMR experiment, performed in $\text{THF-}d_8$ and between 30 and 70 °C, because the variation in the relative areas was very small (Fig. S26, ESI†). However, remarkable evidence for the existence of a dynamic chemical exchange process between the two species in equilibrium is obtained in: (a) the VT- ^{11}B spectra (Fig. S27, ESI†), displaying a clear progressive downfield shift of the broad ^{11}B resonance of tetracoordinate complex 4 from 12.9 ppm, at 30 °C, to 21.6 ppm, at 70 °C (with $\Delta\nu_{1/2}$ varying from 327 to 254 Hz, respectively); this is concomitant with a slight sharpening of another much smaller broad resonance present at higher chemical shifts typical of a tricoordinate boron $[\kappa^1\text{N}'\text{-}2\text{-(N-phenylformimino)pyrrolyl}]\text{BMe}_2$ species (4_3), progressively shifting upfield with temperature from 50.3 to 48.9 ppm; and (b) 1D-NOE NMR experiments (Fig. S28 and S29, ESI†) performed while selectively irradiating the iminic $-\text{CH}=\text{N}-$ proton of one of the isomers and obtaining a negative exchange NOE peak for the same resonance of the other isomer, undeniably indicating the equilibrium between species 4 and 4_3 (Scheme 2). The coordination of a *N*-pyrrolyl ligand to a $\text{B}(\text{mesityl})_2$ fragment affording a tricoordinate complex has precedence in the literature since the related compound $[(\text{N-pyrrolyl})\text{BMe}_2]$ had been previously reported and characterised by IR, UV-Vis and Fluorescence spectroscopies.²¹

Integration of the ^1H NMR resonances of the iminic protons of both 4_3 and 4 afforded values of the equilibrium constant ($K = [4_3]/[4]$) at different temperatures. Fitting these data to the van't Hoff equation (Fig. S30, ESI†) led to the following thermodynamic parameters: $\Delta H^\circ = 0.49 \pm 0.04$ kcal mol⁻¹, $\Delta S^\circ = -3.4 \pm 0.1$ cal mol⁻¹ K⁻¹ and $\Delta G^\circ(298.15 \text{ K}) = 1.51 \pm 0.07$ kcal mol⁻¹. The structure(s) of the tricoordinate boron minor isomer(s) and the whole dynamic equilibrium were established by DFT calculations. The energy profile is shown in Fig. 2 (for details see also Scheme S1 and Fig. S31–S33 in ESI†). Calculated thermodynamic functions for the equilibrium between 4 and $4_{3\text{E-endo}}$ reveal that the enthalpies



Scheme 2 Schematic equilibrium between the tetracoordinate 2-iminopyrrolyl boron complex **4** and its tricoordinate isomer(s) **4₃**.

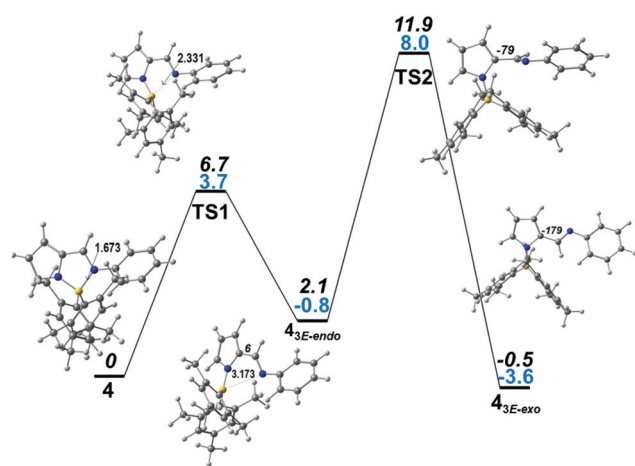


Fig. 2 Energy profile (BP86 functional) for the conversion of complex **4** into the tricoordinate complex **4_{3E-endo}** (elongation of the B–N_{imine} bond from 1.673 to 3.173 Å) and isomerisation to **4_{3E-exo}** (rotation around the internal C_{pyrrolyl}–C_{imine} bond of the 2-iminopyrrolyl ligand from 6 to –179°), with the relative energies (black) and Gibbs energies (blue) in kcal mol⁻¹, and the geometries of the five species with indication of the parameter changing in each step (distances in Å in TS1 and C–C–C–N dihedral angles in ° in TS2).

are in very good agreement, with 0.6 (calc.) and 0.5 (exp.) kcal mol⁻¹, while the Gibbs energies, –0.8 (calc.) and 1.5 (exp.) kcal mol⁻¹ differ a little more, despite being of the same order of magnitude. This not so good agreement is explained by the limitations in the calculations of the entropy.

The existence of this dynamic equilibrium between **4** and **4₃** is responsible for the different optical properties of complex **4** in comparison with those of the remaining complexes (see below in Photophysical studies).

Molecular geometries and electronic structures

DFT²² calculations (ADF program,²³ PBE0 functional, TZ2P basis set (method A, as used in recent publications,^{11g,h} more in Computational details), without any symmetry constraints, were used to optimise the structures of the ground and the first excited singlet state of all the new complexes **3–7**. The reference compounds **8** and **9**, which were initially calculated with a different methodology,^{11a-d} were also included. Other

approaches were tested, one of them including dispersion corrections, and their description was given in Computational details; the results appear in the ESI (Tables S4, S5, S6 and S8†). The ground state geometries were based on the crystal structure of the complexes described above (**3**, **4**, **6**, **7**) or modelled after them. The singlet excited states were obtained from a TDDFT optimization.²⁴ The structures are shown in Fig. 3 with the C6–N2–C7–C12 dihedral angle, the most relevant parameter (the values of the dihedral angles obtained with the other methods are collected in Table S4 in ESI†), and with the most relevant distances in Fig. S34 (3–6) and S35† (7–9).

These dihedral angles are in good agreement with the experimental values for the complexes with available structures: –24° (calc.), –24.0(5)° (exp.) for **3**; –49° (calc.), –52.2(2) to 61.8(2)° (exp., four independent molecules) for **4**; 30° (calc.), 19.3(10)°, –22.6(11)° (exp.) for **6**; and 22°, –22° (calc.), –14.9(2)° for the binuclear **7**. For the previously reported phenyl derivative **8** it was calculated as 36° and determined as –47.21(17),^{11a} while for binuclear **9** it was calculated as 31°, –31° and determined as 47.2(3)°.^{11a} The differences between calculated and experimentally determined values arise from the packing effects in the X-ray determined structures, mostly van der Waals interactions. In most complexes, the dihedral angle has a value around 30°, which drops to 22–24° for the three complexes with fluorine (**3**, **5**, **7**) and widens for **4** (49°) as a result of the bulkiness of the two 2,6-methyl substituents of the mesityl groups and increased repulsion with the iminopyrrolyl phenyl ring.

The angles between the planes N1–B1–N2 and E1–B1–E2 (E being fluorine in **3**, and carbon in **4**, **6** and **7**, see Table S1 in ESI†) were determined experimentally as 91.13(12)°, and calculated as 91° for **3**; 105.53(8)°, 100.95(7)°, 77.27(8)°, 78.16(7)° (exp.) and 79° (calc.) for **4**; 90.4(3)° and 89.2(3)° (exp.) and 92° (calc.) for **6**; 85.81(6)° (exp.) and 95° (calc.) for **7**. The comparison between the experimental and calculated values goes from perfect (**3**), to good (**6**), and to bad (**7**). The last example (**4**) is particularly interesting, since the angles of the C and D molecules are very well reproduced (within 1–2°), while those of A and B molecules are shifted by more than 20°. As mentioned above, these differences are assigned to intramolecular C–H⋯N and intra- and intermolecular C–H⋯π weak non-classical hydrogen bonds observed in the solid state for molecules C and D, providing a good example of the role of weak inter-

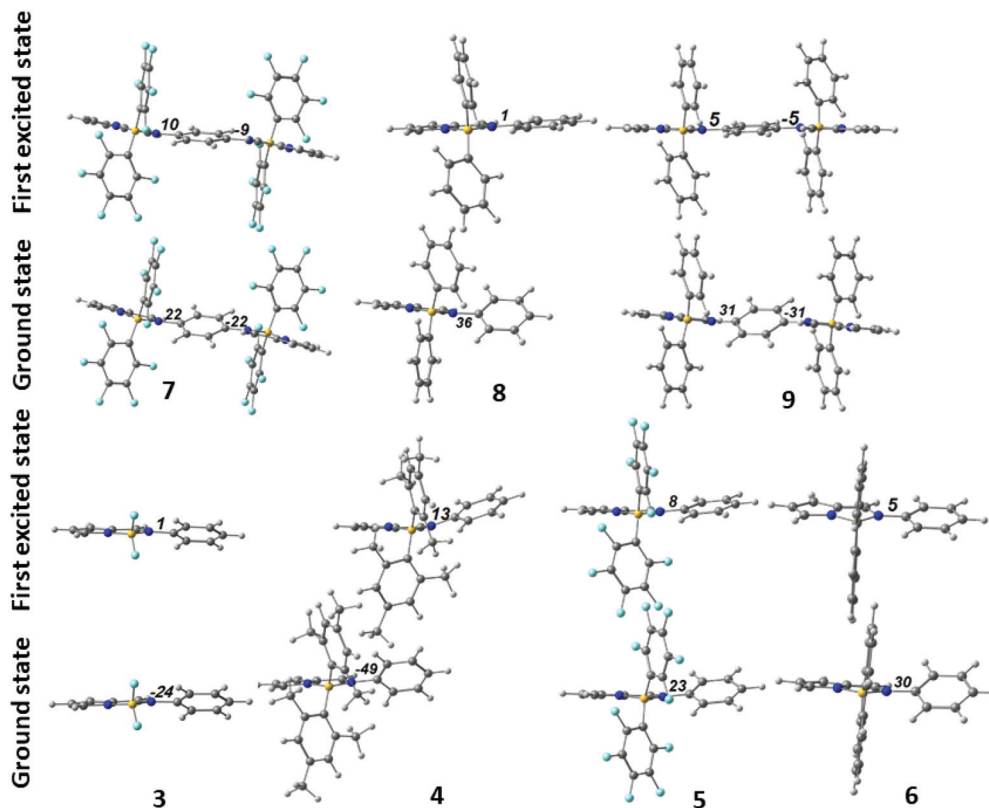


Fig. 3 Optimised geometries of the iminopyrrolyl boron complexes **3–9** in the ground state and in first excited singlet state, showing the C6–N2–C7–C12 dihedral angles (°).

actions in controlling the molecular structure but not considered in our model (single molecule).

In the singlet excited state, there is a tendency for the bidentate ligand to become planar, as observed in **8** and **9**, with calculated angles of 3° and 5°, respectively. Similar to these are the values for **3** (1°), **5** (8°), **6** (5°), while there is a small increase in **4** (12°) and **7** (10°, –9°). The flattening of the iminopyrrolyl in **4** is remarkable. Indeed, in the first singlet state of boron complexes with substituents such as Me, *i*Pr, Br or I in the *ortho* positions of the *N*-phenyl, the iminopyrrolyl is far from planar, though a bit less than in the ground state, owing to the repulsion with the N=C–H group.^{11c,e,g,h} However, in **4**, the stereochemical hindrance of the BMe₂ mesityl groups does not have a significant effect on the geometry of the iminopyrrolyl ligand, which lies far away (see Fig. S34, ESI†).

The experimental B–N_{pyrrolyl} distances are slightly shorter than the B–N_{imine} distances, differing in general by a small amount (~0.06 Å). However, in compound **4** the two values are 1.584 Å and 1.659 Å, this B–N_{imine} bond being the longest (all the distances are shown in Fig. S34 (ESI†)). Interestingly, the B–N_{pyrrolyl} and the B–N_{imine} distances tend to be closer in singlet state for all compounds, being practically the same in **4** (1.585 and 1.590 Å; see Fig. S34 in ESI†). The bond length asymmetry is relevant, since **4** does not behave as the other species in solution (see above and in ESI†).

The HOMO and LUMO of complexes **3–9** are shown in Fig. 4 (see also Fig. S36† for the other relevant molecular orbitals of complexes **4** and **6** and Table S5† for the energies calculations with other methods).

The introduction of fluorine, in particular the substitution of H by F in the phenyl groups, leads to a general stabilization, reflected to a larger extent in the LUMOs. This results from the higher electronegativity of fluorine and, for complexes **5** and **7**, the possibility of fluorine participating in the π system of C₆F₅. The HOMOs and LUMOs of all complexes, with the exception of the HOMO of **6**, have similar nature, being localised in the iminopyrrolyl ligand. The HOMO of **6** is localised in the 9-borafluorenyl groups, but the HOMO–1 of complex **6**, on the other hand, is localised in the iminopyrrolyl (Fig. S36, ESI†). The HOMO of **4** barely extends to the phenyl group at the N_{imine} but has a small localization in the mesityl groups. They contribute a lot more to HOMO–1, HOMO–2, and HOMO–3 (Fig. S36, ESI†).

Photophysical studies

The photophysical properties of complexes **3–9** were studied in THF solutions and ZEONEX films (see Experimental section for details).

Fig. 5 shows the normalised absorption and fluorescence spectra. The absorption wavelength maxima ($\lambda_{\text{abs}}^{\text{max}}$) and the respective molar extinction coefficients (ϵ_{max}) of the new compounds (**3–7**), in THF solution, are listed in Table 2, along with

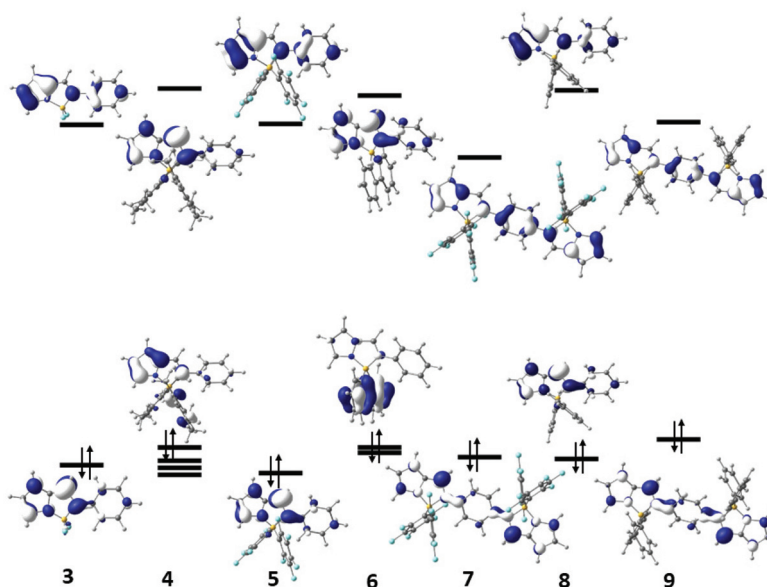


Fig. 4 Three-dimensional representation of the HOMO and LUMO of complexes 3–9 with relative energies (HOMO–LUMO gap: 4.05 (3), 4.24 (4), 4.06 (5), 4.09 (6), 3.54 (7), 4.26 (8) and 3.71 (9) eV; the HOMO is identified by the arrows).

data previously reported for reference compounds 8 and 9, as well as the $\lambda_{\text{abs}}^{\text{max}}$ values of all compounds in ZEONEX films. The ϵ_{max} values of the mononuclear complexes 3, 5, 6 and 8 in THF ($\approx 2 \times 10^4 \text{ L mol}^{-1} \text{ cm}^{-1}$) are typical of allowed $\pi\text{-}\pi^*$ electronic transitions (see below Table 2 and following discussion), as well as those of the binuclear complexes 7 and 9 ($\approx 3 \times 10^4 \text{ L mol}^{-1} \text{ cm}^{-1}$) and similar to those obtained in previous works.¹¹ However, no emission was observed for 4, whose absorption band appears at $\lambda_{\text{abs}}^{\text{max}} = 324 \text{ nm}$, much shorter than that of the reference compound 8 ($\lambda_{\text{abs}}^{\text{max}} = 383 \text{ nm}$). This fact can be attributed to the weak chelation of the 2-(*N*-phenylimino)pyrrolyl chromophore, which is involved in the dynamic equilibrium between bidentate (in 4) and monodentate (in 4₃) 2-iminopyrrolyl ligand coordination to boron described above (and in ESI†), which induces non-radiative decay, thus leading to fluorescence extinction. The calculated absorption spectra of 4_{3E-endo} and 4_{3E-exo} species, found at 339 and 355 nm (see below), probably overlapping with the absorption of 4, are close to that of the protonated ligand precursor 1¹⁰ (where the N_{imine} nitrogen is free).

The absorption wavelength maxima of the remaining mononuclear boron complexes (3, 5 and 6) are within the 393–402 nm range, significantly longer than that of their reference complex 8 (383 nm). Compounds 3 and 5, with strong electron withdrawing co-ligands, *i.e.* fluoride and pentafluorophenyl groups, exhibit the largest bathochromic shift (20 nm) with respect to complex 8. A similar effect of the pentafluorophenyl groups occurs with the binuclear complex 7 whose $\lambda_{\text{abs}}^{\text{max}} = 452 \text{ nm}$ is 26 nm red-shifted with respect to the non-fluorinated binuclear complex 9 ($\lambda_{\text{abs}}^{\text{max}} = 428 \text{ nm}$). These observations indicate that the compounds containing F or C₆F₅ co-ligands in their molecular architecture have no severe rotational restrictions in the C6–N2–C7–C12 dihedral angle, between the 2-formiminopyrrolyl and the aromatic *N*-phenylimine arm (see

3 and 7 in Fig. 1) in the S₀ → S₁ electronic transition, leading to a higher extension of π -conjugation in S₁ and, consequently, to longer absorption wavelength maxima.

The first vibronic transition wavelength ($\lambda_{\text{em}}^{0-0}$) of the mononuclear complexes emission band range from 455 nm (reference complex 8) to 467 nm (complex 3), while those of the binuclear complexes are longer: 512 nm for the reference complex 9 and 517 nm for complex 7, owing to the higher π -conjugation length of the chromophore.^{11a,d} In both cases fluorination substantially red-shifts the fluorescence, as it was observed with absorption. The fluorescence colours exhibited by the boron complexes 3–9 in solution are shown in Fig. 6.

The Stokes shift ($\Delta\lambda = \lambda_{\text{em}}^{0-0} - \lambda_{\text{abs}}^{\text{max}}$) is *ca.* 66 ± 3 nm for all complexes, except for the reference compound 9, which shows a much larger shift (86 nm). The larger change of the C6–N2–C7–C12 dihedral angle from the ground to the first singlet excited state, predicted by the theoretical calculations (31°–5° = 26° for 9 as compared with that of 7, 22°–10° = 12°, Fig. 2) seems to be the most probable cause.

In the ZEONEX films, both absorption and fluorescence spectra of the mononuclear boron compounds are generally slightly red-shifted (*ca.* 1–6 nm) with respect to those in THF, despite the decrease of the dielectric constant from THF ($\epsilon = 7.6$) to ZEONEX ($\epsilon = 2.5$), which by itself should cause blue-shifts. A possible reason is that the packing in the films causes a decrease of the torsional angles between the chromophoric moieties of the complexes, thus extending the π -delocalization and red-shifting the spectra. Identical observations were previously made with similar compounds.^{11h} However, in the case of binuclear compounds 7 and 9 blue-shifts are observed for absorption (3 and 12 nm, respectively).

The fluorescence quantum yields (Table 2) of the binuclear complexes in THF solution ($\phi_f = 0.36$ and 0.32 for 9 and 7,

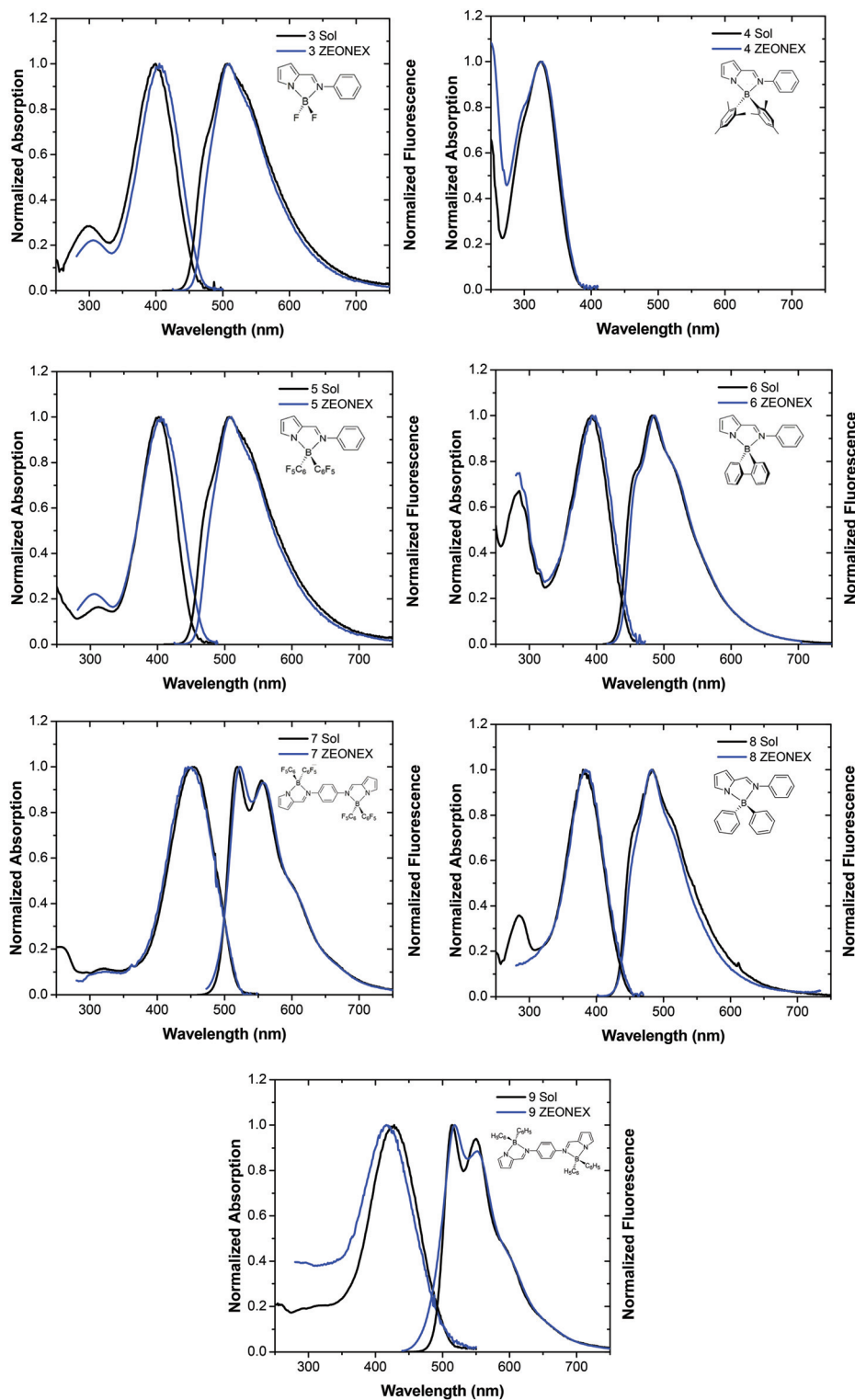


Fig. 5 Normalised absorption and emission spectra of complexes 3–9 in THF solution (black) and ZEONEX film (blue). The absorption in ZEONEX below 280 nm is not shown (absorption of ZEONEX).

respectively) are similar to those of the mononuclear complexes except that of 3 ($\phi_f = 0.14$). The boron complex 6, with a 9-borafluorenyl scaffold, has the highest fluorescence quantum yield ($\phi_f = 0.40$), owing to its lowest non-

radiative rate constant value ($k_{nr} = 1.9 \times 10^8 \text{ s}^{-1}$), close to those of the binuclear complexes. This may result from the limited flexibility of the bidentate ligand attached to boron.

Table 2 Wavelength maximum ($\lambda_{\text{abs}}^{\text{max}}$) and molar extinction coefficient (ϵ_{max}) of the first absorption band, wavelength maximum ($\lambda_{\text{em}}^{\text{max}}$) and wavelength of the first vibronic transition ($\lambda_{\text{em}}^{0-0}$) of the emission band, fluorescence quantum yield (ϕ_f), lifetime (τ_f), rate constant (k_f), and sum of non-radiative rate constants (k_{nr}) of boron complexes 3–9, in THF solution and ZEONEX films, at 293 K

Complex	Structure	Solution (THF)									Solid-state (ZEONEX 480 film)		
		$\lambda_{\text{abs}}^{\text{max}}$ (nm)	ϵ_{max}^a	$\lambda_{\text{em}}^{0-0}$ (nm)	$\lambda_{\text{em}}^{\text{max}}$ (nm)	$\Delta\lambda^b$ (nm)	ϕ_f	τ_f (ns)	k_f^c (ns^{-1})	k_{nr}^d (ns^{-1})	$\lambda_{\text{abs}}^{\text{max}}$ (nm)	$\lambda_{\text{em}}^{\text{max}}$ (nm)	ϕ_{PL}
3		399	1.97	467	507	68	0.14	1.20	0.12	0.72	405	510	0.17
4		324	1.63	<i>e</i>	<i>e</i>	<i>e</i>	<i>e</i>	<i>e</i>	<i>e</i>	<i>e</i>	325	<i>e</i>	<i>e</i>
5		402	1.60	466	494	64	0.32	2.15	0.15	0.32	405	497	0.31
6		393	2.08	461	483	68	0.40	3.1	0.13	0.19	394	486	0.40
7		452	3.13	519	519	67	0.32	2.14	0.15	0.32	449	522	0.31
8 ^f		383	1.73	451	479	68	0.34	1.90	0.18	0.35	383	482	0.37
9 ^g		428	3.00	512	512	84	0.36 ^h	2.2	0.16	0.29	416	518	0.36

^a $10^4 \text{ L mol}^{-1} \text{ cm}^{-1}$. ^b ($\Delta\lambda = \lambda_{\text{em}}^{0-0} - \lambda_{\text{abs}}^{\text{max}}$), Stokes shift. ^c $k_f = \phi_f/\tau_f$; ^d $k_{\text{nr}} = (1 - \phi_f)/\tau_f$; ^e Non-emissive; ^f From ref. 11a and c; ^g From ref. 11a and d; ^h Revised experimental value from ref. 11a and c.



Fig. 6 Fluorescence colours displayed by complexes 3–9 in THF under UV-irradiation at 365 nm.

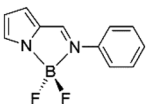
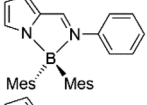
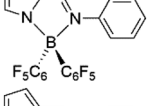
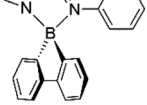
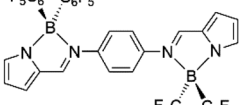
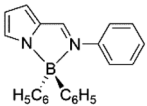
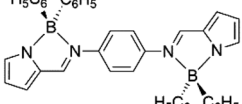
In the ZEONEX films, the photoluminescence quantum yields (ϕ_{PL}) are similar to ϕ_f in THF solutions within experimental error.

The electronic absorption spectra, emission energies and lifetimes of the first excited singlet state were calculated with

the TDDFT²⁴ methodology with the ADF program²³ (method A, PBE0 functional, TZ2P basis set, including the spin-orbit coupling effect). The relevant energies are collected in Table 3. Other approaches were tested, their description being given in Computational details; the results appear in Tables S6 and S8 in the ESI.†

The calculated absorption energies are generally higher than the experimental values, but in agreement with their trends (the energies calculated with other approaches are found in Table S6, ESI†). In particular, the lower energies of the binuclear complexes 7 and 9, and the high energy of 4, are well reproduced. The lower absorption energy in the electronic spectrum of the new complexes 3, 5, 7, as well as 8 and 9, with both HOMO and LUMO localised in the 2-iminopyrrolyl ligand, consists of one intense band resulting from a HOMO to LUMO transition (96–97%), being therefore described as a $\pi \rightarrow \pi^*$ (iminopyrrolyl) intraligand transition, as can be seen in the frontier orbitals shown in Fig. 4. The other two complexes,

Table 3 Calculated and experimental transition energy maxima (eV) of the lowest energy absorption band ($E_{\text{abs}}^{\text{max}}$) and of the emission band ($E_{\text{em}}^{\text{max}}$) of boron complexes **3–9** in solution

Complex	$E_{\text{abs}}^{\text{max}}$ (eV)		$E_{\text{em}}^{\text{max}}$ (eV)	
	Exp	Calc.	Exp.	Calc.
3 	3.08	3.36	2.50	2.57
4 	3.83	3.79	^a	2.37
5 	3.08	3.41	2.51	2.64
6 	3.15	3.50	2.57	2.57
7 	2.74	2.88	2.39	2.25
8 	3.25	3.45	2.58	2.70
9 	2.91	3.04	2.42	2.55

^a Non-emissive.

4 and **6**, differ, because the HOMO has a different composition (their frontier orbitals are shown in Fig. S36[†] and the compositions in Table S7, ESI[†]).

The HOMO of **4** is localised in the 2-iminopyrrolyl, but only slightly in the *N*-phenyl, and in one of the mesityl groups. The HOMO–1, HOMO–2, and HOMO–3 have similar compositions but with larger contributions of the B-phenyls and smaller of the 2-iminopyrrolyl. The LUMO is mainly in the bidentate ligand. Therefore, besides the $\pi \rightarrow \pi^*$ (iminopyrrolyl) intraligand transition, there is a π (mesityl) $\rightarrow \pi^*$ (iminopyrrolyl) component in this absorption band, calculated at 322 nm (3.79 eV) and observed at 324 nm (3.83 eV). The complex **4**_{3E-endo}, which was found to be in equilibrium with **4** (see Fig. 2 above and in ESI[†]), absorbs, according to the calculations, at 339 nm (3.62 eV) and **4**_{3E-exo} at 355 nm (3.49 eV). This observation may contribute to a broadening of the absorption band.

Complex **6** frontier orbitals are different, because the LUMO and the HOMO–1 are almost completely localised over the 2-iminopyrrolyl, while only the phenyl rings of the 9-bora-

fluorenyl rigid fragment contribute to the HOMO, which is thus almost orthogonal (see Fig. S36, ESI[†]). The lower energy absorption band, calculated at 354 nm (3.50 eV) and appearing at 393 nm (3.15 eV), is essentially a HOMO–1 to LUMO intraligand transition from $\pi \rightarrow \pi^*$ (iminopyrrolyl), with a HOMO to LUMO small component assigned to a π (9-borafluorenyl) $\rightarrow \pi^*$ (iminopyrrolyl) interligand transition (see composition in Table S7, ESI[†]). This feature has already been observed by Urban *et al.* in related tetracoordinate borafluorenyl 8-oxyquinolinato complexes,^{14d} and by Zhang *et al.* in the 2-(2-oxyphe-nyl)benzimidazolato derivative.^{14b}

The emission energies were obtained from the TDDFT optimization of the first excited singlet state. They compare relatively well with the experimental values (Table 3; emissions calculated using several methods are given in Table S8, ESI[†]) and the smaller energies correspond to the two binuclear complexes. Complexes **4** and **6** behave differently, as the oscillator strength for the excitation to the first singlet state is very weak, and only for the second singlet excited state is the value significant. This results from the nature of their frontier orbitals, which, as referred earlier, is different from the other complexes. The substitution of hydrogens by fluorines, leading from **8** to **5** and **9** to **7**, results in lower absorption and emission energies, as also discussed for the experimental values. The same tendency is observed in the BF₂ derivative **3**. The emission takes place from the LUMO to the HOMO in complexes **3**, **5**, **7–9**, and from the LUMO to the HOMO–1 in **6**. The role of HOMO–1 in the 9-borafluorenyl derivatives has already been emphasised by the authors referred above.^{14b,d} Complex **4** is in equilibrium with the tricoordinate complexes **4**_{3E-endo} and **4**_{3E-exo} as discussed previously. The absence of emission of the samples of **4**, in solution and in solid-state, can be explained by the low oscillator strength of the emission of this tetracoordinate complex (lower than for all the other complexes). These values become almost zero in the tricoordinate complexes in equilibrium.

Electrochemical studies

The ionisation potential (IP) and electron affinity (EA) of complexes **3–7** were determined from the onsets of the oxidation and reduction processes, respectively, measured by cyclic voltammetry, after correcting to the vacuum level (for which ferrocene was used as external reference). The obtained values were used to estimate the electron- and hole-injection barriers between the emissive layer and the electrodes in the OLED devices in which the complexes were applied.

The estimated values for IP and EA are summarised in Table 4, together with the energies of the HOMOs and LUMOs of the corresponding complexes calculated by DFT, with solvent correction (CH₂Cl₂), being compared with those previously obtained for the reference compounds **8** and **9**.^{11a,c,d} The corresponding voltammograms are shown in Fig. S37 in the ESI[†]. Complexes **5** and **7** showed remarkable electrochemical stability, as shown by the good reproducibility of successive reduction and oxidation cycles.

The values of -IP show a correlation with the energies of the HOMOs, although with IP values differing between 0.09 and

Table 4 Ionisation potentials (IP) and electron affinities (EA) values of complexes 3–9, estimated from cyclic voltammetry measurements in CH₂Cl₂, and the corresponding energies of HOMOs and LUMOs determined by DFT (CH₂Cl₂). All values in eV

Compound	Cyclic voltammetry		DFT (CH ₂ Cl ₂)	
	IP	EA	E_{HOMO}	E_{LUMO}
3	5.77	3.10	−5.63	−3.24
4	5.33	3.23	−5.42	−2.89
5	5.85	2.97	−5.69	−3.26
6	5.67	2.57	−5.45	−2.99
7	5.71	3.14	−5.51	−3.52
8	5.64 ^a	2.82 ^a	−5.51	−2.98
9	5.50 ^b	3.44 ^b	−5.31	−3.23

^a Values from ref. 11a and c. ^b Values from ref. 11a and d.

0.20 eV from the calculated ones (see Fig. S38a, in ESI†). The $-EA$ values also correlate with the calculated LUMO energies, with differences varying between 0.13 and 0.38 eV (see Fig. S38b, ESI†).

Electroluminescence studies

Several organic light-emitting diodes (OLEDs) structures were fabricated to assess the electroluminescence (EL) properties of complexes 5, 6, 7, 8, and 9 (see Table S9, ESI†). Fig. 7 shows the output characteristics of OLEDs based on these complexes dispersed (at 4% by weight) in poly(vinylcarbazole) (PVK). The corresponding emission spectra are shown in Fig. S39, ESI†. The performance of other devices is presented in the ESI (Fig. S40†).

PVK was chosen as host because it shows good hole-transporting properties, emits in the near-UV/blue region of the spectrum (EL maximum around 400 nm), therefore away from the compounds' emission spectral zone, and has a relatively low lying HOMO (reported values range from -5.8 to -5.4 eV (ref. 25)) and a high lying LUMO (reported in the range -2.3 to -1.9 eV (ref. 26)). Considering the IP and EA values determined from CV for these compounds (Table 4), PVK favours electron trapping at the boron complexes sites, though hole trapping is not anticipated to be that effective, in particular for the case of compound 5, which shows the highest IP (5.85 eV), indicating that its HOMO is lower than that of PVK. Dispersion was made in order to reduce electroluminescence concentration quenching by reducing/eliminating compounds aggregation. In these devices, a polyTPD interlayer (polyTPD_IL), *ca.* 5 nm thick, was used as hole-transporting/electron-blocking layer. PolyTPD has a reported HOMO energy of -5.2 to -5.4 eV, close to the PEDOT:PSS workfunction (5.2 eV), and a LUMO energy of -2.3 eV. Calcium was used as the cathode material, protected with an overlayer of aluminium.

All devices showed a light-onset voltage (taken as the voltage at which a minimum luminance of 10^{-2} cd m⁻² is detected) in the range 4–5 V (Fig. 7A). Compound 5 is the one leading to OLEDs with lower current and luminance (maximum luminance of 31 cd m⁻²), while the OLEDs based on compounds 6 and 9 show similar values of maximum lumi-

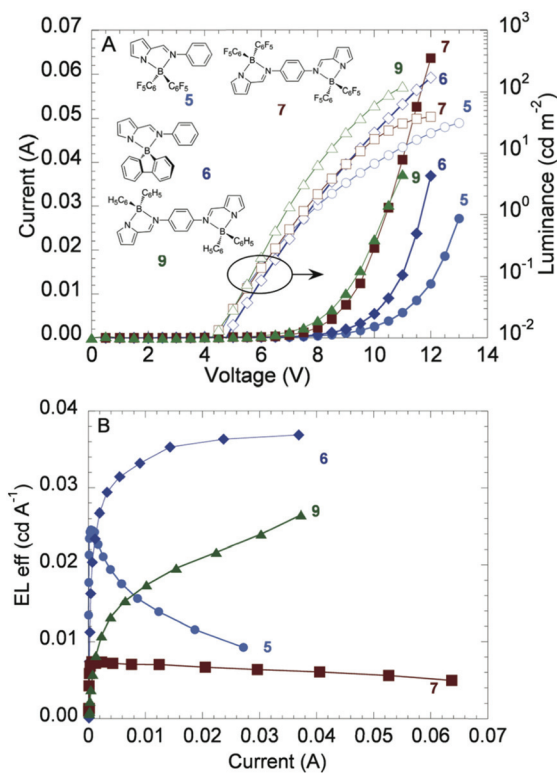


Fig. 7 (A) Current (filled symbols) and luminance (open symbols) of the OLEDs based on compounds 5, 6, 7 and 9, having the structure ITO/PEDOT:PSS/polyTPD_IL/PVK + 4%Comp/Ca/Al, active area of 8 mm², as a function of the applied voltage; (B) corresponding electroluminescence efficiency as a function of the current.

nance (170 and 124 cd m⁻², respectively). OLEDs based on compound 7 reach the highest current levels, though the maximum luminance is only 40 cd m⁻². This is translated into a lower luminance efficiency. OLEDs based on compound 6 show the highest efficiency (*ca.* 0.037 cd A⁻¹). Therefore, OLEDs based on this compound show the best overall performance. It also worth noting that the efficiency of the OLED based on compound 5 shows a fast decrease upon increase of the flowing current (Fig. 7B), a behaviour that contrasts with the relatively stable values at the highest current intensity of the OLEDs based on the other three compounds. This indicates that strong charge-induced exciton quenching occurs, a conclusion that is supported by the fact that devices based on neat 5 showed negligible emission.

In the emission spectra of these devices (Fig. S39, ESI†), there are small differences with respect to the corresponding photoluminescence (PL) spectra recorded in films of the complexes dispersed in ZEONEX, which we attribute mainly to interference effects.

The behaviour of the OLEDs based on binuclear complex 7 is different from those based on 9 (reference binuclear complex), not in terms of current–voltage dependence but in terms of luminance and efficiency. As they show similar PL efficiency, both in solution and solid-state, this difference in OLED performance can be due to stronger charge trapping on

9-based OLED as this complex has lower IP and higher EA (Table 4).

Overall, the OLEDs based on the new complexes **5**, **6** and **7** exhibit decent performances, with those based on **6** showing the highest maximum luminance and electroluminescence efficiency. It is worth noting that, among the three complexes, **6** is also the one showing the highest solid-state photoluminescence efficiency. The performance of these (simple) OLEDs is poorer when compared with other tetracoordinate boron complexes mentioned in the Introduction. However, device optimisation, involving the preparation by sublimation and the insertion of selective charge-transporting/blocking layers, should improve it, considering the high solid state fluorescence quantum yields of the new complexes.

Conclusions

A new set of tetracoordinate 2-iminopyrrolyl mononuclear boron complexes bearing different co-ligands (BX_2), of the type $[\text{BX}_2\{\kappa^2\text{N},\text{N}'\text{-NC}_4\text{H}_3\text{-2-C(H)=N-C}_6\text{H}_5\}]$ (BF_2 **3**; $\text{B}(\text{Mesityl})_2$ **4**; $\text{B}(\text{C}_6\text{F}_5)_2$ **5**, 9-borafluoren-9-yl **6**), and a binuclear $\text{B}(\text{C}_6\text{F}_5)_2$ derivative containing two 2-iminopyrrolyl chelating fragments linked through a phen-1,4-diyl aromatic bridge (**7**), were synthesised employing synthetic methodologies different from those previously reported for the $\text{B}(\text{C}_6\text{H}_5)_2$ analogues (**8** and **9**).^{11a,c,d} All these compounds, except **4**, are fluorophores revealing blue to yellowish-green emissions. The highly electron-withdrawing and ionic fluoride co-ligands of **3** (BF_2) impart considerable kinetic instability in solution and air-sensitivity in solid-state, along with the poorest fluorescence quantum yield of this series ($\phi_f = 0.14$). The sterically hindered and electron-donating 2,4,6-trimethylphenyl (mesityl) co-ligand of **4** (BMe_2) induces full fluorescence quenching owing to a dynamic equilibrium involving the tetracoordinate 2-iminopyrrolyl boron complex and the corresponding tricoordinate species, both assigned by NMR, in which the 2-iminopyrrolyl ligand coordinates to boron in bidentate or monodentate modes, respectively. DFT calculations show that the activation barrier to break the anomalously weak $\text{B-N}_{\text{imine}}$ bond of **4** is very small. Very likely owing to this reason compound **4** (followed very close by **3**) exhibits the lowest decomposition temperature in the series, as determined by TGA. The also highly electron-withdrawing but more covalent pentafluorophenyl co-ligand of **5** and **7** ($\text{B}(\text{C}_6\text{F}_5)_2$) confers high thermal stability to these compounds, which are by far those showing the highest decomposition temperatures, ca. 100 °C higher than those of the corresponding $\text{B}(\text{C}_6\text{H}_5)_2$ analogues **8** and **9**. Compounds **5** and **7** exhibit fluorescence quantum yields ($\phi_f = 0.32$), slightly below those of **8** and **9** ($\phi_f = 0.34\text{--}0.36$). The highly rigid and planar 1,1'-biphenyl-2,2'-diyl bidentate co-ligand of **6** (9-borafluoren-9-yl) imparts the highest fluorescence quantum yield ($\phi_f = 0.40$) and an intermediate thermal stability in this series of compounds. The DFT and TDDFT calculations show that the frontier orbitals involved in the absorption/emission processes of these compounds are similar in the case of **3**, **5** and **7** (and also for reference com-

pounds **8** and **9**), with both HOMO and LUMO localised in the 2-iminopyrrolyl ligand (essentially $\pi \rightarrow \pi^*$ (iminopyrrolyl) intraligand transitions), whereas in **6** there is basically a HOMO–1 to LUMO intraligand transition from $\pi \rightarrow \pi^*$ (iminopyrrolyl), with a HOMO to LUMO small component assigned to a π (9-borafluorenyl) $\rightarrow \pi^*$ (iminopyrrolyl) interligand transition. The thermally stable complexes **5**, **6** and **7** were tested in OLED devices, the films being prepared by spin coating. The OLEDs based on **6** showed the highest maximum luminance and electroluminescence efficiency (170 cd m^{-2} and 0.037 cd A^{-1} , respectively).

Experimental section

General procedures

All experiments were carried out under inert atmosphere of dinitrogen, using a dual vacuum/nitrogen line and standard Schlenk techniques. Nitrogen gas was supplied in cylinders by specialised companies (Air Liquide) and purified by passage through 4 Å molecular sieves. Unless otherwise stated, all reagents were purchased from commercial suppliers (e.g., Acros, Aldrich, Fluka) and used without further purification. All solvents to be used under inert atmosphere were thoroughly deoxygenated and dehydrated before use. They were dried and purified by refluxing over a suitable drying agent followed by distillation under nitrogen. The following drying agents were used: sodium/benzophenone (for toluene, diethyl ether, and tetrahydrofuran (THF)), calcium hydride (for *n*-hexane and dichloromethane). Solvents and solutions were transferred using a positive pressure of nitrogen through stainless steel cannulae and mixtures were filtered in a similar way using modified cannulae that could be fitted with glass fibre filter disks.

Nuclear Magnetic Resonance (NMR) spectra were recorded on Bruker Avance III 300 (^1H , 300.130 MHz; ^{13}C , 75.468 MHz; ^{11}B , 96.2712 MHz; ^{19}F , 282.404 MHz) or 400 (^1H , 400.130 MHz; ^{13}C , 100.613 MHz; ^{11}B , 128.3478 MHz; ^{19}F , 376.498 MHz) spectrometers. Deuterated solvents were dried by storage over 4 Å molecular sieves and degassed by the freeze–pump–thaw method. Spectra were referenced internally using the residual protio solvent resonances (^1H) and the solvent carbon (^{13}C) resonances relative to tetramethylsilane ($\delta = 0$), and referenced externally using 15% $\text{BF}_3\cdot\text{OEt}_2$ ($\delta = 0$) for ^{11}B , and CFCl_3 ($\delta = 0$) for ^{19}F . All chemical shifts are quoted in δ (ppm) and coupling constants given in hertz. Multiplicities were abbreviated as follows: broad (br), singlet (s), doublet (d), triplet (t), and multiplet (m). Samples were prepared in J. Young NMR tubes in a glove box. Elemental analyses were obtained from the IST elemental analysis services.

The ligand precursors, 2-(*N*-phenylformimino)pyrrole (**1**),²⁷ [pyrrole-2-formimino-*N*]₂-1,4- C_6H_4 (**2**)^{11d} and the boron precursors $\text{B}(\text{C}_6\text{H}_5)_3$,²⁸ $\text{B}(\text{C}_6\text{F}_5)_2\text{OEt}$ ¹⁷ and 9-chloro-9-borafluorene¹⁶ were synthesised according to literature procedures. Furthermore, the synthetic procedures and corresponding analytical data of the boron complexes $[\kappa^2\text{N},\text{N}'\text{-2-(N-C}_6\text{H}_5\text{-formimino)pyrrolyl}]\text{B}(\text{C}_6\text{H}_5)_2$ (**8**) and $\{(\text{C}_6\text{H}_5)_2\text{B}[\kappa^2\text{N},\text{N}'\text{-pyrrolyl-2-formimino-N-1,4-C}_6\text{H}_4\text{-}\kappa^2\text{N},\text{N}'\text{-2-formiminopyrrolyl}]\text{B}(\text{C}_6\text{H}_5)_2\}$ (**9**) were reported in our earlier publications.^{11a,c,d}

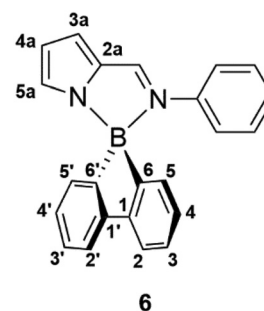
Syntheses of mono- and binuclear organoboron complexes

[κ^2N,N' -2-(*N*-C₆H₅-formimino)pyrrolyl]BF₂ (3). A solution of 2-(*N*-phenylformimino)pyrrole **1** (0.170 g, 1 mmol), in THF (15 mL), was added to an excess of NaH, at room temperature. Then the precooled boron starting precursor, boron trifluoride diethyl etherate (BF₃·OEt₂) (0.213 g, 1.5 mmol) was added dropwise to the solution of sodium salt of **1**, at –20 °C, and stirred overnight in *ca.* 20 mL of THF, at –20 °C. All the volatiles were evaporated, followed by extraction of the residue with toluene (5–10 mL). Again, the whole volatiles were evaporated, followed by a new extraction with toluene (5–10 mL). The resulting solution was kept at –20 °C to afford complex **3** as a crystalline yellow solid. Yield: 0.098 g (45%). ¹H NMR (400 MHz, CD₂Cl₂): δ 8.40 (s, 1H, CH=N), 7.57–7.37 (m, 6H, *Ph* + *Pyrr*), 6.99 (s, 1H, *Pyrr*), 6.49 (s, 1H, *Pyrr*). ¹³C{¹H} NMR (100.61 MHz, CD₂Cl₂): δ 151.8, 139.7, 133.7, 133.0, 130.4, 128.5, 120.7, 119.8, 117.9. ¹¹B NMR (128.35 MHz, CD₂Cl₂): δ 3.5 (t, ¹J_{BF} = 88 Hz; Δν_{1/2} = 80 Hz). ¹⁹F{¹H} NMR (376.50 MHz, CD₂Cl₂): δ –156.8 (q, ¹J_{BF} = 32 Hz). Anal. calcd (%) for C₁₁H₉BF₂N₂: C, 60.60; H, 4.16; N, 12.85. Found: C, 60.00; H, 3.73; N, 12.77.

[κ^2N,N' -2-(*N*-C₆H₅-formimino)pyrrolyl]B(Mesityl)₂ (4). A solution of 2-(*N*-phenylformimino)pyrrole **1** (0.192 g, 1 mmol), in THF (15 mL), was added to an excess of NaH, at room temperature. The sodium salt solution was added to the boron starting precursor, dimesitylboron fluoride (BMes₂F) (0.192 g, 1 mmol), and stirred overnight in *ca.* 20 mL of THF. All the volatiles were evaporated, followed by extracting the residue with toluene (5–10 mL). Again, the whole volatiles were evaporated, followed by extracting with Et₂O (5–10 mL) and double layering with *n*-hexane. The resulting mixture was kept at –20 °C to afford complex **4** as a crystalline yellow solid. Yield: 0.326 g (78%). *Major isomer* (93%): ¹H NMR (300 MHz, CD₂Cl₂): δ 8.15 (s, 1H, CH=N), 7.25–7.20 (m, 4H, *Ph* + *Pyrr*), 7.07–7.01 (m, 3H, *Ph* + *Pyrr*), 6.68 (s, 4H, *Ph*_{mesityl}), 6.47–6.45 (m, 1H, *Pyrr*), 2.20 (s, 6H, CH₃), 1.93 (s, 12H, CH₃). ¹³C{¹H} NMR (75.47 MHz, CD₂Cl₂): δ 154.6, 141.4, 136.4, 133.2, 130.3, 129.2, 128.8, 127.5, 124.2, 117.1, 116.4, 23.8, 21.1. ¹¹B NMR (96.27 MHz, CD₂Cl₂): δ 14.3 (br, Δν_{1/2} = 296 Hz). *Minor isomer* (7%): ¹H NMR (300 MHz, CD₂Cl₂): δ 8.27 (s, 1H, CH=N), 7.36 (t, 2H, *Ph*, J_{HH} = 8.1 Hz), 7.26–7.15 (m overlapping with the *major isomer*, 2H, *Ph* + *Pyrr*), 6.80 (s, 4H, *Ph*_{mesityl}), 6.31 (m, 1H, *Pyrr*), 6.16 (br, 1H, *Pyrr*), 2.26 (s, 6H, CH₃), 2.24 (s, 12H, CH₃). ¹¹B NMR (96.27 MHz, CD₂Cl₂): δ 51.1 (very br). *Major isomer* (93%): ¹H NMR (300 MHz, THF-*d*₈, 30 °C): δ 8.38 (s, 1H, CH=N), 7.20–7.12 (m, 3H, *Ph* + *Pyrr*), 7.09–7.01 (m, 2H, *Ph* + *Pyrr*), 6.98 (m, 1H, *Pyrr*), 6.59 (s, 4H, *Ph*_{mesityl}), 6.37 (m, 1H, *Pyrr*), 2.14 (s, 6H, CH₃), 1.89 (s, 12H, CH₃). ¹¹B NMR (96.27 MHz, THF-*d*₈, 30 °C): δ 712.9 (br, Δν_{1/2} = 327 Hz). *Minor isomer* (7%): ¹H NMR (300 MHz, THF-*d*₈, 30 °C): δ 8.24 (s, 1H, CH=N), 7.29 (t, 2H, *Ph*, J_{HH} = 7.5 Hz), 7.21–6.93 (m overlapping with the *major isomer*, 3H, *Ph* + *Pyrr*), 6.73 (s, 4H, *Ph*_{mesityl}), 6.18 (m, 1H, *Pyrr*), 2.22 (s, 12H, CH₃), 2.21 (s, 6H, CH₃). ¹¹B NMR (96.27 MHz, THF-*d*₈, 30 °C): δ 50.1 (very br). Anal. calcd (%) for C₂₉H₃₁BN₂: C, 83.25; H, 7.47; N, 6.70. Found: C, 83.62; H, 7.91; N, 6.78.

[κ^2N,N' -2-(*N*-C₆H₅-formimino)pyrrolyl]B(C₆F₅)₂ (5). A mixture of B(C₆F₅)₂OEt (0.390 g, 1 mmol) and one equivalent of 2-(*N*-phenylformimino)pyrrole **1** (0.170 g, 1 mmol) in *ca.* 20 mL of toluene were heated to reflux overnight. The reaction mixture was brought to room temperature and all the volatiles were evaporated, followed by extracting the residue with Et₂O (5–10 mL) and double layering with *n*-hexane. The resulting mixture was kept at –20 °C to afford complex **5** as a microcrystalline yellow solid. Yield: 0.356 g (70%). ¹H NMR (300 MHz, CD₂Cl₂): δ 8.64 (s, 1H, CH=N), 7.37–7.24 (m, 6H, *Ph* + *Pyrr*), 7.14 (brs, 1H, *Pyrr*), 6.54 (brs, 1H, *Pyrr*). ¹³C{¹H} NMR (75.47 MHz, CD₂Cl₂): δ 151.5, 150.3 (br), 147.0 (br), 142.7 (br), 140.9, 139.4 (br), 136.2 (br), 135.8 (br), 135.6, 134.0, 130.2, 128.2, 121.0, 119.0, 118.8. ¹¹B NMR (96.27 MHz, CD₂Cl₂): δ –1.4 (Δν_{1/2} = 70 Hz). ¹⁹F{¹H} NMR (282.40 MHz, CD₂Cl₂): δ –134.17 (dd, J_{CF} = 16.7, J_{CF} = 9 Hz, 4F, *o*-C₆F₅), –156.81 (t, 2F, J_{CF} = 20.3 Hz, *p*-C₆F₅), –163.66 (m, 4F, *m*-C₆F₅). Anal. calcd (%) for C₂₃H₉BF₁₀N₂: C, 53.73; H, 1.76; N, 5.45. Found: C, 54.05; H, 1.96; N, 5.28.

[κ^2N,N' -2-(*N*-C₆H₅-formimino)pyrrolyl](9-borofluorene) (6). A solution of 2-(*N*-phenylformimino)pyrrole **1** (0.19 g, 1.2 mmol), in THF (15 mL), was added to an excess of NaH, at room temperature. The sodium salt was added to boron starting precursor, 9-chloro-9-borofluorene (0.15 g, 0.8 mmol), at low temperature (–80 °C). The resulting solution was stirred overnight in THF, and allowed to slowly warm up to room temperature. In the next day, the suspension was filtered and crystals suitable for X-ray diffraction of the desired product **6** were obtained from a toluene solution, kept at –20 °C. Yield, 0.09 g (35%). ¹H NMR (300 MHz, CD₂Cl₂): δ 8.67 (s, 1H, CH=N), 7.68 (d, ³J_{HH} = 9 Hz, 2H, H₂ + H_{2'}), 7.26 (dt, ³J_{HH} = 6 Hz, ⁴J_{HH} = 3 Hz, 2H, H₃ + H_{3'}), 7.15–7.11 (m, 3H, N-Ph-H_{meta} + Ph), 7.08–7.03 (m, 7H, H₄ + H_{4'} + H₅ + H_{5'} + Ph + H_{3a}), 6.91 (s, 1H, H_{5a}), 6.50 (m, 1H, H_{4a}). ¹³C{¹H} NMR (75.47 MHz, CD₂Cl₂): δ 151.9 (CH=N), 150.6 (C₆ + C_{6'}), 142.1 (N-Ph-C_{ipso}), 136.1 (C_{2a}), 131.6 (C_{5a}), 130.1 (C₄ + C_{4'}), 129.9 (N-Ph-C_{meta}), 128.8 (C₃ + C_{3'}), 127.8 (N-Ph-C_{para}), 127.6 (C₅ + C_{5'}), 121.4 (N-Ph-C_{ortho}), 120.1 (C₂ + C_{2'}), 117.7 (C_{4a}), 115.5 (C_{3a}), C₁ + C_{1'} resonance absent. ¹¹B NMR (96.27 MHz, CD₂Cl₂): δ 4.0 (Δν_{1/2} = 115 Hz). Anal. calcd (%) for C₂₃H₁₇BN₂: C, 83.16; H, 5.16; N, 8.43. Found: C, 83.72; H, 5.45; N, 8.33.



{(C₆F₅)₂B[κ^2N,N' -pyrrolyl-2-formimino-N-1,4-C₆H₄- κ^2N,N' -2-formiminopyrrolyl] B(C₆F₅)₂} (7). A mixture of two equivalents of B(C₆F₅)₂OEt (0.780 g, 2 mmol) and the 2-(*N*-bis(2-iminopyrrolyl) ligand precursor **2** (0.262 g, 1 mmol) in *ca.* 20 mL of

toluene were heated to reflux overnight. The reaction mixture was brought to room temperature and all the volatiles were evaporated, followed by extracting the residue with Et₂O (5–10 mL) and double layered with *n*-hexane. The resulting mixture was kept at –20 °C to afford complex **5** as orange crystals. Yield: 0.627 g (66%). ¹H NMR (300 MHz, CD₂Cl₂): δ 8.56 (s, 2H, CH=N), 7.39 (s, 2H, *Pyrr*), 7.29 (s, 4H, *Ph*), 7.15 (s, ³J_{HH} = 3.9 Hz, 2H, *Pyrr*), 6.55 (dd, ³J_{HH} = 3.9 Hz, ⁴J_{HH} = 1.8 Hz, 2H, *Pyrr*). ¹³C{¹H} NMR (75.47 MHz, CD₂Cl₂): δ 150.7, 150.2 (br), 147.0 (br), 142.8 (br), 139.7, 139.4 (br), 136.4 (br), 136.1 (br), 135.8, 134.9, 122.0, 119.7. ¹¹B NMR (96.27 MHz, CD₂Cl₂): δ –1.4 (Δν_{1/2} = 173 Hz). ¹⁹F{¹H} NMR (282.40 MHz, CD₂Cl₂): δ –134.20 (dd, ¹J_{CF} = 23.5 Hz, ²J_{CF} = 8.5 Hz, 4F, *o*-C₆F₅), –156.46 (t, 2F, ¹J_{CF} = 20.2 Hz, *p*-C₆F₅), –163.46 (td, ¹J_{CF} = 23.3 Hz, ²J_{CF} = 8.8 Hz, 4F, *m*-C₆F₅). Anal. calcd (%) for C₄₀H₁₂B₂F₂₀N₂·2C₄H₁₀O: C, 52.49; H, 2.94; N, 5.10. Found: C, 52.13; H, 2.45; N, 5.57.

X-ray data collection

Crystals of compounds **3**, **4**, **6** and **7** were selected under an inert atmosphere, covered with polyfluoroether oil, and mounted on a nylon loop. Crystallographic data (Table S2, ESI†) was collected using graphite monochromated Mo-Kα radiation (λ = 0.71073 Å) on a Bruker AXS-KAPPA APEX II diffractometer equipped with an Oxford Cryosystem open-flow nitrogen cryostat, at 150 K. Cell parameters were retrieved using Bruker SMART software and refined using Bruker SAINT on all observed reflections. Absorption corrections were applied using SADABS.²⁹ Structure solution and refinement were performed using direct methods with the programs SIR2004,³⁰ SIR2011,³¹ SIR2014,³² and SHELXL,³³ included in the package of programs WINGX-Version 2020.1.³⁴ The crystal size, poor quality and diffracting power of **6** gave rise to low quality data. Nevertheless, the structure was refined to convergence and all results were consistent with the model reported herein. Multiple attempts were made to grow better diffracting crystals, all of them unsuccessful. All non-hydrogen atoms were refined anisotropically. All hydrogen atoms were inserted in idealised positions and allowed to refine riding on the parent carbon atom, with C–H distances of 0.95, 0.98 and 0.99 Å for aromatic, methyl and methylene H atoms, respectively, and with U_{iso}(H) = 1.2U_{eq}(C). Graphic presentations were prepared with ORTEP-3 (version 2020.1)³⁴ and Mercury³⁵ Data was deposited in CCDC under the deposit numbers 2073567 for **3**, 2073568 for **4**, 2073569 for **6** and 2073570 for **7**.†

Thermogravimetric analysis

Thermogravimetric analyses (TGA) were carried out with a TA instrument Model TGA Q50 to determine the thermal decomposition temperatures of the boron complexes. In all cases, nitrogen was used in the TGA measurements at a flow rate of 60 mL min^{–1}. Samples were placed directly in a platinum sample holder and heated at a rate of 1 °C min^{–1} until thermal degradation was achieved. Two distinct temperatures were determined: T_{dec 1%} – temperature at which 1% degra-

ation occurred and T_{dec 5%} – temperature at which 5% degradation occurred.

Computational studies

All the Density Functional Theory²² calculations were performed using the Amsterdam Density Functional program package (ADF).²³ The geometries of **3–9**, modelled after those of **3**, **4**, **6**, **7**, **8** and **9**, were optimised without symmetry constraints, with the Vosko–Wilk–Nusair³⁶ Local Density Approximation of the correlation energy and the PBE0 functional,^{37,38} including spin orbit coupling (SOPERT),³⁹ and taking into account solvent effects (THF) treated with the COSMO model implemented in ADF. Relativistic effects were described with the ZORA approximation.⁴⁰ Triple ζ Slater-type orbitals (STO) were used to describe all the electrons of H, C, B, N, and F, augmented with a set of two polarization functions (H, single ζ 2s, 2p; C, B, N, F single ζ, 3d, 4f). TDDFT was used to obtain the geometry of the first singlet excited states,²⁴ and the absorption spectra with the Tamm-Dancoff approximation (TDA).⁴¹ Unrestricted calculations were carried out for open shell complexes. The calculated fluorescence rate constants were the reciprocal of the excited singlet state lifetimes obtained from the SOPERT calculations (SO).

A linear transit calculation was performed to analyse the conversions of complex **4** into **4**_{3E-endo}, elongating the B–N_{imine} bond, and of **4**_{3E-endo} into **4**_{3E-exo} by rotating the –C(H)=N–Ph imine group across the internal C_{pyrrolyl}–C_{imine} bond of the iminopyrrolyl. The structures corresponding to the maximum of the curve were then optimised as transition states and identified by their negative frequencies. Three-dimensional structures and representations of the orbitals were obtained with Chemcraft.⁴²

For the sake of comparison with previous studies and to evaluate the role of dispersion in these systems, the previous calculations (method A in ESI†) were repeated with the B3LYP functional (method B),⁴³ with PBE0 and the Grimme D3 correction⁴⁴ (A/D3), with B3LYP and the Grimme D3 correction (B/D3), and finally with Becke's exchange⁴⁵ and Perdew's⁴⁶ correlation functionals (gas phase, GP). The basis set was TZ2P with a small frozen core for all atoms as in method A. The latter structure was used to calculate the absorption spectra with (THF) and without solvent (GP). The first singlet excited state was obtained by promotion of one electron from the HOMO to the LUMO followed by geometry optimization. The solvent (COSMO) was introduced in a single point calculation on the structures from the GP calculation. These results are collected in the ESI.†

The Energy Decomposition Analysis (EDA)^{18,19} is a method to decompose the energy in several terms. The interaction energy between two fragments in a molecule, ΔE_{int}, is the difference between the energy of the molecule and the sum of the energies of the fragments in the geometry they have in the molecule. The fragments relax to their optimised geometry, a process involving another energy term, ΔE_{reorg}. The latter energy accounts for the geometry relaxation taking place when the 2-iminopyrrolyl and the BX₂ fragments are no longer bound, which correspond to ΔE_{reorg-ImPyrr}

and $\Delta E_{\text{reorg-BX}_2}$ terms, respectively. ΔE_{int} is a sum of several terms:

$$\Delta E_{\text{int}} = \Delta E_{\text{Pauli}} + \Delta E_{\text{elec}} + \Delta E_{\text{orb}} (+\Delta E_{\text{solv}})$$

In this equation, ΔE_{elec} is associated with the electrostatic interaction between rigid fragments, ΔE_{Pauli} with the repulsive interactions between occupied orbitals, and the ΔE_{orb} term contribution represents charge donation from one fragment to the other. As solvent (THF) was considered in the calculations, there is the solvent term, ΔE_{solv} . The sum of $\Delta E_{\text{Pauli}} + \Delta E_{\text{elec}}$ is often called ΔE_{steric} .

The binding energy (BE) between two fragments in a molecule, defined as the difference between the energy of the molecule and the sum of the energies of the fragments in their optimised geometry, can be related to the previous terms. Indeed, the BE can be obtained from the sum $\Delta E_{\text{int}} + \Delta E_{\text{reorg}}$. Therefore, the BE of several compounds, associated with the bond strengths, can be interpreted according to its dependence on several energy terms.

Spectroscopic measurements

The photophysical properties of the new complexes 3–7 were studied in diluted THF solution ($c < 3 \times 10^{-5}$ M) and in solid films. Films were prepared by drop-casting a toluene solution of the complexes mixed with ZEONEX (1% (w/w)) on quartz plates.

Absorption spectra were measured in a Beckman DU-70 spectrophotometer for compounds 3, 5 and 7, and with an Agilent Cary 8454 UV-Visible spectrophotometer for 6, and fluorescence spectra with a SPEX Fluorolog 212I for all compounds. The fluorescence spectra were collected with right angle geometry, in the S/R mode, and corrected for the photo-multiplier wavelength dependence. Fluorescence quantum yields of the mononuclear (3, 5 and 6) and the binuclear (7 and 9) complexes were determined by comparison with the quantum yields of α -tetrathiophene and α -pentathiophene ($\Phi_{\text{f}} = 0.18$ and 0.36 in dioxane at 25 °C, respectively).⁴⁷

Fluorescence decays were measured using the time-correlated single-photon counting (TCSPC) technique as previously described.⁴⁸ The pulsed (82 MHz) excitation source was a Ti:Sapphire Tsunami laser pumped with a solid-state laser Millennia Xs (Spectra Physics). Decays longer than 2 ns, were remeasured at reduced repetition rate (4 MHz) using a pulse picker (Spectra Physics, Model 3980). The Tsunami output (720–900 nm) was frequency doubled and vertically polarised. The sample emission was passed through a polariser set at the magic angle and a Jobin-Yvon H10 monochromator, and finally detected with a microchannel plate photomultiplier (Hamamatsu, R3809u-50 MCP-PT). A fraction of the Tsunami output was detected with a PHD-400-N photodiode (Becker and Hickl, GmbH) for generation of the start signal. Start and stop signals were processed with a SPC-630 acquisition board (Becker and Hickl, GmbH). The instrumental response function (IRF) was measured using a LUDOX scattering solution in water with transmittance at the excitation wavelength matched to that of the sample (FWHM = 19 ps). The IRF and sample signals were collected until 5×10^3 counts at the maximum

were reached. Fluorescence decays were deconvoluted from the IRF using the modulation functions method (Sand program).

An integrating sphere for absolute measurements was used to obtain the values for the fluorescence emission quantum yields (ϕ_{PL}) of the ZEONEX films of boron complexes 3–9, as recommended by the European Photochemistry Association (EPA).^{49,50} A NIST calibration lamp was used to compute the correction curve of the integrating sphere/detection system. This is of utmost importance, for the correct calculation of fluorescence quantum yields, ϕ_{PL} . A fixed monochromator (Oriel, FICS 77441) coupled to an ICCD detector (Andor, i-Star 720) with time gate capabilities was used in the accumulation mode. The signals were collected from the integrating sphere by a collimating beam probe coupled to an optical fibre (fused silica) in this way assuring the connection to the monochromator entrance.

The absolute fluorescence quantum yields of the ZEONEX films were obtained using the following equation:

$$\phi_{\text{PL}} = [P_{\text{c}} - (1 - A) \times P_{\text{b}}] / A \times L_{\text{a}} \text{ with } A = (1 - L_{\text{c}} / L_{\text{b}})$$

where A is the absorption coefficient, P_{b} is the light emitted by the sample after absorption of scattered excitation light, P_{c} is the light emitted by the sample after absorption of total laser light, L_{a} is the total amount of excitation laser light, L_{b} is the scattered laser light, and L_{c} is excitation light spectrum.

In many cases P_{b} is negligible and the equation simply becomes:

$$\phi_{\text{PL}} = P_{\text{c}} / (L_{\text{a}} - L_{\text{c}})$$

Using this methodology, the ϕ_{PL} determinations of several standard fluorophores with a known quantum yield were performed for validation purposes. The agreement found between the ϕ_{PL} obtained by the absolute method and the reported literature values validate the photoluminescence quantum yields determined by this absolute approach.

Electrochemical properties

The electrochemical properties of complexes 3–9 were investigated by cyclic voltammetry using a three electrodes set-up consisting of platinum disk electrode, as the working electrode, a saturated calomel reference electrode (SCE), as the reference electrode, and a platinum wire, as the counter electrode. For the current–potential measurements, a Solartron potentiostat was used and the complexes were dissolved in the electrolyte, which consisted of 0.1 M solutions of tetrabutylammonium tetrafluoroborate (TBABF₄) or tetrabutylammonium perchlorate (TBAClO₄) salts ($\geq 99.0\%$ for electrochemical analysis) in dry dichloromethane. All the measurements were performed at 50 mV s⁻¹, at room temperature, under N₂ atmosphere, and the supporting electrolytes were prepared in a N₂-filled glove box. Ferrocene was used as external reference to calibrate the reference electrode. As the energy level of Fc/Fc⁺ (ferrocene/ferrocenium ion redox couple) is at 4.80 eV below the vacuum level,⁵¹ the ionisation potential (IP) and the electron affinity (EA) of the complexes were estimated from the onset potentials determined for the oxidation and reduction scans, respectively, using the equations: IP

(-HOMO) (eV) = $E_{\text{onset,ox}}$ (eV) + 4.80 - $E_{\text{Fc}/\text{Fc}^+}$ (eV) and EA (eV) = $E_{\text{onset,ox}}$ (eV) + 4.80 eV - $E_{\text{Fc}/\text{Fc}^+}$ (eV).

Light-emitting diodes studies

Light-emitting diodes were prepared on glass/ITO substrates (ITO = indium tin oxide), which were cleaned with detergent, distilled water, acetone and isopropanol. They were treated with oxygen plasma, prior to the deposition of PEDOT:PSS (poly(3,4-ethylenedioxythiophene) doped with polystyrene sulfonic acid, CLEVIOS P VPAI 4083 from Heraeus Clevios GmbH) by spin coating. The PEDOT:PSS films (70–80 nm thick, as measured with a DEKTAK profilometer) were annealed in air for 2 minutes at 120 °C, and then transferred into a nitrogen filled glove box.

Films of complexes 3–7 were deposited on top of PEDOT:PSS by spin coating, from their THF solutions, inside the glove box. Their thicknesses were in the range 60–100 nm. The substrates were then placed inside an evaporation chamber, and the top metal cathode (calcium), *ca.* 20 nm thick, was deposited at a base pressure of 2×10^{-6} mbar through a shadow mask, defining pixel areas of 8 mm² (except for the OLEDs based on neat 6 whose pixels had areas of 4 mm²). A protective aluminium layer, *ca.* 60–80 nm thick, was deposited on top.

Mixtures of poly(vinylcarbazole) (PVK, Aldrich) and 4%, by weight, of the complexes 5, 6, 7 and 9, were prepared in THF inside the glove box and deposited by spin coating, on top of PEDOT:PSS coated ITO, giving film thicknesses in the range 85–100 nm.

Devices with an interlayer⁵² of polyTPD (poly(*N,N'*-bis-4-butylphenyl-*N,N'*-bisphenyl)benzidine, Ossila), *ca.* 5 nm thick, as determined by UV-Vis absorption between PEDOT:PSS and the PVK + complexes active layer were also prepared. This involved the deposition of a layer of polyTPD (*ca.* 30 nm thick), by spin coating from a THF solution, on the ITO/PEDOT:PSS substrates inside the glove box and annealed at 100 °C for 10 min. It was then washed with THF until a constant thickness was reached (assessed by UV-Vis absorption). The active layer (PVK + complexes) was then spun coated on top, followed by the calcium and aluminium thermal deposition.

Devices were tested under vacuum, using a K2400 Source Meter and a calibrated silicon photodiode, as described previously.⁵³ The electroluminescence (EL) spectra were obtained with a CCD spectrograph (from Ocean Optics or from ScanSci). External quantum efficiency values were estimated as detailed in ref. 53.

Conflicts of interest

There are no conflicts of interest to declare.

Acknowledgements

We thank the Fundação para a Ciência e a Tecnologia for financial support (Project PTDC/QUI-QIN/31585/2017) and for

fellowships to P.K., A.I.R., C.S.B.G., B.F. and D.V.V. (SFRH/BPD/89167/2012, PD/BD/113535/2015 – ChemMat PhD Program, SFRH/BPD/107834/2015, SFRH/BD/80122/2011, and SFRH/BD/81017/2011, respectively). Centro de Química Estrutural, BioISI – Biosystems & Integrative Sciences Institute, Instituto de Telecomunicações, LAQV – REQUIMTE, IBB-Institute for Bioengineering and Biosciences, UCIBIO – REQUIMTE, and acknowledge the financial support of Fundação para a Ciência e a Tecnologia for financial support (Projects UIDB/00100/2020 and UIDP/00100/2020, UIDB/04046/2020 and UIDP/04046/2020, UIDB/50008/2020, UIDB/50006/2020 and UIDP/50006/2020, UIDB/04565/2020, and UIDB/04378/2020 and UIDP/04378/2020, respectively).

References

- (a) A. Kraft, A. C. Grimsdale and A. B. Holmes, Electroluminescent Conjugated Polymers—Seeing Polymers in a New Light, *Angew. Chem., Int. Ed.*, 1998, **37**, 402–428; (b) C. D. Muller, A. Falcou, N. Reckefuss, M. Rojahn, V. Wiederhirn, P. Rudati, H. Frohne, O. Nuyken, H. Becker and K. Meerholz, Multi-colour organic light-emitting displays by solution processing, *Nature*, 2003, **421**, 829–833; (c) J. R. Sheats, H. Antoniadis, M. Hueschen, W. Leonard, J. Miller, R. Moon, D. Roitman and A. Stocking, Organic Electroluminescent Devices, *Science*, 1996, **273**, 884–888; (d) M. Gross, D. C. Muller, H. G. Nothofer, U. Scherf, D. Neher, C. Brauchle and K. Meerholz, Improving the performance of doped π -conjugated polymers for use in organic light-emitting diodes, *Nature*, 2000, **405**, 661–665; (e) N. S. Sariciftci, L. Smilowitz, A. J. Heeger and F. Wudl, Photoinduced Electron Transfer from a Conducting Polymer to Buckminsterfullerene, *Science*, 1992, **258**, 1474–1476; (f) J. J. M. Halls, C. A. Walsh, N. C. Greenham, E. A. Marseglia, R. H. Friend, S. C. Moratti and A. B. Holmes, Efficient photodiodes from interpenetrating polymer networks, *Nature*, 1995, **376**, 498–500; (g) U. Mitschke and P. BaEuerle, The electroluminescence of organic materials, *J. Mater. Chem.*, 2000, **10**, 1471–1507; (h) A. P. Kulkarni, C. J. Tonzola, A. Babel and S. A. Jenekhe, Electron Transport Materials for Organic Light-Emitting Diodes, *Chem. Mater.*, 2004, **16**, 4556–4573; (i) C. J. Brabec, N. S. Sariciftci and J. C. Hummelen, Plastic Solar Cells, *Adv. Funct. Mater.*, 2001, **11**, 15–26; (j) C. W. Tang and S. A. VanSlyke, Organic electroluminescent diodes, *Appl. Phys. Lett.*, 1987, **51**, 913–915; (k) F. Hide, M. A. Diaz-Garcia, B. J. Schwartz and A. I. Heeger, New Developments in the Photonic Applications of Conjugated Polymers, *Acc. Chem. Res.*, 1997, **30**, 430–436; (l) A. Hagfeldt and M. Gratzel, Molecular Photovoltaics, *Acc. Chem. Res.*, 2000, **33**, 269–277; (m) P. Peumans, A. Yakimov and S. R. Forrest, Small molecular weight organic thin-film photodetectors and solar cells, *J. Appl. Phys.*, 2003, **93**, 3693–3723; (n) C. D. Dimitrakopoulos and P. R. L. Malenfant, Organic Thin Film Transistors for Large Area Electronics, *Adv.*

- Mater.*, 2002, **14**, 99–117; (o) H. K. Shim and J. I. Jin, Light-Emitting Characteristics of Conjugated Polymers, *Adv. Polym. Sci.*, 2002, **158**, 193–243; (p) J. Slinker, D. Bernards, P. L. Houston, H. D. Abruna, S. Bernhard and G. G. Malliaras, Solid-state electroluminescent devices based on transition metal complexes, *Chem. Commun.*, 2003, 2392–2399; (q) U. Mitschke and P. Bauerle, The electroluminescence of organic materials, *J. Mater. Chem.*, 2000, **10**, 1471–1507.
- 2 (a) C. W. Tang and S. A. Van Slyke, Organic electroluminescent diodes, *Appl. Phys. Lett.*, 1987, **51**, 913–915; (b) C. W. Tang, S. A. Van Slyke and C. H. J. Chen, Electroluminescence of doped organic thin films, *Appl. Phys.*, 1989, **65**, 3610–3616.
- 3 (a) C. W. Lee, O. Y. Kim and J. Y. Lee, Organic materials for organic electronic devices, *J. Ind. Eng. Chem.*, 2014, **20**, 1198–1208; (b) N. T. Kalyani and S. J. Dhoble, Novel materials for fabrication and encapsulation of OLEDs, *Renewable Sustainable Energy Rev.*, 2015, **44**, 319–347; (c) J.-H. Jou, S. Kumar, A. Agrawal, T.-H. Li and S. Sahoo, Approaches for fabricating high efficiency organic light emitting diodes, *J. Mater. Chem. C*, 2015, **3**, 2974–3002; (d) H.-J. Li, W.-F. Fu, L. Li, X. Gan, W.-H. Mu, W.-Q. Chen, X.-M. Duan and H.-B. Song, Intense One- and Two-Photon Excited Fluorescent Bis(BF₂) Core Complex Containing a 1,8-Naphthyridine Derivative, *Org. Lett.*, 2010, **12**, 2924–2927; (e) C. Adachi, T. Tsutsui and S. Saito, Blue light-emitting organic electroluminescent devices, *Appl. Phys. Lett.*, 1990, **56**, 799; (f) J. Ye, Z. Chen, M.-K. Fung, C. Zheng, X. Ou, X. Zhang, Y. Yuan and C.-S. Lee, Carbazole/Sulfone Hybrid D- π -A-Structured Bipolar Fluorophores for High-Efficiency Blue-Violet Electroluminescence, *Chem. Mater.*, 2013, **25**, 2630–2637; (g) S. Kappaun, C. Slugovc and E. J. W. List, Phosphorescent Organic Light-Emitting Devices: Working Principle and Iridium Based Emitter Materials, *Int. J. Mol. Sci.*, 2008, **9**, 1527–1547; (h) X.-C. Hang, T. Fleetham, E. Turner, J. Brooks and J. Li, Highly Efficient Blue-Emitting Cyclometalated Platinum(II) Complexes by Judicious Molecular Design, *Angew. Chem., Int. Ed.*, 2013, **52**, 6753–6756; (i) A. Tronnier, A. Risler, N. Langer, G. Wagenblast, I. Münster and T. Strassner, A Phosphorescent C[^]C* Cyclometalated Platinum(II) Dibenzothiophene NHC Complex, *Organometallics*, 2012, **31**, 7447–7452; (j) M. A. Baldo, D. F. O'Brien, Y. You, A. Shoustikov, S. Sibley, M. E. Thompson and S. R. Forrest, Highly efficient phosphorescent emission from organic electroluminescent devices, *Nature*, 1998, **395**, 151–154; (k) Z. Zhong, X. Wang, Y. Ma, F. Peng, T. Guo, J.-X. Jiang, L. Ying, J. Wang, J. Peng and Y. Cao, Synthesis and characterization of highly efficient solution-processable orange Ir(III) complexes for phosphorescent OLED applications, *Org. Electron.*, 2018, **57**, 178–185; (l) Y.-X. Hu, X. Xia, W.-Z. He, Z.-J. Tang, Y.-L. Lv, X. Li and D.-Y. Zhang, Recent developments in benzothiazole-based iridium(III) complexes for application in OLEDs as electrophosphorescent emitters, *Org. Electron.*, 2019, **66**, 126–135; (m) G. Li, D. G. Congrave, D. Zhu, Z. Su and M. R. Bryce, Recent advances in luminescent dinuclear iridium(III) complexes and their application in organic electroluminescent devices, *Polyhedron*, 2018, **140**, 146–157; (n) C. Bizzarri, F. Hundemer, J. Busch and S. Bräse, Triplet emitters versus TADF emitters in OLEDs: A comparative study, *Polyhedron*, 2018, **140**, 51–66; (o) P. Data, P. Pander, M. Okazaki, Y. Takeda, S. Minakata and A. P. Monkman, Dibenzo[a,j]phenazine-Cored Donor-Acceptor-Donor Compounds as Green-to-Red/NIR Thermally Activated Delayed Fluorescence Organic Light Emitters, *Angew. Chem., Int. Ed.*, 2016, **55**, 5739–5744; (p) H. Wang, Y. Liu, W. Hu, W. Xu, P. Wang, Y. Wang and X. Luan, Novel spironaphthalenone-based host materials for efficient red phosphorescent and thermally activated delayed fluorescent OLEDs, *Org. Electron.*, 2018, **61**, 376–382; (q) T. Hatakeyama, K. Shiren, K. Nakajima, S. Nomura, S. Nakatsuka, K. Kinoshita, J. Ni, Y. Ono and T. Ikuta, Ultrapure Blue Thermally Activated Delayed Fluorescence Molecules: Efficient HOMO-LUMO Separation by the Multiple Resonance Effect, *Adv. Mater.*, 2016, **28**, 2777–2781; (r) Y. Wada, K. Shizu, S. Kubo, K. Suzuki, H. Tanaka and C. Adachi, Highly efficient electroluminescence from a solution-processable thermally activated delayed fluorescence emitter, *Appl. Phys. Lett.*, 2015, **107**, 183303; (s) S. Wang, X. Yan, Z. Cheng, H. Zhang, Y. Liu and Y. Wang, Highly Efficient Near-Infrared Delayed Fluorescence Organic Light Emitting Diodes Using a Phenanthrene-Based Charge-Transfer Compound, *Angew. Chem., Int. Ed.*, 2015, **54**, 13068–13072; (t) H. Uoyama, K. Goushi, K. Shizu, H. Nomura and C. Adachi, Highly efficient organic light-emitting diodes from delayed fluorescence, *Nature*, 2012, **492**, 234–238; (u) Y.-J. Shiu, Y.-C. Cheng, W.-L. Tsai, C.-C. Wu, C.-T. Chao, C.-W. Lu, Y. Chi, Y.-T. Chen, S.-H. Liu and P.-T. Chou, *Angew. Chem., Int. Ed.*, 2016, **55**, 3017–3021; (v) B. M. Bell, T. P. Clark, T. S. De Vries, Y. Lai, D. S. Laitar, T. J. Gallagher, J.-H. Jeon, K. L. Kearns, T. McIntire, S. Mukhopadhyay, H.-Y. Na, T. D. Paine and A. A. Rachford, Boron-based TADF emitters with improved OLED device efficiency roll-off and long lifetime, *Dyes Pigm.*, 2017, **141**, 83–92; (w) Y.-J. Shiu, Y.-T. Chen, W.-K. Lee, C.-C. Wu, T.-C. Lin, S.-H. Liu, P.-T. Chou, C.-W. Lu, I.-C. Cheng, Y.-J. Lien and Y. Chi, Efficient thermally activated delayed fluorescence of functional phenylpyridinato boron complexes and high performance organic light-emitting diodes, *J. Mater. Chem. C*, 2017, **5**, 1452–1462; (x) K. Matsuo and T. Yasuda, Enhancing thermally activated delayed fluorescence characteristics by intramolecular B-N coordination in a phenylpyridine-containing donor-acceptor π -system, *Chem. Commun.*, 2017, **53**, 8723–8726; (y) M. Stanoppi and A. Lorbach, Boron-based donor-spiro-acceptor compounds exhibiting thermally activated delayed fluorescence (TADF), *Dalton Trans.*, 2018, **47**, 10394–10398; (z) S. S. Kothavale and J. Y. Lee, Three- and Four-Coordinate, Boron-Based, Thermally Activated Delayed Fluorescent Emitters, *Adv. Opt. Mater.*, 2020, **8**, 2000922.

- 4 See for example: (a) L. Ji, S. Griesbeck and T. B. Marder, Recent developments in and perspectives on three-coordinate boron materials: a bright future, *Chem. Sci.*, 2017, **8**, 846–863; (b) Y. Zou, S. Gong, G. Xie and C. Yang, Design Strategy for Solution-Processable Thermally Activated Delayed Fluorescence Emitters and Their Applications in Organic Light-Emitting Diodes, *Adv. Opt. Mater.*, 2018, **6**, 1800568; (c) Y. Tao, R. Chen, H. Li, C. Zheng and W. Huang, in Thermally Activated Delayed Fluorescence Materials Based on Donor-Acceptor Molecular Systems, in *Highly Efficient OLEDs*, ed. H. Yersin, Wiley-VCH, 2018, pp. 377–423; (d) C. C. Vidyasagar, B. M. M. Flores, V. M. Jiménez-Pérez and P. M. Gurubasavaraj, Recent advances in boron-based schiff base derivatives for organic light-emitting diodes, *Mater. Today Chem.*, 2019, **11**, 133–155; (e) S. K. Møllerup and S. Wang, Boron-Doped Molecules for Optoelectronics, *Trends Chem.*, 2019, **1**, 77–89; (f) K. Suzuki, S. Kubo, K. Shizu, T. Fukushima, A. Wakamiya, Y. Murata, C. Adachi and H. Kaji, Triarylboron-Based Fluorescent Organic Light-Emitting Diodes with External Quantum Efficiencies Exceeding 20%, *Angew. Chem., Int. Ed.*, 2015, **127**, 15446–15450; (g) Y. Kitamoto, T. Namikawa, T. Suzuki, Y. Miyata, H. Kita, T. Sato and S. Oi, Dimesitylarylborane-based luminescent emitters exhibiting highly-efficient thermally activated delayed fluorescence for organic light-emitting diodes, *Org. Electron.*, 2016, **34**, 208–217; (h) Y. Gao, Q.-Q. Pan, L. Zhao, Y. Geng, T. Su, T. Gao and Z.-M. Su, Realizing performance improvement of blue thermally activated delayed fluorescence molecule DABNA by introducing substituents on the para-position of boron atom, *Chem. Phys. Lett.*, 2018, **701**, 98–102.
- 5 (a) D. Li, H. Zhang and Y. Wang, Four-coordinate organoboron compounds for organic light-emitting diodes (OLEDs), *Chem. Soc. Rev.*, 2013, **42**, 8416–8433; (b) D. Frath, J. Massue, G. Ulrich and R. Ziessel, Luminescent materials: locking π -conjugated and heterocyclic ligands with boron (III), *Angew. Chem., Int. Ed.*, 2014, **53**, 2290–2310; (c) D. Suresh and P. T. Gomes, in *Advances in Organometallic Chemistry and Catalysis*, ed. A. J. L. Pombeiro, John Wiley & Sons, Inc., Hoboken, NJ, USA, 2014, ch. 36, pp. 485–492; (d) S.-F. Liu, Q. Wu, H. L. Schmider, H. Aziz, N.-X. Hu, Z. Popovic and S. Wang, Syntheses, Structures, and Electroluminescence of New Blue/Green Luminescent Chelate Compounds: Zn(2-py-in)₂(THF), BPh₂(2-py-in), Be(2-py-in)₂, and BPh₂(2-py-aza) [2-py-in = 2-(2-pyridyl)indole; 2-py-aza = 2-(2-pyridyl)-7-azaindole], *J. Am. Chem. Soc.*, 2000, **122**, 3671–3678; (e) S. Anderson, M. S. Weaver and A. J. Hudson, Materials for organic electroluminescence: aluminium vs. boron, *Synth. Met.*, 2000, **111–112**, 459–463; (f) Y. Liu, J. Guo, H. Zhang and Y. Wang, Highly Efficient White Organic Electroluminescence from a Double-Layer Device Based on a Boron Hydroxyphenylpyridine Complex, *Angew. Chem., Int. Ed.*, 2002, **41**, 182–184; (g) H.-Y. Chen, Y. Chi, C.-S. Liu, J.-K. Yu, Y.-M. Cheng, K.-S. Chen, P.-T. Chou, S.-M. Peng, G.-H. Lee, A. J. Carty, S.-J. Yeh and C.-T. Chen, Rational Color Tuning and Luminescent Properties of Functionalized Boron-Containing 2-Pyridyl Pyrrolide Complexes, *Adv. Funct. Mater.*, 2005, **15**, 567–574; (h) Q. D. Liu, M. S. Mudadu, R. Thummel, Y. Tao and S. Wang, From Blue to Red: Syntheses, Structures, Electronic and Electroluminescent Properties of Tunable Luminescent N,N Chelate Boron Complexes, *Adv. Funct. Mater.*, 2005, **15**, 143–154; (i) J. Ugoletti, S. Hellstrom, G. J. P. Britovsek, T. S. Jones, P. Hunt and A. J. P. White, Synthesis and characterisation of luminescent fluorinated organoboron compounds, *Dalton Trans.*, 2007, **14**, 1425–1432; (j) Z. Zhang, H. Bi, Y. Zhang, D. Yao, H. Gao, Y. Fan, H. Zhang, Y. Wang, Y. Wang, Z. Chen and D. Ma, Luminescent Boron-Contained Ladder-Type π -Conjugated Compounds, *Inorg. Chem.*, 2009, **48**, 7230–7236; (k) D. Li, Z. Zhang, S. Zhao, Y. Wang and H. Zhang, Diboron-containing fluorophores with extended ladder-type π -conjugated skeletons, *Dalton Trans.*, 2011, **40**, 1279–1285; (l) Y.-L. Rao and S. Wang, Four-Coordinate Organoboron Compounds with a π -Conjugated Chelate Ligand for Optoelectronic Applications, *Inorg. Chem.*, 2011, **50**, 12263–12274; (m) Y.-J. Shiu, Y.-C. Cheng, W.-L. Tsai, C.-C. Wu, C.-T. Chao, C.-W. Lu, Y. Chi, Y.-T. Chen, S.-H. Liu and P.-T. Chou, Pyridyl Pyrrolide Boron Complexes: The Facile Generation of Thermally Activated Delayed Fluorescence and Preparation of Organic Light-Emitting Diodes, *Angew. Chem., Int. Ed.*, 2016, **55**, 3017–3021.
- 6 (a) B. Lee, B. G. Park, W. Cho, H. Y. Lee, A. Olsz, C.-H. Chen, S. B. Park and D. Lee, BOIMPY: Fluorescent Boron Complexes with Tunable and Environment-Responsive Light-Emitting Properties, *Chem. – Eur. J.*, 2016, **22**, 17321–17328; (b) B. M. Bell, T. P. Clark, T. S. De Vries, Y. Lai, D. S. Laitar, T. J. Gallagher, J.-H. Jeon, K. L. Kearns, T. McIntire, S. Mukhopadhyay, H.-Y. Na, T. D. Paine and A. A. Rachford, Boron-based TADF emitters with improved OLED device efficiency roll-off and long lifetime, *Dyes Pigm.*, 2017, **141**, 83–92; (c) Y.-J. Shiu, Y.-T. Chen, W.-K. Lee, C.-C. Wu, T.-C. Lin, S.-H. Liu, P.-T. Chou, C.-W. Lu, I.-C. Cheng, Y.-J. Lien and Y. Chi, Efficient thermally activated delayed fluorescence of functional phenylpyridinato boron complexes and high performance organic light-emitting diodes, *J. Mater. Chem. C*, 2017, **5**, 1452–1462; (d) Y. Wu, W. Yuan, H. Ji, Y. Qin, J. Zhang, H. Li, Y. Li, Y. Wang, Y. Sun and W. Liu, New fluorescent imidazo [1,2-*a*]pyridine-BODIPY chromophores: Experimental and theoretical approaches, and cell imaging exploration, *Dyes Pigm.*, 2017, **142**, 330–339; (e) H. Zhang, C. Liu, J. Xiu and J. Qiu, Triphenylamine-modified difluoroboron dibenzoylmethane derivatives: Synthesis, photophysical and electrochemical properties, *Dyes Pigm.*, 2017, **136**, 798–806; (f) M. Stanoppi and A. Lorbach, Boron-based donor-spiro-acceptor compounds exhibiting thermally activated delayed fluorescence (TADF), *Dalton Trans.*, 2018, **47**, 10394–10398; (g) K. Dhanunjayarao, X. Mukundam, R. V. R. N. Chinta and K. Venkatasubbaiah, Synthesis of highly fluorescent

- imidazole based diboron complex, *J. Organomet. Chem.*, 2018, **865**, 234–238; (h) F. Yagishita, T. Kinouchi, K. Hoshi, Y. Tezuka, Y. Jibu, T. Karatsu, N. Uemura, Y. Yoshida, T. Mino, M. Sakamoto and Y. Kawamura, Highly efficient blue emission from boron complexes of 1-(o-hydroxyphenyl)imidazo[1,5-a]pyridine, *Tetrahedron*, 2018, **74**, 3728–3733; (i) D. Wang, Y.-P. Wan, H. Liu, D.-J. Wang and G.-D. Yin, Synthesis, photoluminescent and electrochemical properties of diacetoxyboron derivatives for bis- β -diketone linked thienothiophene, *Dyes Pigm.*, 2018, **149**, 728–735; (j) X. Li, P. Tang, T. Yu, W. Su, Y. Li, Y. Wang, Y. Zhao and H. Zhang, Two *N,N*-chelated difluoroboron complexes containing phenanthroimidazole moiety: Synthesis and luminescence properties, *Dyes Pigm.*, 2019, **163**, 9–16; (k) D. Song, Y. Yu, L. Yue, D. Zhong, Y. Zhang, X. Yang, Y. Sun, G. Zhou and Z. Wu, Asymmetric thermally activated delayed fluorescence (TADF) emitters with 5,9-dioxa-13*b*-boranaphtho[3,2,1-*de*]anthracene (OBA) as the acceptor and highly efficient blue-emitting OLEDs, *J. Mater. Chem. C*, 2019, **7**, 11953–11963; (l) P. Li, H. Chan, S.-L. Lai, M. Ng, M.-Y. Chan and V. W.-W. Yam, Four-Coordinate Boron Emitters with Tridentate Chelating Ligand for Efficient and Stable Thermally Activated Delayed Fluorescence Organic Light-Emitting Devices, *Angew. Chem., Int. Ed.*, 2019, **58**, 9088–9094; (m) G. Guijie Li, W. Lou, D. Wang, C. Deng and Q. Zhang, Difluoroboron-Enabled Thermally Activated Delayed Fluorescence, *ACS Appl. Mater. Interfaces*, 2019, **11**, 32209–32217.
- 7 S. Kappaun, S. Rentenberger, A. Pogantsch, E. Zojer, K. Mereiter, G. Trimmel, R. Saf, K. C. Möller, F. Stelzer and C. Slugovc, Organoboron Quinolinolates with Extended Conjugated Chromophores: Synthesis, Structure, and Electronic and Electroluminescent Properties, *Chem. Mater.*, 2006, **18**, 3539–3547.
- 8 See for example: K. Ivaniuk, A. Pidluzhna, P. Stakhira, G. V. Baryshnikov, Y. P. Kovtun, Z. Hotra, B. F. Minaev and H. Ågren, BODIPY-core derivatives for photovoltaics and OLED applications: Studies of a series of 1,7-diphenyl-substituted BODIPY dyes, *Dyes Pigm.*, 2020, **175**, 108123.
- 9 X. Liu, Y. Ren, H. Xia, X. Fan and Y. Mu, Synthesis, structures, photoluminescent and electroluminescent properties of boron complexes with anilido-imine ligands, *Inorg. Chim. Acta*, 2010, **363**, 1441–1447.
- 10 C. S. B. Gomes, P. T. Gomes, R. E. Di Paolo, A. L. Maçanita, M. T. Duarte and M. J. Calhorda, Synthesis, Structure, and Photophysical Characterization of Blue-Green Luminescent Zinc Complexes Containing 2-Iminophenanthropyrrolyl Ligands, *Inorg. Chem.*, 2009, **48**, 11176–11186.
- 11 (a) D. Suresh, C. S. B. Gomes, P. T. Gomes, R. E. Di Paolo, A. L. Maçanita, M. J. Calhorda, A. Charas, J. Morgado and M. T. Duarte, Syntheses and photophysical properties of new iminopyrrolyl boron complexes and their application in efficient single-layer non-doped OLEDs prepared by spin coating, *Dalton Trans.*, 2012, **41**, 8502–8505; Erratum: *Dalton Trans.*, 2012, **41**, 14713; and *Dalton Trans.*, 2013, **42**, 16969; (b) M. J. Calhorda, D. Suresh, P. T. Gomes, R. E. Di Paolo and A. L. Maçanita, Photophysical properties of iminopyrrolyl boron complexes: A DFT interpretation, *Dalton Trans.*, 2012, **41**, 13210–13217; (c) D. Suresh, P. S. Lopes, B. Ferreira, C. A. Figueira, C. S. B. Gomes, P. T. Gomes, R. E. Di Paolo, A. L. Maçanita, M. T. Duarte, A. Charas, J. Morgado and M. J. Calhorda, Tunable Fluorophores Based on 2-(*N*-Arylimino)pyrrolyl Chelates of Diphenylboron: Synthesis, Structure, Photophysical Characterization, and Application in OLEDs, *Chem. – Eur. J.*, 2014, **20**, 4126–4140; (d) D. Suresh, C. S. B. Gomes, P. S. Lopes, C. A. Figueira, B. Ferreira, P. T. Gomes, R. E. Di Paolo, A. L. Maçanita, A. Charas, J. Morgado, D. Vila-Viçosa and M. J. Calhorda, Luminescent Di- and Trinuclear Boron Complexes Based on Aromatic Iminopyrrolyl Spacer Ligands: Synthesis, Characterization, and Application in OLEDs, *Chem. – Eur. J.*, 2015, **21**, 9133–9149; (e) D. Suresh, B. Ferreira, P. S. Lopes, P. Krishnamoorthy, C. S. B. Gomes, A. Charas, D. Vila-Viçosa, J. Morgado, M. J. Calhorda, A. L. Maçanita and P. T. Gomes, Boron complexes of aromatic ring fused iminopyrrolyl ligands: synthesis, structure, and luminescence properties, *Dalton Trans.*, 2016, **45**, 15603–15620; (f) P. Krishnamoorthy, B. Ferreira, C. S. B. Gomes, D. Vila-Viçosa, A. Charas, J. Morgado, M. J. Calhorda, A. L. Maçanita and P. T. Gomes, Violet-blue emitting 2-(*N*-alkylimino)pyrrolyl organoboranes: Synthesis, structure and luminescent properties, *Dyes Pigm.*, 2017, **140**, 520–532; (g) A. I. Rodrigues, C. A. Figueira, C. S. B. Gomes, D. Suresh, B. Ferreira, R. E. Di Paolo, M. J. Calhorda, D. de Sá Pereira, F. B. Dias, J. Morgado, A. L. Maçanita and P. T. Gomes, Boron complexes of aromatic 5-substituted iminopyrrolyl ligands: synthesis, structure, and luminescence properties, *Dalton Trans.*, 2019, **48**, 13337–13352; (h) A. I. Rodrigues, P. Kishnamoorthy, C. S. B. Gomes, N. Carmona, R. E. Di Paolo, P. Panda, J. Pina, J. S. Seixas de Melo, F. B. Dias, M. J. Calhorda, A. L. Maçanita, J. Morgado and P. T. Gomes, Luminescent halogen-substituted 2-(*N*-arylimino)pyrrolyl boron complexes: the internal heavy-atom effect, *Dalton Trans.*, 2020, **49**, 10185–10202.
- 12 See for example: (a) L. Bonardi, G. Ulrich and R. Ziessel, Tailoring the Properties of Boron–Dipyrrromethene Dyes with Acetylenic Functions at the 2,6,8 and 4-B Substitution Positions, *Org. Lett.*, 2008, **10**, 2183–2186; (b) S. Goeb and R. Ziessel, Convenient Synthesis of Green Diisindolodithienylpyrromethene–Dialkynyl Borane Dyes, *Org. Lett.*, 2007, **9**, 737–740; (c) C. Goze, G. Ulrich and R. Ziessel, Tetrahedral Boron Chemistry for the Preparation of Highly Efficient “Cascatelle” Devices, *J. Org. Chem.*, 2007, **72**, 313–322; (d) C. Goze, G. Ulrich and R. Ziessel, Unusual Fluorescent Monomeric and Dimeric Dialkynyl Dipyrrromethene–Borane Complexes, *Org. Lett.*, 2006, **8**, 4445–4448; (e) C. Goze, G. Ulrich, L. J. Mallon, B. D. Allen, A. Harriman and R. Ziessel, Synthesis and Photophysical Properties of Borondipyrrromethene Dyes Bearing Aryl Substituents at the Boron Center, *J. Am. Chem. Soc.*, 2006, **128**, 10231–10239; (f) G. Ulrich, C. Goze, S. Goeb,

- P. Retailleau and R. Ziessel, New fluorescent aryl- or ethynyl-aryl-boron-substituted indacenes as promising dyes, *New J. Chem.*, 2006, **30**, 982–986.
- 13 A. Nagai, K. Kokado, Y. Nagata, M. Arita and Y. Chujo, Highly Intense Fluorescent Diarylboron Diketonate, *J. Org. Chem.*, 2008, **73**, 8605–8607.
- 14 (a) A. Hübner, A. M. Diehl, M. Bolte, H.-W. Lemer and M. Wagner, *Organometallics*, 2013, **32**, 6827–6833; (b) Z. Zhang, H. Zhang, C. Jiao, K. Ye, H. Zhang, J. Zhang and Y. Wang, 2-(2-Hydroxyphenyl)benzimidazole-Based Four-Coordinate Boron-Containing Materials with Highly Efficient Deep-Blue Photoluminescence and Electroluminescence, *Inorg. Chem.*, 2015, **54**, 2652–2659; (c) M. F. Smith, S. J. Cassidy, I. A. Adams, M. Vasiliu, D. L. Gerlach, D. A. Dixon and P. A. Rugar, Substituent Effects on the Properties of Borfluorenes, *Organometallics*, 2016, **35**, 3182–3191; (d) M. Urban, K. Durka, P. Górka, G. Wiosna-Satyga, K. Nawara, P. Jankowski and S. Luliński, The effect of locking π -conjugation in organoboron moieties in the structures of luminescent tetracoordinate boron complexes, *Dalton Trans.*, 2019, **48**, 8642–8663.
- 15 See for example: (a) R. M. Bellabarba, P. T. Gomes and S. I. Pascu, Synthesis of allyl- and aryl-iminopyrrolyl complexes of nickel, *Dalton Trans.*, 2003, 4431–4436; (b) S. A. Carabineiro, R. M. Bellabarba, P. T. Gomes, S. I. Pascu, L. F. Veiros, C. Freire, L. C. J. Pereira, R. T. Henriques, M. C. Oliveira and J. E. Warren, Synthesis, Structure and Magnetic Behavior of Five-Coordinate Bis(iminopyrrolyl) Complexes of Cobalt(II) containing PMe_3 and THF Ligands, *Inorg. Chem.*, 2008, **47**, 8896–8911; (c) C. S. B. Gomes, D. Suresh, P. T. Gomes, L. F. Veiros, M. T. Duarte, T. G. Nunes and M. C. Oliveira, Sodium complexes containing 2-iminopyrrolyl ligands: the influence of steric hindrance in the formation of coordination polymers, *Dalton Trans.*, 2010, **39**, 736–748; (d) T. F. C. Cruz, C. A. Figueira, J. C. Waerenborgh, L. C. J. Pereira, Y.-L. Li, R. Lescouëzec and P. T. Gomes, Synthesis, characterization and magnetism of homoleptic bis(5-aryl-2-iminopyrrolyl) complexes of iron(II) and cobalt(II), *Polyhedron*, 2018, **152**, 179–186; (e) T. F. C. Cruz, P. S. Lopes, L. C. J. Pereira, L. F. Veiros and P. T. Gomes, Hydroboration of Terminal Olefins with Pinacolborane Catalyzed by New Mono(2-Iminopyrrolyl) Cobalt(II) Complexes, *Inorg. Chem.*, 2018, **57**, 8146–8159; (f) C. A. Figueira, P. S. Lopes, C. S. B. Gomes, J. C. S. Gomes, F. Lemos and P. T. Gomes, New phenyl-nickel complexes of bulky 2-iminopyrrolyl chelates: synthesis, characterisation and application as aluminium-free catalysts for the production of hyperbranched polyethylene, *Dalton Trans.*, 2018, **47**, 15857–15872; (g) C. A. Figueira, P. S. Lopes, C. S. B. Gomes, J. C. S. Gomes, L. F. Veiros, F. Lemos and P. T. Gomes, Neutral Mono(5-aryl-2-iminopyrrolyl)nickel(II) Complexes as Precatalysts for the Synthesis of Highly Branched Ethylene Oligomers: Preparation, Molecular Characterization, and Catalytic Studies, *Organometallics*, 2019, **38**, 614–625.
- 16 (a) Herrmann/Brauer, *Synthetic Methods of Organometallic and Inorganic Chemistry*, Georg Thieme Verlag Stuttgart, New York, 2002, Vol. 10, p. 54; (b) S. Biswas, I. M. Oppel and H. F. Bettinger, Synthesis and Structural Characterization of 9-Azido-9-Borfluorene: Monomer and Cyclootrimer of a Borole Azide, *Inorg. Chem.*, 2010, **49**, 4499–4506.
- 17 R. Duchateau, S. J. Lancaster, M. Thornton-Pett and M. Bochmann, Synthesis of Cyclopentadienyl-, Indenyl-, and Fluorenylbis(pentafluorophenyl)boranes as Ligands in Titanium and Zirconium Half-Sandwich Complexes. The Crystal Structures of $\text{C}_{13}\text{H}_9\text{B}(\text{C}_6\text{F}_5)_2 \cdot t\text{-BuNH}_2$, $\text{C}_{13}\text{H}_8\text{SiMe}_3\text{B}(\text{C}_6\text{F}_5)_2$, and $\{\eta^5\text{-C}_5\text{H}_4\text{B}(\text{C}_6\text{F}_5)_2\}\text{TiCl}_3$, *Organometallics*, 1997, **16**, 4995–5005.
- 18 K. Kitaura and K. Morokuma, A new energy decomposition scheme for molecular interactions within the Hartree–Fock approximation, *Int. J. Quantum Chem.*, 1975, **10**, 325–340.
- 19 M. von Hopffgarten and G. Frenking, Energy decomposition analysis, *Wiley Interdiscip. Rev.: Comput. Mol. Sci.*, 2012, **2**, 43–62.
- 20 S. Heřmánek, Boron-11 NMR spectra of boranes, main-group heteroboranes, and substituted derivatives. Factors influencing chemical shifts of skeletal atoms, *Chem. Rev.*, 1992, **92**, 325–362.
- 21 (a) D. R. Brittelli and D. F. Eaton, Twisted internal charge transfer emission in B,B-bis(mesityl) pyrroloboranes, *J. Phys. Org. Chem.*, 1989, **2**, 89–92; (b) C. Cornelilßen and W. Rettig, Unusual fluorescence red shifts in (TICT)-forming boranes, *J. Fluoresc.*, 1994, **4**, 71–74; (c) C. Cornelilßen-Gude and W. Rettig, An Experimental and ab Initio CI Study for Charge Transfer Excited States and Their Relaxation in Pyrroloborane Derivatives, *J. Phys. Chem. A*, 1999, **103**, 4371–4377.
- 22 R. G. Parr and W. Yang, *Density Functional Theory of Atoms and Molecules*, Oxford University Press, New York, 1989.
- 23 (a) G. te Velde, F. M. Bickelhaupt, S. J. A. van Gisbergen, C. Fonseca Guerra, E. J. Baerends, J. G. Snijders and T. Ziegler, Chemistry with ADF, *J. Comput. Chem.*, 2001, **22**, 931–967; (b) C. Fonseca Guerra, J. G. Snijders, G. te Velde and E. J. Baerends, Towards an order-N DFT method, *Theor. Chem. Acc.*, 1998, **99**, 391–403; (c) ADF2013, SCM, Theoretical Chemistry, Vrije Universiteit, Amsterdam, The Netherlands, <http://www.scm.com>.
- 24 (a) S. J. A. van Gisbergen, J. A. Groeneveld, A. Rosa, J. G. Snijders and E. J. Baerends, Excitation Energies for Transition Metal Compounds from Time-Dependent Density Functional Theory. Applications to MnO_4^- , $\text{Ni}(\text{CO})_4$, and $\text{Mn}_2(\text{CO})_{10}$, *J. Phys. Chem. A*, 1999, **103**, 6835–6844; (b) A. Rosa, J. Baerends, S. J. A. van Gisbergen, E. van Lenthe, J. A. Groeneveld and J. G. Snijders, Electronic Spectra of $\text{M}(\text{CO})_6$ ($\text{M} = \text{Cr}, \text{Mo}, \text{W}$) Revisited by a Relativistic TDDFT Approach, *J. Am. Chem. Soc.*, 1999, **121**, 10356–10365; (c) S. J. A. van Gisbergen, A. Rosa, G. Ricciardi and E. J. Baerends, Time-dependent density functional calculations on the electronic absorption spectrum of free base porphyrin, *J. Chem. Phys.*, 1999, **111**, 2499–

- 2507; (d) S. J. A. van Gisbergen, J. G. Snijders and E. J. Baerends, Implementation of time-dependent density functional response equations, *Comput. Phys. Commun.*, 1999, **118**, 119–138; (e) J. Moussa, L.-M. Chamoreau, A. D. Esposti, M. P. Gullo, A. Barbieri and H. Amouri, Tuning Excited States of Bipyridyl Platinum(II) Chromophores with π -Bonded Catecholate Organometallic Ligands: Synthesis, Structures, TD-DFT Calculations, and Photophysical Properties, *Inorg. Chem.*, 2014, **53**, 6624–6633.
- 25 K. C. Gordon, P. J. Walsh and E. M. McGale, Electroluminescence from PVK-based polymer blends with metal complex dyes, *Curr. Appl. Phys.*, 2004, **4**, 331–334.
- 26 X. Gong, S.-H. Lim, J. C. Ostrowski, D. Moses, C. J. Bardeen and G. C. Bazan, Phosphorescence from iridium complexes doped into polymer blends, *J. Appl. Phys.*, 2004, **95**, 948–953.
- 27 (a) S. A. Carabineiro, L. C. Silva, P. T. Gomes, L. C. J. Pereira, L. F. Veiros, S. I. Pascu, M. T. Duarte, S. Namorado and R. T. Henriques, Synthesis and Characterization of Tetrahedral and Square Planar Bis(iminopyrrolyl) Complexes of Cobalt(II), *Inorg. Chem.*, 2007, **46**, 6880–6890; (b) C. Pozo-Gonzalo, J. A. Pomposo, J. Rodríguez, E. Y. Schmidt, A. M. Vasil'’tsov, N. V. Zorina, A. V. Ivanov, B. A. Trofimov, A. I. Mikhaleva and A. B. Zaitsev, Synthesis and electrochemical study of narrow band gap conducting polymers based on 2,2'-dipyroles linked with conjugated aza-spacers, *Synth. Met.*, 2007, **157**, 60–65.
- 28 R. Koster, P. Binger and W. Fenzl, Triphenylborane, *Inorg. Synth.*, 1974, **15**, 134–136.
- 29 G. M. Sheldrick, *SADABS - Program for Empirical Absorption Correction*, Univ. Göttingen, Germany, 1996.
- 30 M. C. Burla, R. Caliendo, M. Camalli, B. Carrozzini, G. L. Cascarano, L. De Caro, C. Giacovazzo, G. Polidori and R. Spagna, SIR2004: an improved tool for crystal structure determination and refinement, *J. Appl. Crystallogr.*, 2005, **38**, 381–388.
- 31 M. Camalli, B. Carrozzini, G. L. Cascarano and C. Giacovazzo, Automated determination of the extinction symbol via electron diffraction data, *J. Appl. Crystallogr.*, 2012, **45**, 351–356.
- 32 M. C. Burla, R. Caliendo, B. Carrozzini, G. L. Cascarano, C. Cuocci, C. Giacovazzo, M. Mallamo, A. Mazzone and G. Polidori, Crystal structure determination and refinement via SIR2014, *J. Appl. Crystallogr.*, 2015, **48**, 306–309.
- 33 (a) SHELXL: G. M. Sheldrick, Crystal structure refinement with SHELXL, *Acta Crystallogr., Sect. C: Struct. Chem.*, 2015, **71**, 3–8; (b) C. B. Hübschle, G. M. Sheldrick and B. Dittrich, ShelXle: a Qt graphical user interface for SHELXL, *J. Appl. Crystallogr.*, 2011, **44**, 1281–1284.
- 34 L. J. Farrugia, WinGX and ORTEP for Windows: an update, *J. Appl. Crystallogr.*, 2012, **45**, 849–854.
- 35 C. F. Macrae, I. Sovago, S. J. Cottrell, P. T. A. Galek, P. McCabe, E. Pidcock, M. Platings, G. P. Shields, J. S. Stevens, M. Towler and P. A. Wood, Mercury 4.0: from visualization to analysis, design and prediction, *J. Appl. Crystallogr.*, 2020, **53**, 226–235.
- 36 S. H. Vosko, L. Wilk and M. Nusair, Accurate spin-dependent electron liquid correlation energies for local spin density calculations: a critical analysis, *Can. J. Phys.*, 1980, **58**, 1200–1211.
- 37 M. Ernzerhof and G. Scuseria, Assessment of the Perdew–Burke–Ernzerhof exchange–correlation functional, *J. Chem. Phys.*, 1999, **110**, 5029–5036.
- 38 C. Adamo and V. Barone, Toward reliable density functional methods without adjustable parameters: The PBE0 model, *J. Chem. Phys.*, 1999, **110**, 6158–6170.
- 39 F. Wang and T. Ziegler, A simplified relativistic time-dependent density-functional theory formalism for the calculations of excitation energies including spin-orbit coupling effect, *J. Chem. Phys.*, 2005, **123**, 154102.
- 40 E. van Lenthe, A. Ehlers and E.-J. Baerends, Geometry optimizations in the zero order regular approximation for relativistic effects, *J. Chem. Phys.*, 1999, **110**, 8943–8953.
- 41 S. Hirata and M. Head-Gordon, Time-dependent density functional theory within the Tamm-Dancoff approximation, *Chem. Phys. Lett.*, 1999, **314**, 291–299.
- 42 Chemcraft. Available online: <http://www.chemcraftprog.com/index.html> (last accessed on September 2020).
- 43 M. Reiher, O. Salomon and B. A. Hess, Reparameterization of hybrid functionals based on energy differences of states of different multiplicity, *Theor. Chem. Acc.*, 2001, **107**, 48–55.
- 44 S. Grimme, Accurate description of van der Waals complexes by density functional theory including empirical corrections, *J. Comput. Chem.*, 2004, **25**, 1463–1473.
- 45 A. D. Becke, A new inhomogeneity parameter in density-functional theory, *J. Chem. Phys.*, 1998, **109**, 2092–2098.
- 46 (a) J. P. Perdew, Density-functional approximation for the correlation energy of the inhomogeneous electron gas, *Phys. Rev. B: Condens. Matter Mater. Phys.*, 1986, **33**, 8822–8824; (b) J. P. Perdew, *Phys. Rev. B: Condens. Matter Mater. Phys.*, 1986, **34**, 7406–7406, Erratum.
- 47 R. S. Becker, J. Seixas de Melo, A. L. Maçanita and F. Elisei, Comprehensive Evaluation of the Absorption, Photophysical, Energy Transfer, Structural, and Theoretical Properties of α -Oligothiophenes with One to Seven Rings, *J. Phys. Chem.*, 1996, **100**, 18683–18695.
- 48 B. Ferreira, P. F. Silva, J. S. Seixas de Melo, J. Pina and A. L. Maçanita, Excited-State Dynamics and Self-Organization of Poly(3-hexylthiophene) (P3(HT)) in Solution and Thin Films, *J. Phys. Chem. B*, 2012, **116**, 2347–2355.
- 49 D. P. Ferreira, D. S. Conceição, F. Fernandes, T. Sousa, R. C. Calhelha, I. C. F. R. Ferreira, P. F. Santos and L. F. Vieira Ferreira, Characterization of a Squaraine/Chitosan System for Photodynamic Therapy of Cancer, *J. Phys. Chem. B*, 2016, **120**, 1212–1220.

- 50 A. Barbieri and G. Accorsi, *EPA Newslett.*, 2006, 26–34.
- 51 J. Pommerehne, H. Vestweber, W. Guss, R. F. Mahrt, H. Bässler, M. Porsh and J. Daub, Efficient two layer leds on a polymer blend basis, *Adv. Mater.*, 1995, 7, 551–554.
- 52 G. Bernardo, A. Charas, L. Alcácer and J. Morgado, Improving polymer light-emitting diodes efficiency using interlayers based on cross-linkable polymers, *Appl. Phys. Lett.*, 2007, **91**, 063509.
- 53 J. Morgado, A. Charas, J. A. Fernandes, I. S. Gonçalves, L. D. Carlos and L. Alcácer, Luminescence properties of composites made of a europium(III) complex and electroluminescent polymers with different energy gaps, *J. Phys. D: Appl. Phys.*, 2006, **39**, 3582–3587.

New luminescent tetracoordinate boron complexes: an in-depth experimental and theoretical characterisation and their application in OLEDs

Paramasivam Krishnamoorthy,^{a,h} Carina B. Fialho,^a Tiago F. C. Cruz,^a Ana I. Rodrigues,^a Bruno Ferreira,^a Clara S. B. Gomes,^{a,e,i} Diogo Vila-Viçosa,^c Ana Charas,^d José M. S. S. Esperança,^e Luís F. Vieira Ferreira,^f Maria José Calhorda,^c António L. Maçanita,^{a,b}
Jorge Morgado^{d,g} and Pedro T. Gomes^{*,a,b}

^a Centro de Química Estrutural, Instituto Superior Técnico, Universidade de Lisboa, Av. Rovisco Pais, 1049-001 Lisboa, Portugal.

^b Departamento de Engenharia Química, Instituto Superior Técnico, Universidade de Lisboa, Av. Rovisco Pais, 1049-001 Lisboa, Portugal.

^c BioISI - Biosystems & Integrative Sciences Institute, Departamento de Química e Bioquímica, Faculdade de Ciências, Universidade de Lisboa, Campo Grande, Ed. C8, 1749-016 Lisboa, Portugal.

^d Instituto de Telecomunicações, Av. Rovisco Pais, 1049-001 Lisboa, Portugal.

^e LAQV-REQUIMTE, Departamento de Química, Faculdade de Ciências e Tecnologia, Universidade NOVA de Lisboa, 2829-516 Caparica, Portugal

^f BSIRG – Biospectroscopy and Interfaces Research Group, IBB-Institute for Bioengineering and Biosciences, Instituto Superior Técnico, Universidade de Lisboa, 1049-001 Lisboa, Portugal

^g Department of Bioengineering, Instituto Superior Técnico, Universidade de Lisboa, Av. Rovisco Pais, 1049-001 Lisboa, Portugal.

^h Centre for Environmental Research, Department of Chemistry, Kongu Engineering College, Perundurai, Erode 638 060, India

ⁱ UCIBIO-REQUIMTE, Departamento de Química, Faculdade de Ciências e Tecnologia, Universidade NOVA de Lisboa, 2829-516 Caparica, Portugal.

* Corresponding author: Pedro T. Gomes; E-mail: pedro.t.gomes@tecnico.ulisboa.pt

Index

Crystallographic and molecular structure data of boron complexes 3 , 4 , 6 and 7	S3
Thermogravimetric Analysis (TGA)	S8
Computational studies – Energy Decomposition Analysis and binding energy	S10
NMR spectra of complexes 3-7	S13
Variable-temperature (VT) NMR spectra of complex 4	S23
Van't Hoff plot for the equilibrium between tetracoordinate and tricoordinate isomers of complex 4	S27
Computational studies – Energy profile for the conversion of complex 4 into the tricoordinate isomers 4_{3E-endo} and 4_{3E-exo} and comparison with mononuclear boron complexes 3 , 5 , 6 and 8	S28
Computational studies – Ground state and first excited state optimised structure geometries of boron complexes 3-9	S32
Computational studies – Frontier orbitals and composition of the lower energy electronic transitions in boron complexes 4 and 6	S35
Computational studies – Calculated HOMOs and LUMOs energies for complexes 3-9 using different methods.....	S36
Computational studies – Calculated absorption energies and first excited state lifetimes for complexes 3-9 using different methods.....	S37
Computational studies – Composition of the lower energy electronic transitions in complexes 4 and 6	S38
Computational studies – Calculated energies of $S_1 \rightarrow S_0$ transition for complexes 3-2 using different methods.....	S39
Electrochemical properties	S40
Electroluminescence performance	S42

Crystallographic and molecular structure data of boron complexes 3, 4, 6 and 7

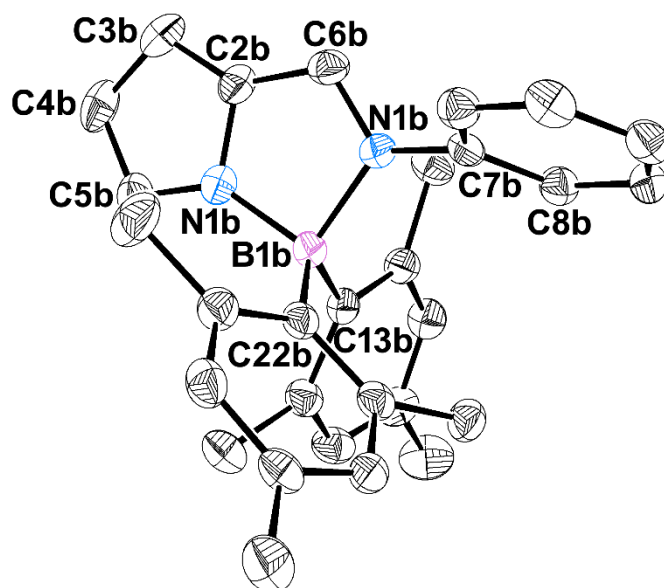


Figure S1. Perspective view of the molecular structure of 2-iminopyrrolyl boron complex 4 (molecule B), using 50% probability level ellipsoids. All calculated hydrogen atoms were omitted for clarity.

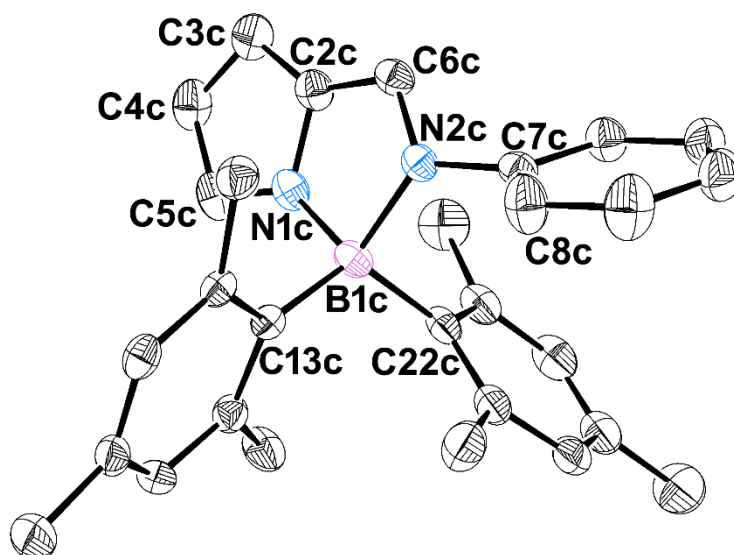


Figure S2. Perspective view of the molecular structure of 2-iminopyrrolyl boron complex 4 (molecule C), using 50% probability level ellipsoids. All calculated hydrogen atoms were omitted for clarity.

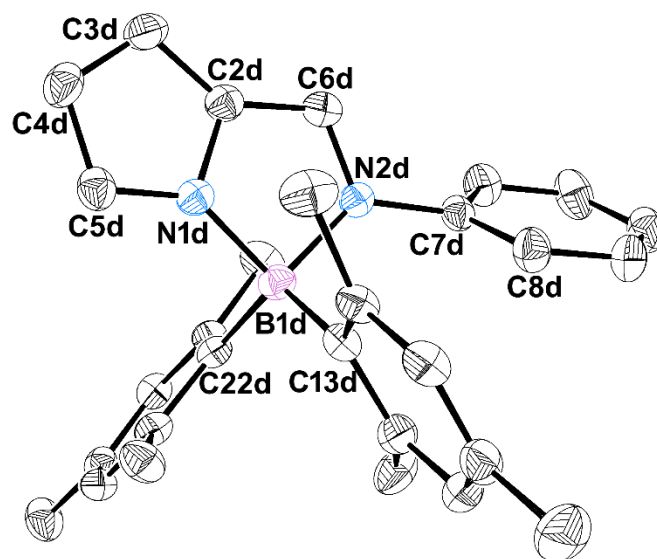


Figure S3. Perspective views of the molecular structure of 2-iminopyrrolyl boron complex **4** (molecule D), using 50% probability level ellipsoids. All calculated hydrogens atoms were omitted for clarity.

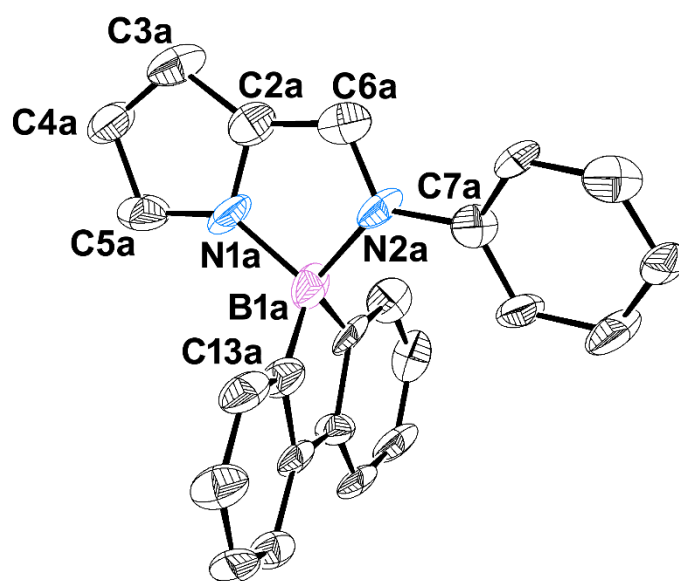


Figure S4. Perspective view of the molecular structure of 2-iminopyrrolyl boron complex **6** (molecule A), using 50% probability level ellipsoids. All calculated hydrogen atoms were omitted for clarity.

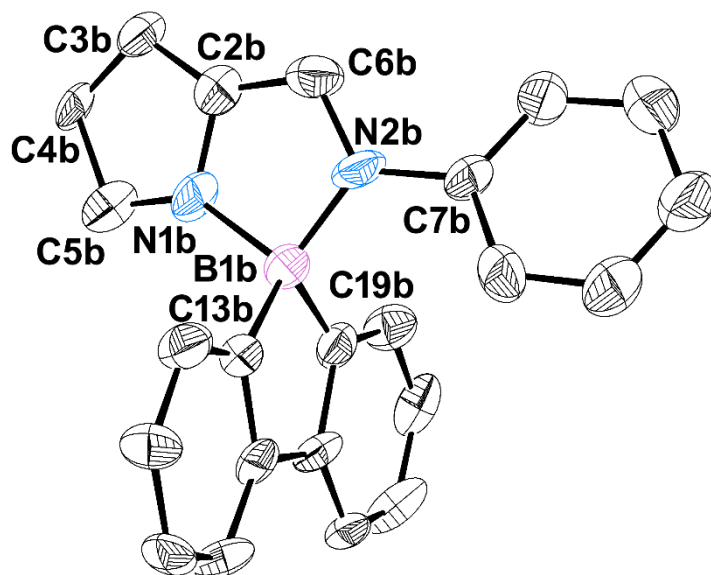


Figure S5. Perspective view of the molecular structure of 2-iminopyrrolyl boron complex **6** (molecule B), using 50% probability level ellipsoids. All calculated hydrogen atoms were omitted for clarity.

Table S1. Selected bond distances (Å) and angles (°) for compounds **3**, **4**, **6** and **7**.

	3	4				6		7
		<i>molecule A</i>	<i>molecule B</i>	<i>molecule C</i>	<i>molecule D</i>	<i>molecule A</i>	<i>molecule B</i>	
<i>Bond distances</i>								
N1–B1	1.537(5)	1.589(3)	1.581(3)	1.573(3)	1.589(2)	1.570(10)	1.592(10)	1.555(2)
N2–B1	1.603(4)	1.682(2)	1.648(3)	1.654(3)	1.664(3)	1.613(11)	1.562(11)	1.602(2)
N1–C2	1.370(4)	1.381(2)	1.383(3)	1.385(2)	1.371(2)	1.357(10)	1.382(10)	1.385(2)
N1–C5	1.353(4)	1.354(2)	1.348(3)	1.350(3)	1.345(2)	1.360(10)	1.342(10)	1.343(2)
C2–C6	1.410(4)	1.396(2)	1.398(3)	1.401(3)	1.412(3)	1.432(11)	1.388(11)	1.392(2)
N2–C6	1.305(4)	1.309(2)	1.313(2)	1.309(2)	1.305(2)	1.284(9)	1.301(8)	1.3218(19)
N2–C7	1.431(4)	1.448(2)	1.437(2)	1.441(2)	1.450(2)	1.452(9)	1.427(10)	1.4186(19)
B1–E1 ^a	1.379(4)	1.626(3)	1.638(3)	1.627(3)	1.621(3)	1.598(11)	1.652(12)	1.631(2)
B1–E2 ^b	1.381(4)	1.643(3)	1.640(3)	1.640(3)	1.639(3)	1.600(12)	1.593(11)	1.630(2)
<i>Bond angles</i>								
N1–B1–N2	97.0(2)	93.41(13)	94.01(14)	94.49(14)	93.49(13)	94.3(6)	96.5(6)	96.62(11)
C5–N1–C2	107.9(3)	106.48(16)	107.17(16)	107.36(17)	107.62(15)	107.0(6)	109.8(7)	107.83(13)
C2–N1–B1	111.0(2)	112.85(14)	112.48(16)	112.40(16)	112.58(15)	113.1(7)	108.9(7)	110.90(12)
C5–N1–B1	140.9(3)	140.34(16)	139.35(18)	139.81(17)	139.39(17)	139.9(7)	141.1(7)	141.27(14)
C6–N2–C7	123.9(3)	115.46(15)	119.01(17)	119.29(16)	117.76(16)	121.0(7)	121.8(7)	124.01(12)
C6–N2–B1	110.6(2)	110.69(14)	111.41(16)	110.71(16)	111.75(14)	121.0(7)	112.5(7)	110.32(12)
C7–N2–B1	125.3(2)	132.82(14)	126.56(15)	126.84(15)	129.57(14)	126.6(6)	125.4(6)	125.20(12)
E1–B1–E2	109.9(3)	113.22(16)	116.34(16)	116.51(16)	116.15(15)	100.7(6)	99.6(6)	117.27(13)
E1–B1–N1	112.9(3)	120.39(16)	104.63(15)	104.43(16)	118.73(15)	116.2(6)	112.1(7)	107.53(13)
E2–B1–N1	114.3(3)	103.79(15)	119.21(15)	119.06(15)	102.81(14)	114.9(7)	113.8(6)	113.37(12)
E1–B1–N2	111.8(3)	104.63(15)	117.85(16)	120.15(14)	104.42(15)	115.9(7)	117.8(6)	112.88(12)
E2–B1–N2	110.3(3)	120.84(15)	103.32(15)	100.98(15)	119.82(16)	115.7(6)	117.8(8)	107.33(12)
$\omega_{(B1)}$ ^c	91.13(12)	-77.47(8)	-79.05(7)	77.27(8)	78.16(7)	90.4(3)	89.2(3)	85.81(6)
$\varphi_{(Pyr-Ph)}$ ^d	26.58(12)	-57.53(7)	66.98(7)	64.19(9)	57.37(9)	21.7(3)	26.0(3)	23.72(10)
C6–N2–C7–Cx ^e	-24.0(5)	59.2(2)	53.8(2)	-52.2(2)	-61.8(2)	19.3(10)	-22.6(11)	-14.9(2)

^a E1 = F1 (**3**), C13 (**4** and **6**) and C10 (**7**); ^b E2 = F2 (**3**), C22 (**4**), C19 (**6**) and C16 (**7**); ^c Dihedral angle between N1–B1–N2 and E1–B1–E2; ^d Dihedral angle between the average planes of the 2-iminopyrrolyl (Pyr) moiety and of the iminic *N*-phenyl ring (Ph); ^e Cx = C8 or C12.

Table S2. Crystal data and structure refinement for compounds **3**, **4**, **6** and **7**.

Compound	3	4	6	7
Formula	C ₁₁ H ₉ F ₂ BN ₂	C ₂₉ H ₃₁ BN ₂	C ₂₃ H ₁₇ BN ₂	C ₄₈ H ₃₂ B ₂ F ₂₀ N ₄ O ₂
<i>M</i>	218.01	418.37	332.19	1098.39
λ (Å)	0.71073	0.71073	0.71073	0.71073
<i>T</i> (K)	150(2)	150(2)	150(2)	150(2)
crystal system	Monoclinic	Triclinic	Monoclinic	Triclinic
space group	<i>P</i> 2 ₁ / <i>n</i>	<i>P</i> -1	<i>P</i> 2 ₁ / <i>c</i>	<i>P</i> -1
<i>a</i> (Å)	6.413(3)	16.9181(13)	17.677(4)	8.9402(4)
<i>b</i> (Å)	7.019(3)	17.0427(13)	11.145(3)	10.6602(5)
<i>c</i> (Å)	22.215(8)	17.8177(12)	17.729(4)	12.8486(6)
α (deg)	90	75.611(3)	90	105.370(2)
β (deg)	95.590(14)	71.293(3)	97.743(12)	97.060(2)
γ (deg)	90	87.992(4)	90	95.9220(10)
<i>V</i> (Å ³)	995.2(6)	4707.7(6)	3461.1(13)	1159.93(9)
<i>Z</i>	4	8	8	1
<i>Z</i> '	1	4	2	0.5
ρ_{calc} (g cm ⁻³)	1.455	1.181	1.275	1.572
μ (mm ⁻¹)	0.113	0.068	0.074	0.152
θ_{max} (deg)	25.66	25.77	25.34	26.19
total data	3960	41526	54163	14831
unique data	1100	11977	1773	3567
<i>R</i> _{int}	0.0509	0.0510	0.3189	0.0451
<i>R</i> [<i>I</i> > 3 σ (<i>I</i>)]	0.0594	0.055	0.1233	0.0367
<i>wR</i> ₂	0.1459	0.1216	0.2685	0.0881
Goodness of fit	0.958	1.073	0.911	1.059
ρ_{min}	-0.259	-0.519	-0.427	-0.219
ρ_{max}	0.232	0.684	0.350	0.249

Thermogravimetric Analysis (TGA)

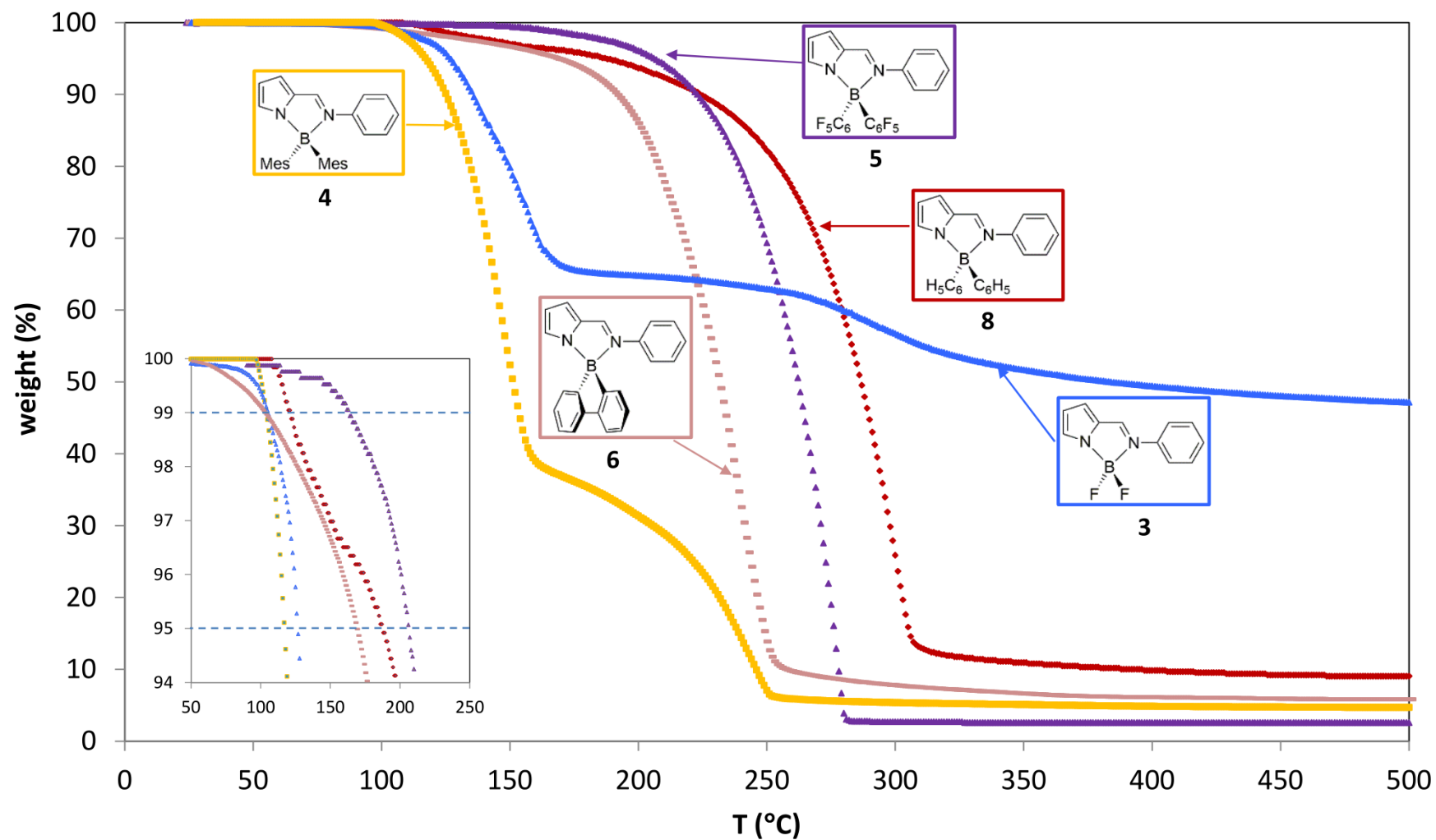


Fig. S6. TGA thermograms of complexes **3**, **4**, **5**, **6** and **8**. The inset of the picture represents the beginning of the decomposition with two dashed lines, one for the 1% weight loss, and another for the 5% weight loss.

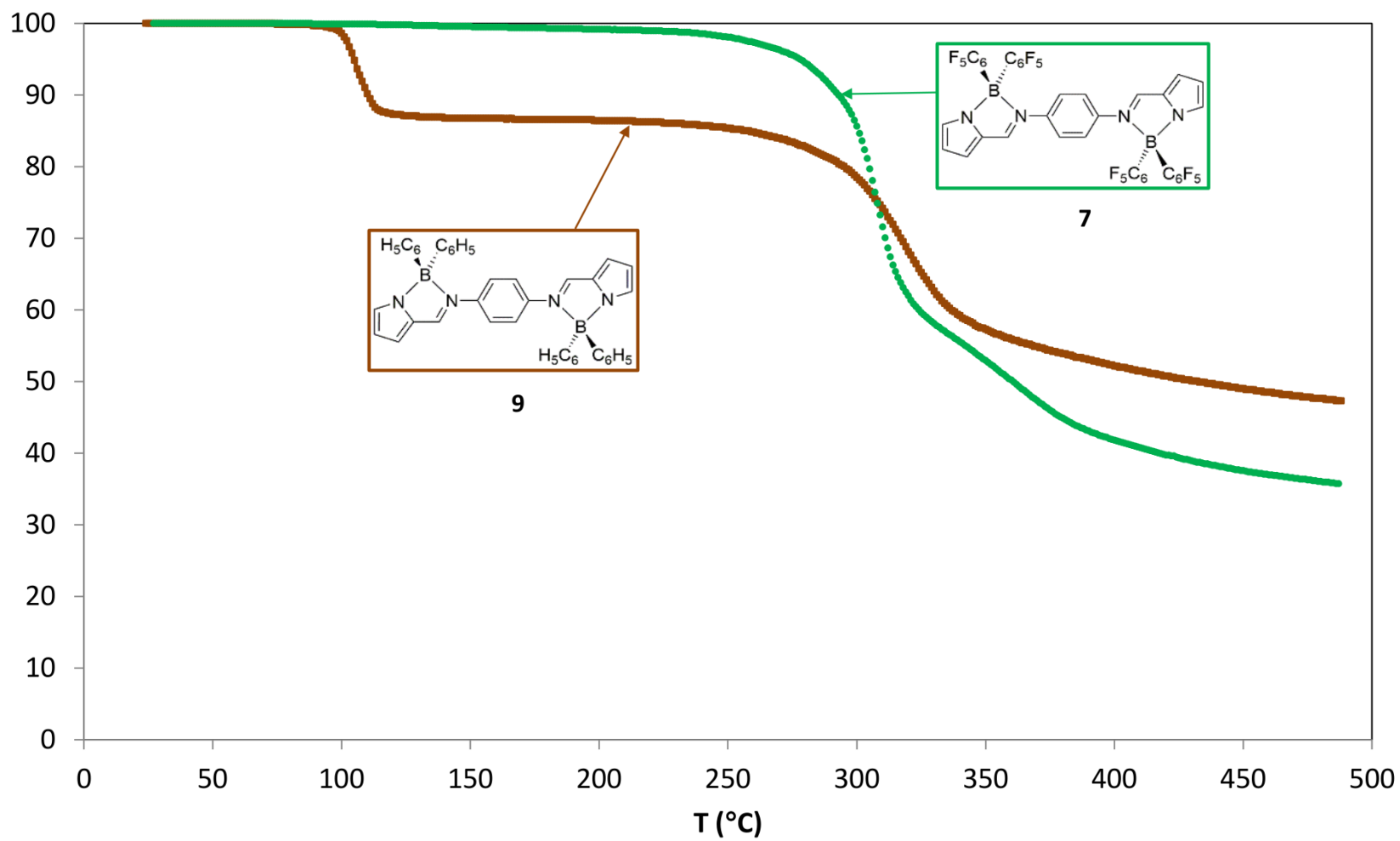


Fig. S7. TGA thermograms of complexes **7** and **9**.

Computational studies – Energy Decomposition Analysis and binding energy

The complexes **3-9** share 2-iminopyrrolyl ligands and therefore the binding energies of this ligand to the boron fragment (BX_2) could be related to their thermal stability described above (Figures S5 and S6 and Table 1). This led us to perform an Energy Decomposition Analysis (EDA) to understand the differences between them. The binding energy (BE) between two fragments in a molecule is the difference between the energy of the molecule and the sum of the energies of the fragments in their optimised geometry. On the other hand, it is possible to define the interaction energy (ΔE_{int}) as the difference between the energy of the molecule and the sum of the energies of the fragments when they keep the same geometry as they have in the molecule. The energy needed to convert this geometry into the geometry with the lowest energy is called the reorganization energy (E_{reorg}). Thus:

$$\text{BE} = \Delta E_{int} + \Delta E_{reorg}$$

The Energy Decomposition Analysis (EDA) gives a different way of interpreting the ΔE_{int} terms by decomposing them:

$$\Delta E_{int} = \Delta E_{Pauli} + \Delta E_{elec} + \Delta E_{orb}$$

where ΔE_{Pauli} is a repulsive term representing the destabilizing interactions between occupied orbitals, while the attractive terms ΔE_{elec} and ΔE_{orb} include the electrostatic interaction between the rigid fragments, and the interaction between orbitals, such as HOMO-LUMO interactions and polarization (mixing of empty and occupied levels of each fragment occurring in the presence of another fragment), respectively.

When the calculations include the effect of the solvent, as happens in this study, another term (ΔE_{solv}), arising from the interactions of molecules and fragment with the solvent, also contributes to the interaction energy:

$$\Delta E_{int} = \Delta E_{Pauli} + \Delta E_{elec} + \Delta E_{orb} + \Delta E_{solv}$$

The EDA values are given in Table S5. In the five mononuclear complexes, the binding energy (BE, kcal mol⁻¹) increases from **4** ($\text{B}(2,4,6\text{-Me}_3\text{-C}_6\text{H}_2)_2$, -77.7) < **8** ($\text{B}(\text{C}_6\text{H}_5)_2$, -112.0) < **5** ($\text{B}(\text{C}_6\text{F}_5)_2$, -131.5) < **6** (9-borafluorenyl, -143.0) < **3** (BF_2 , -153.4) and follows almost the same order of the interaction energy ΔE_{int} . This indicates that the reorganizing energies do not change the trend. Indeed, the 2-iminopyrrolyl ligand requires ~21.5 – 23.8 kcal mol⁻¹ to relax from the geometry it adopts in the complex to the optimised one. It is practically the same value for all the complexes. The relaxation of the BX_2 fragment involves a change in the F-B-F or C-B-C angle observed in the

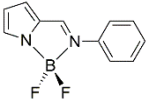
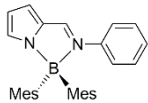
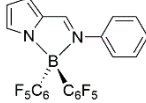
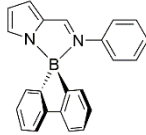
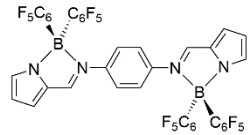
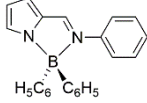
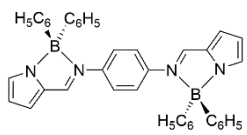
complex to 180° in the free fragment (except in the case of the chelated 9-borafluorenyl fragment in **6**). The maximum reorganization energy (kcal mol⁻¹) occurs for the F-B-F in **3** (67.2), followed by **4** (61.2), **5** (51.4), **8** (45.8) and, not surprisingly, the more rigid **6** (31.9).

The ΔE_{steric} term shows the balance between the Pauli repulsion and the attractive electrostatic term. It is negative for all complexes except **4**. Since ΔE_{orb} and ΔE_{solv} are not very different for the five species, we assign the lowest BE of **4** to the large ΔE_{Pauli} repulsive term associated with a low ΔE_{elec} . Complex **3**, with low ΔE_{Pauli} and very large ΔE_{elec} displays the highest BE. The other fluorinated complex, **5**, also has a large ΔE_{elec} but high ΔE_{Pauli} , the resulting ΔE_{steric} being similar to that of **6**. The smaller solvent penalty and reorganization energy of the BX₂ fragment confer a higher BE to **6** than to **5**. Complex **8** has a less negative ΔE_{steric} term.

The BEs (kcal mol⁻¹) of the pentafluorinated derivatives are larger than those of the hydrogenated analogues. Indeed, the BE of **5** [B(C₆F₅)₂] is -131.5 and of **8** [B(C₆H₅)₂] is -112.0, while for the binuclear **7** and **9** are -270.1 and -233.5, respectively, reflecting the main pattern observed in the experimental thermal analysis (Table S3). This behaviour is assigned mainly to the larger attractive electrostatic and covalent interactions in the fluorinated species. The ΔE_{orb} term is for both **7** and **9** more negative than in the mononuclear species (twice owing to the double number of B-N bonds formed) and is higher for the fluorinated **7**, which has a higher BE and ΔE_{int} , despite the higher solvent destabilization.

Complex **4** [B(2,4,6-Me₃-C₆H₂)₂] with the lowest decomposition energy has the weakest binding energy (-77.7). The high binding energy of complex **3** [BF₂] does not agree with the easy thermal decomposition, but this may be assigned to kinetic factors, which caused decomposition of the compound even in normal handling. The relative thermal stability of **6** (9-borafluorenyl), as measured by T_{dec 5%} (Table 1), is slightly different than might be anticipated from its BE of -143.0.

Table S3. Energy Decomposition Analysis (EDA) of complexes **3-9**.

EDA terms							
	3	4	5	6	7	8	9
ΔE_{Pauli}	213.6	336.2	314.8	269.9	628.0	297.3	595.5
ΔE_{elec}	-338.6	-314.2	-339.7	-304.6	-759.9	-311.4	-700.4
ΔE_{steric}	-125.0	22.0	-24.9	-34.7	-131.9	-14.1	-104.9
ΔE_{orb}	-251.1	-269.7	-292.3	-263.2	-582.4	-261.5	-523.5
ΔE_{solv}^a	-132.5	-87.3	-110.5	-99.4	-291.3	-95.2	-256.8
ΔE_{int}	-243.6	-160.4	-206.7	-198.5	-423.0	-180.4	-371.6
$\Delta E_{reorg-ImPyrr}$	23.0	21.5	23.8	23.6	48.3	22.6	46.5
$\Delta E_{reorg-BX_2}$	67.2	61.2	51.4	31.9	104.6	45.8	91.6
ΔE_{reorg}	90.2	82.7	75.2	55.5	152.9	68.4	138.1
BE	-153.4	-77.7	-131.5	-143.0	-270.1	-112.0	-233.5

^a The solvation energy of the fragments is subtracted.^{23c}

NMR spectra of complexes 3-7

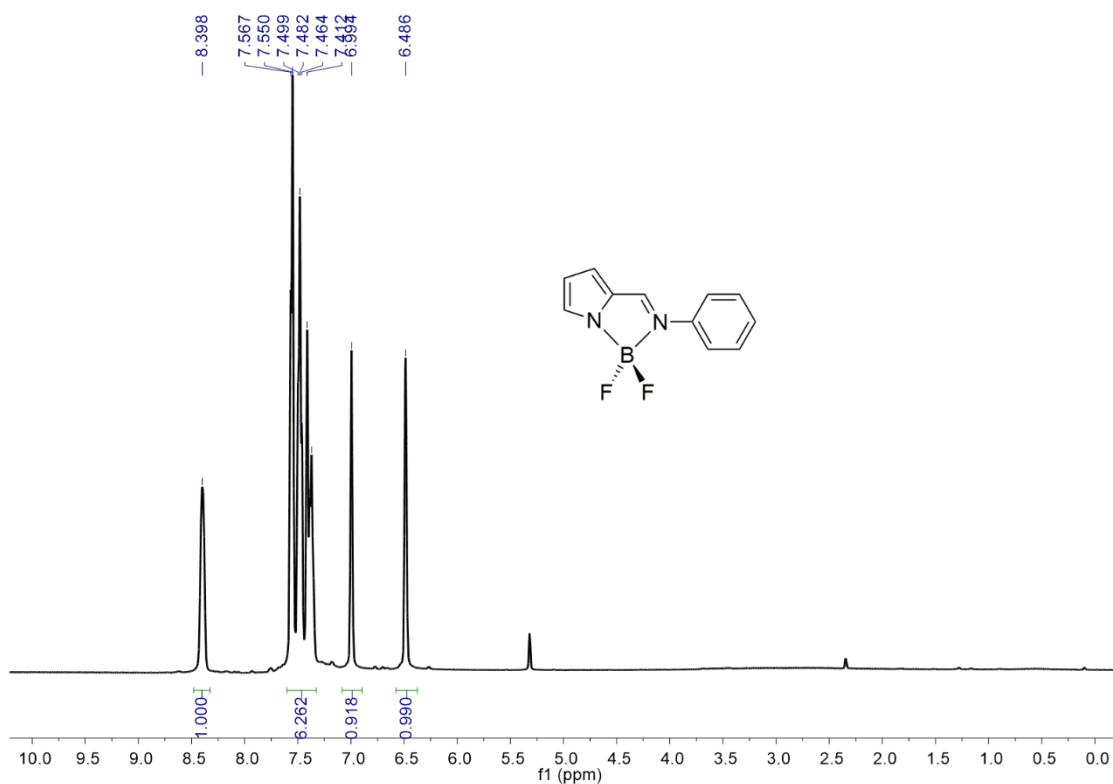


Figure S8. ¹H NMR spectrum (400 MHz, CD₂Cl₂) of complex **3**.

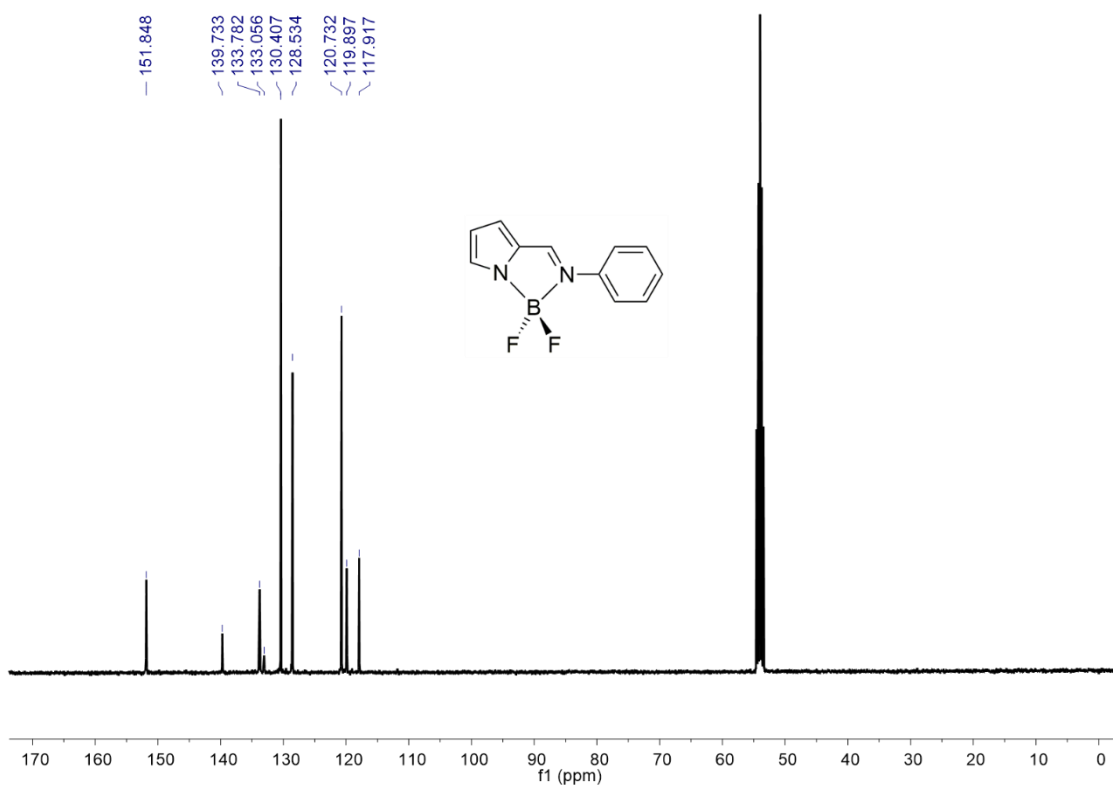


Figure S9. ¹³C{¹H} NMR spectrum (100.61 MHz, CD₂Cl₂) of complex **3**.

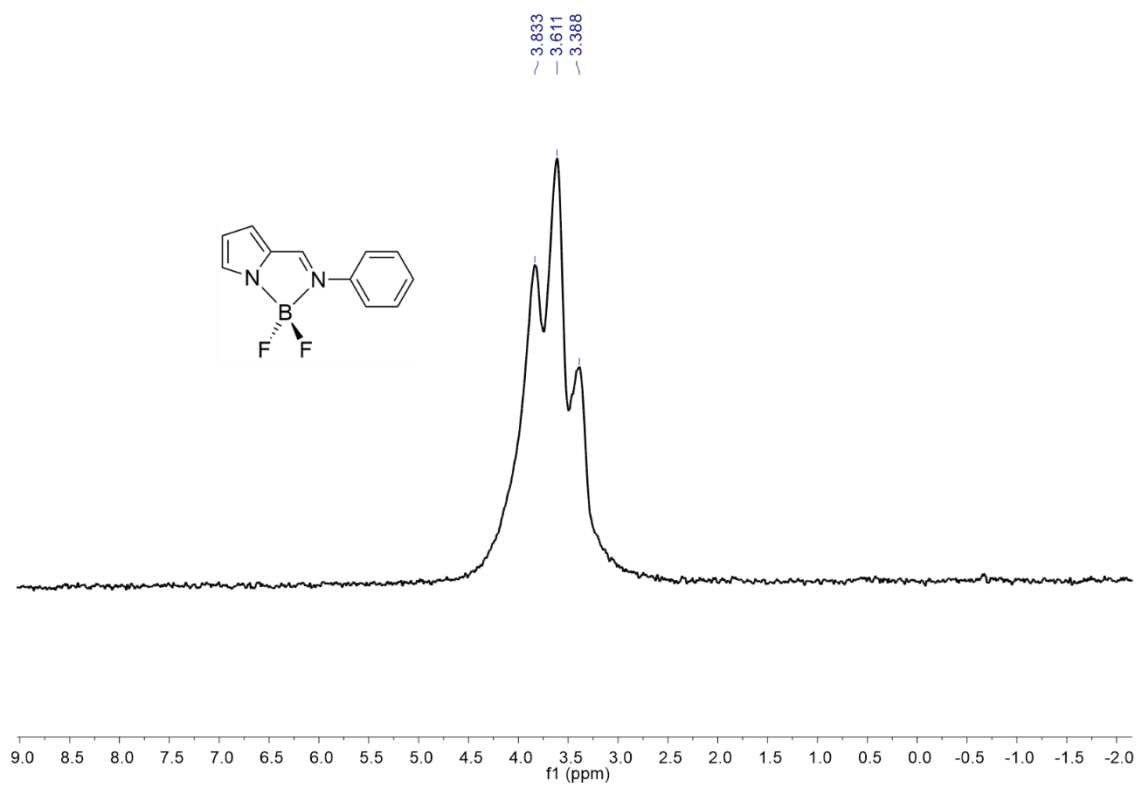


Figure S10. ^{11}B NMR spectrum (128.35 MHz, CD_2Cl_2) of complex **3**.

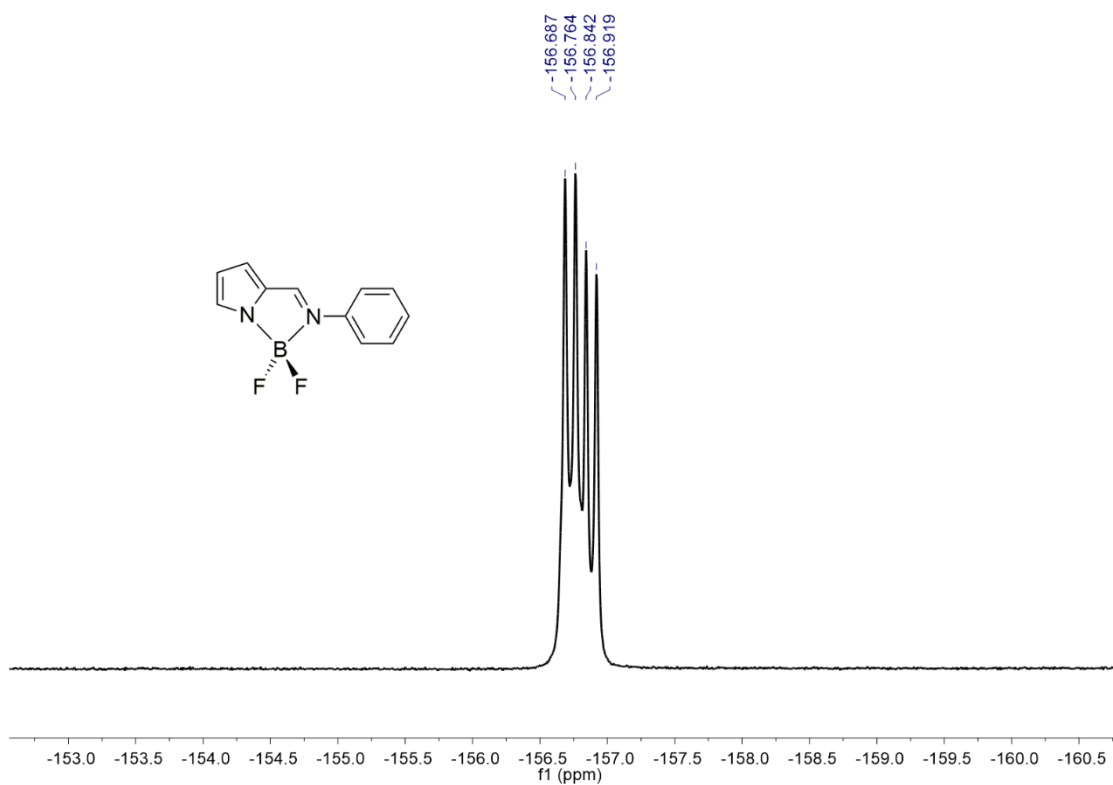


Figure S11. $^{19}\text{F}\{^1\text{H}\}$ NMR spectrum (376.50 MHz, CD_2Cl_2) of complex **3**.

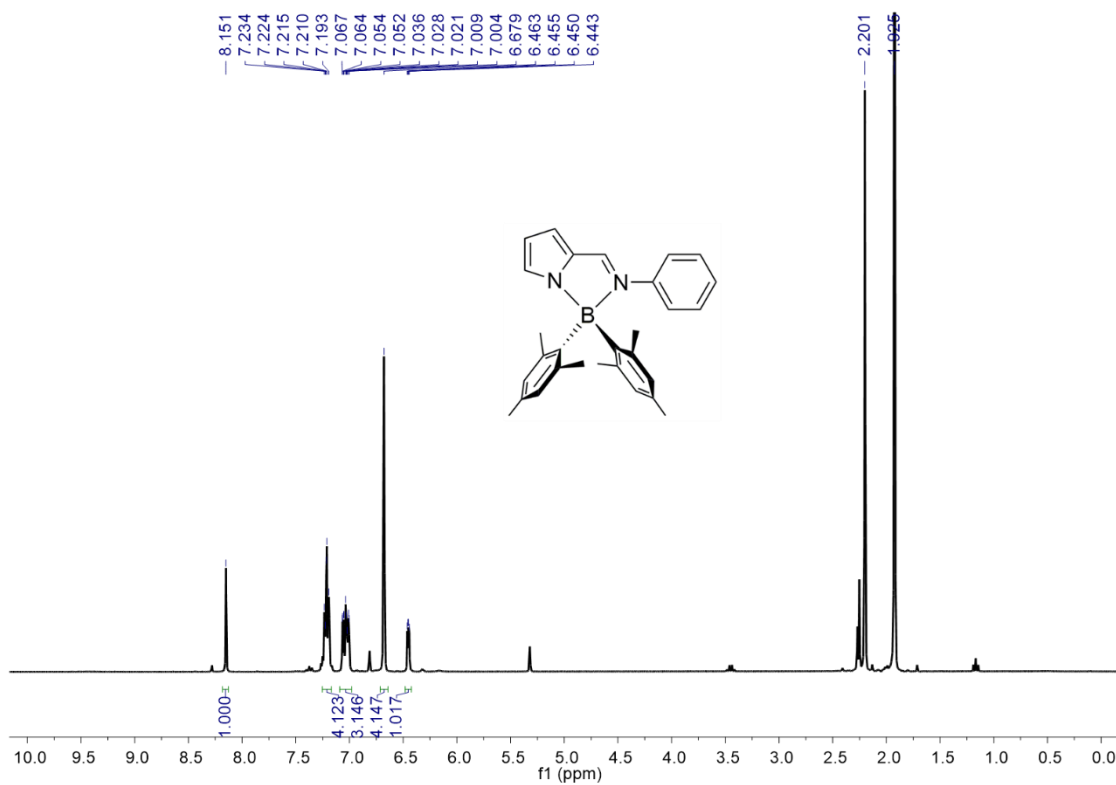


Figure S12. ¹H NMR spectrum (300 MHz, CD₂Cl₂) of complex 4.

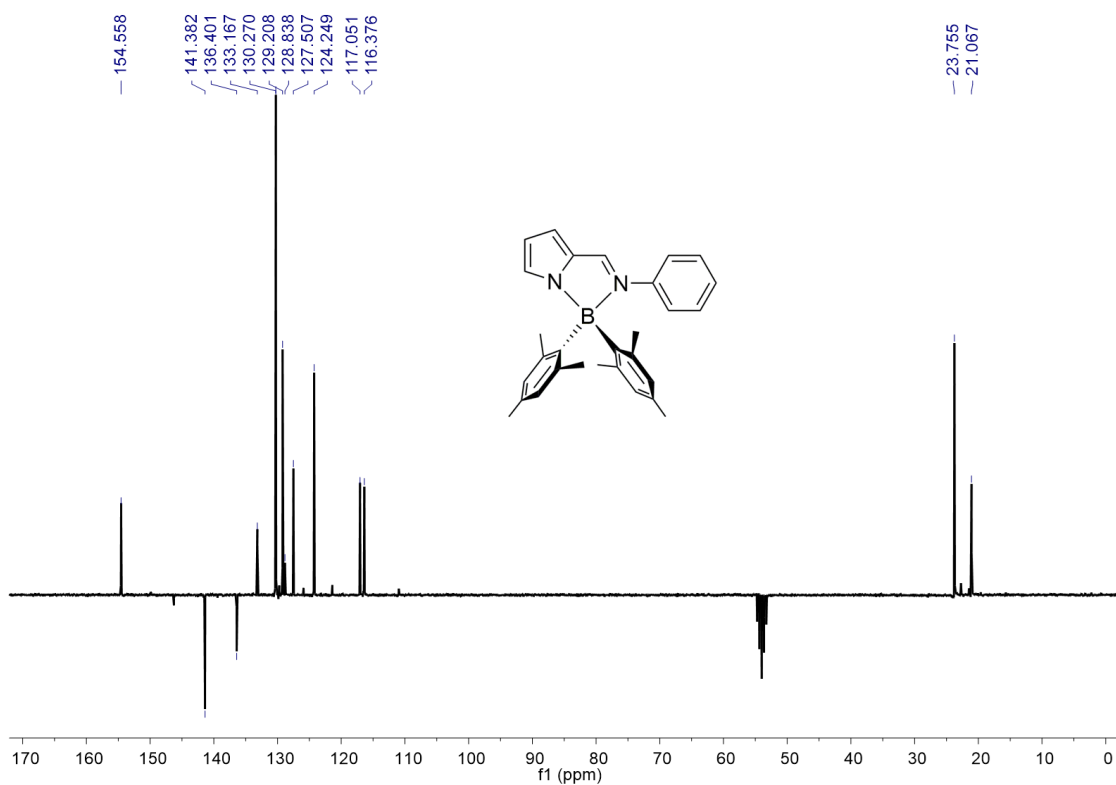


Figure S13. ¹³C APT NMR spectrum (75.47 MHz, CD₂Cl₂) of complex 4.

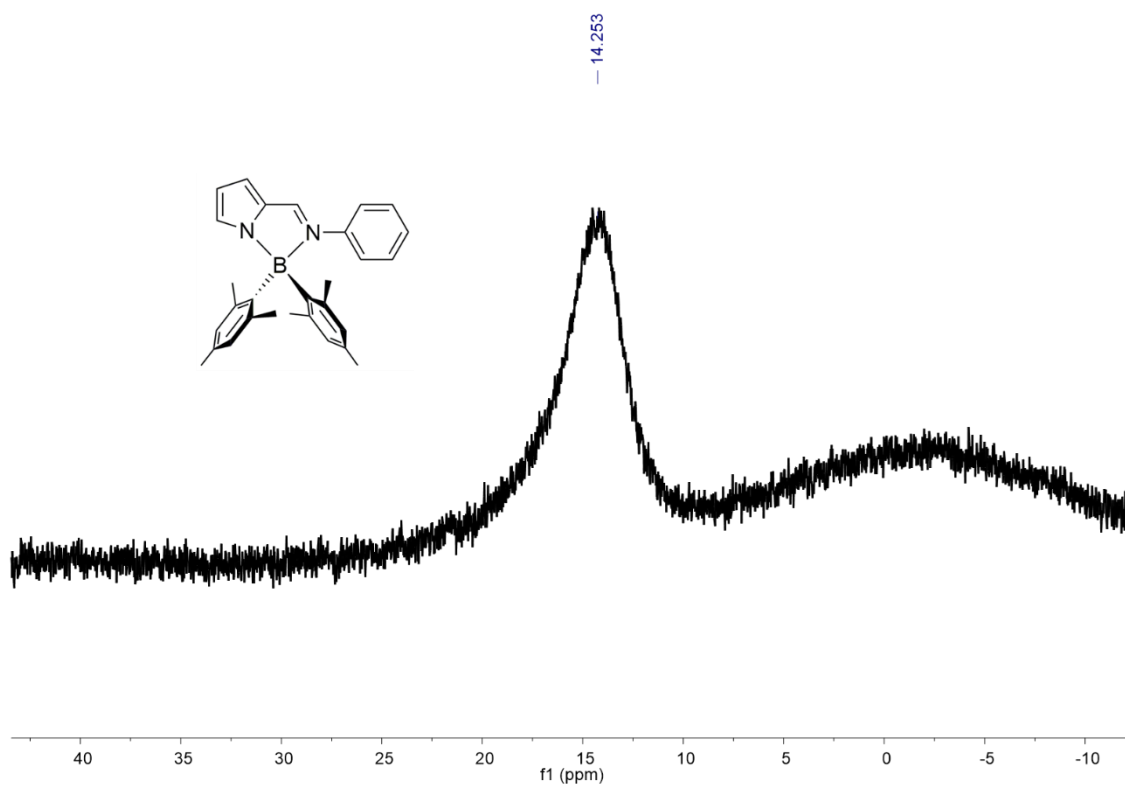


Figure S14. ^{11}B NMR spectrum (96.27 MHz, CD_2Cl_2) of complex **4**.

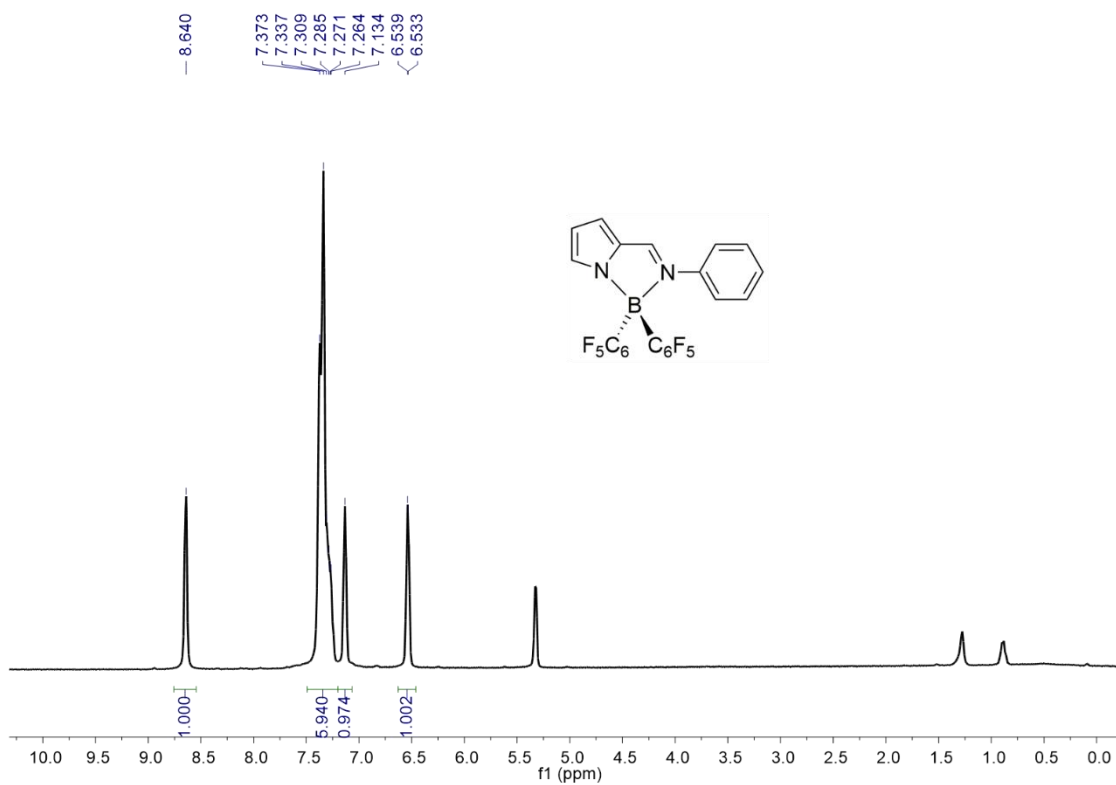


Figure S15. ¹H NMR spectrum (300 MHz, CD₂Cl₂) of complex 5.

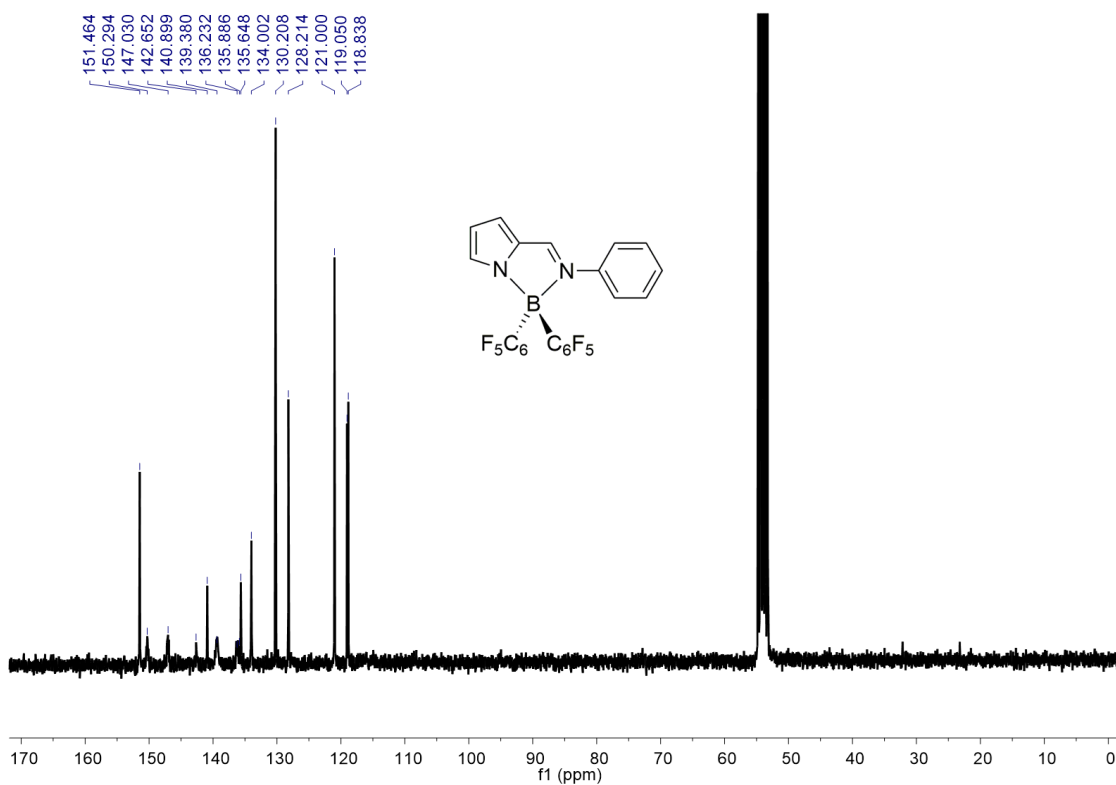


Figure S16. ¹³C{¹H} NMR spectrum (75.47 MHz, CD₂Cl₂) of complex 5.

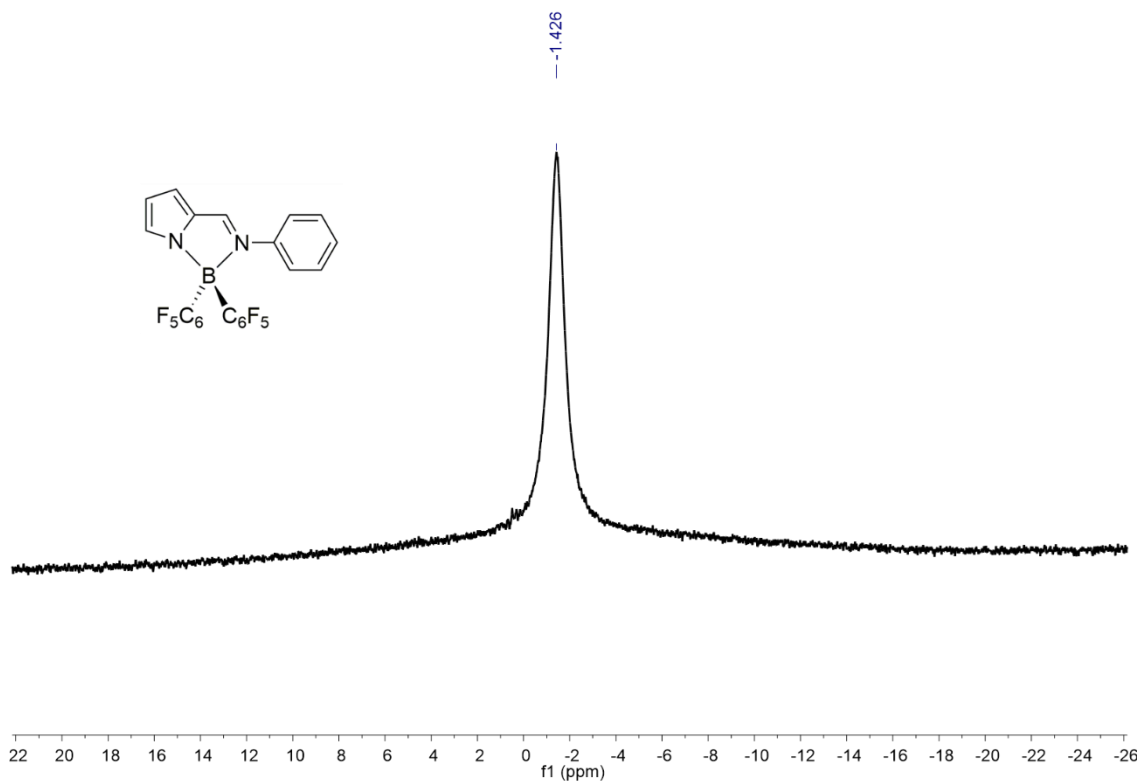


Figure S17. ^{11}B NMR spectrum (96.27 MHz, CD_2Cl_2) of complex **5**.

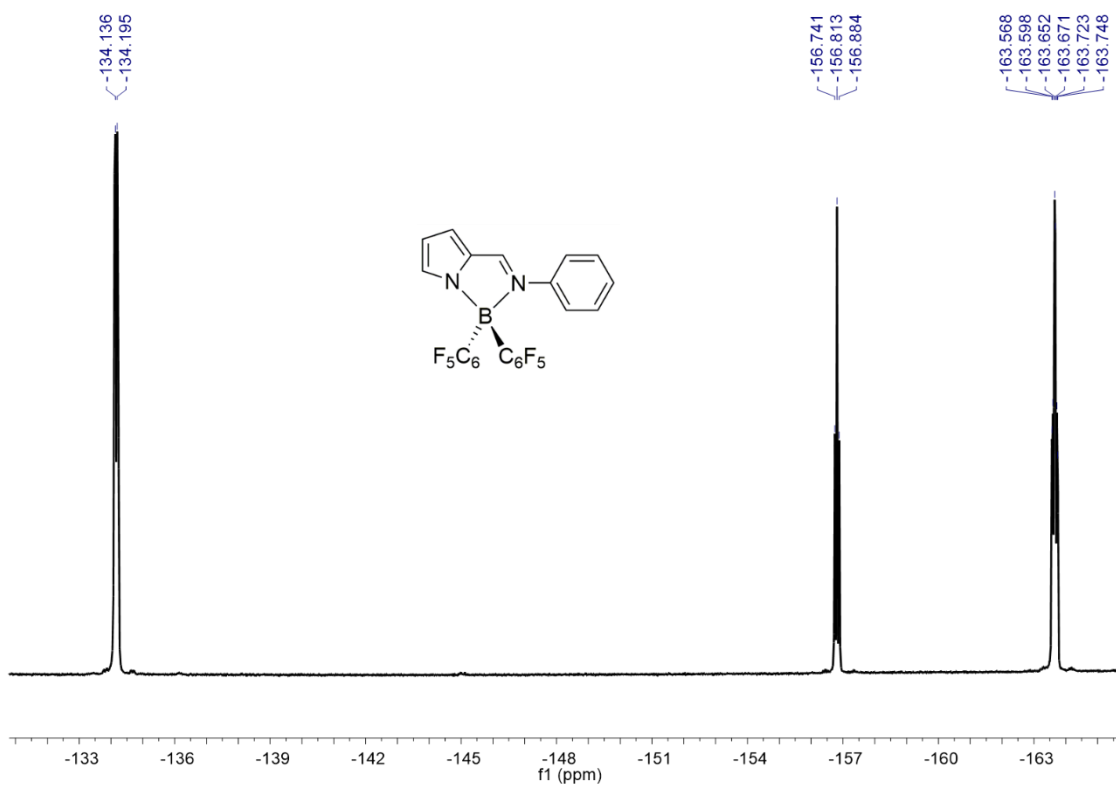


Figure S18. $^{19}\text{F}\{^1\text{H}\}$ NMR spectrum (282.40 MHz, CD_2Cl_2) of complex **5**.

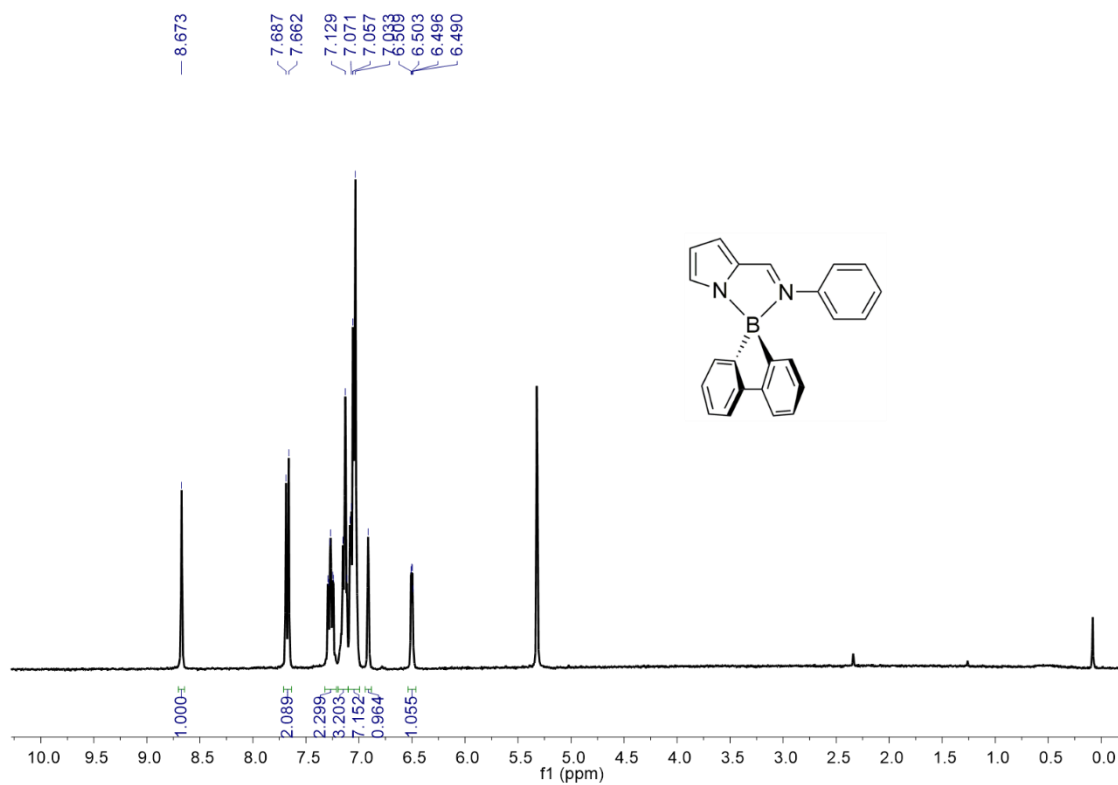


Figure S19. ^1H NMR spectrum (300 MHz, CD_2Cl_2) of complex **6**.

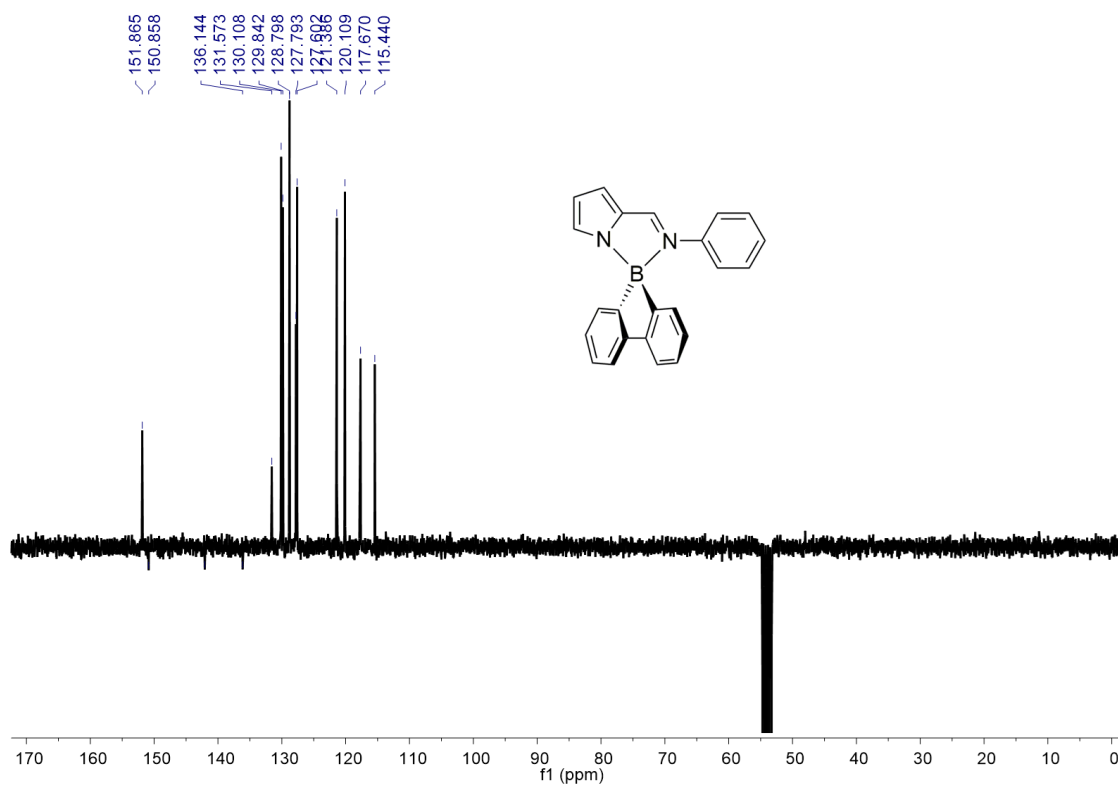


Figure S20. ^{13}C APT NMR spectrum (75.47 MHz, CD_2Cl_2) of complex **6**.

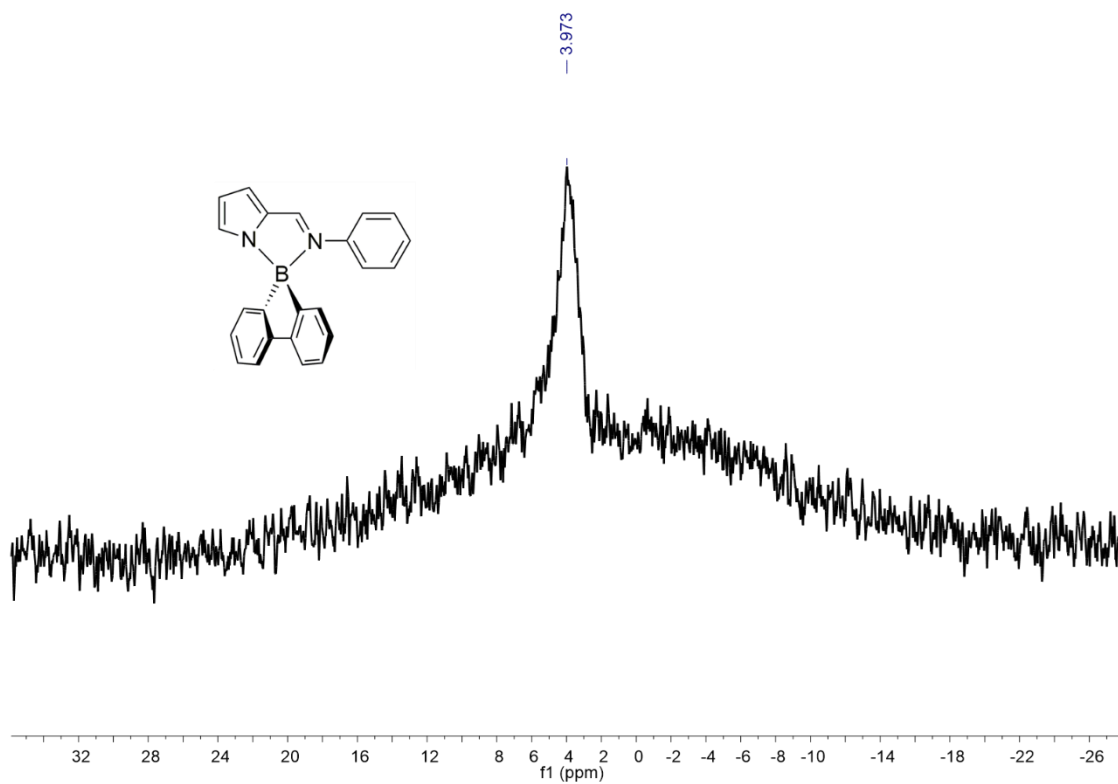


Figure S21. ^{11}B NMR spectrum (96.27 MHz, CD_2Cl_2) of complex **6**.

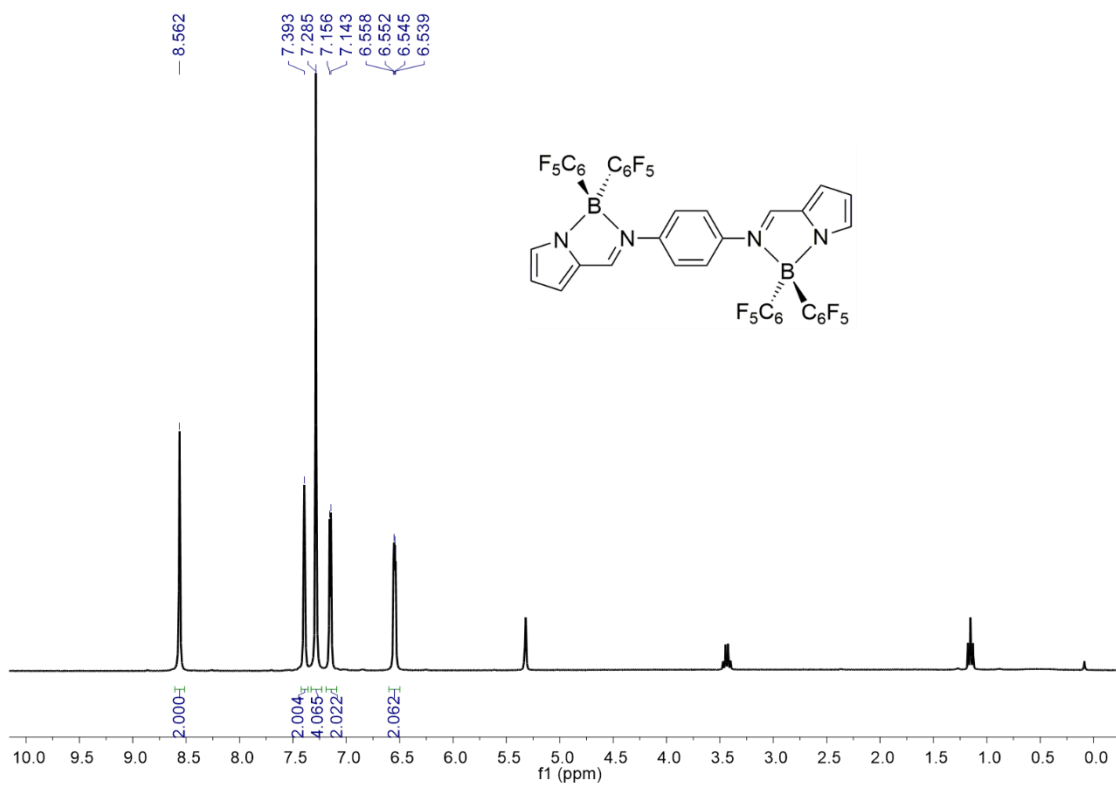


Figure S22. ^1H NMR spectrum (300 MHz, CD_2Cl_2) of complex 7.

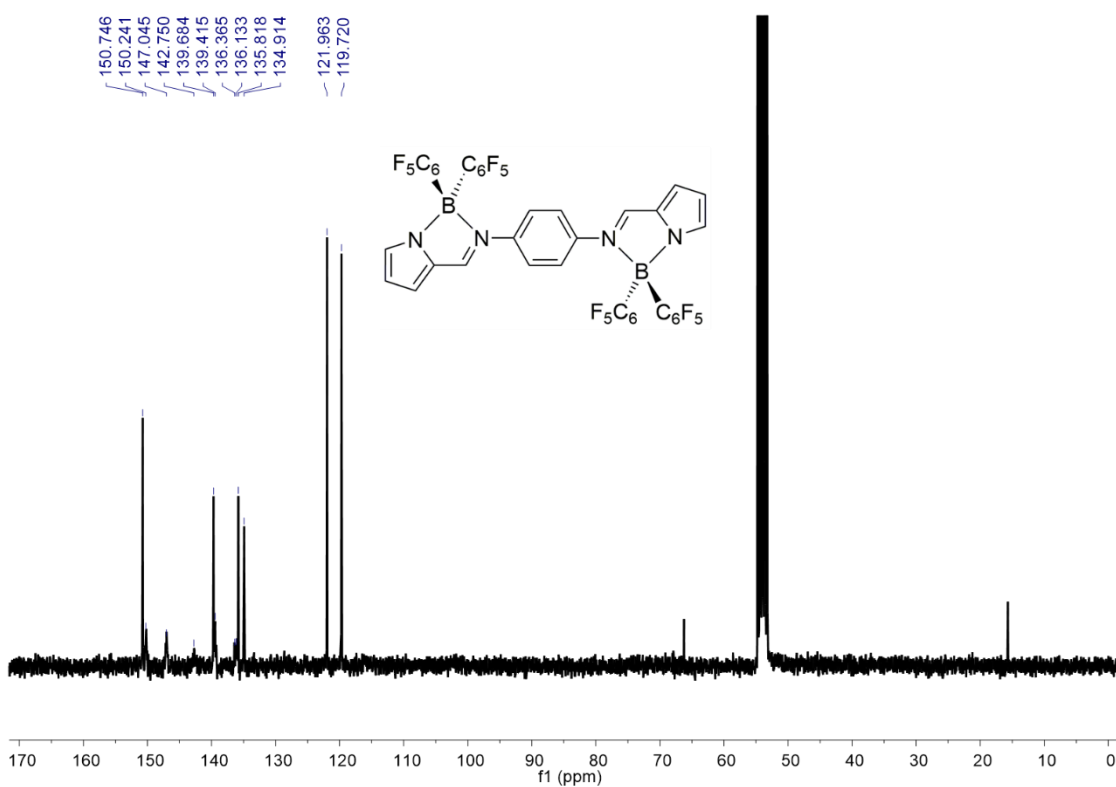


Figure S23. $^{13}\text{C}\{^1\text{H}\}$ NMR spectrum (75.47 MHz, CD_2Cl_2) of complex 7.

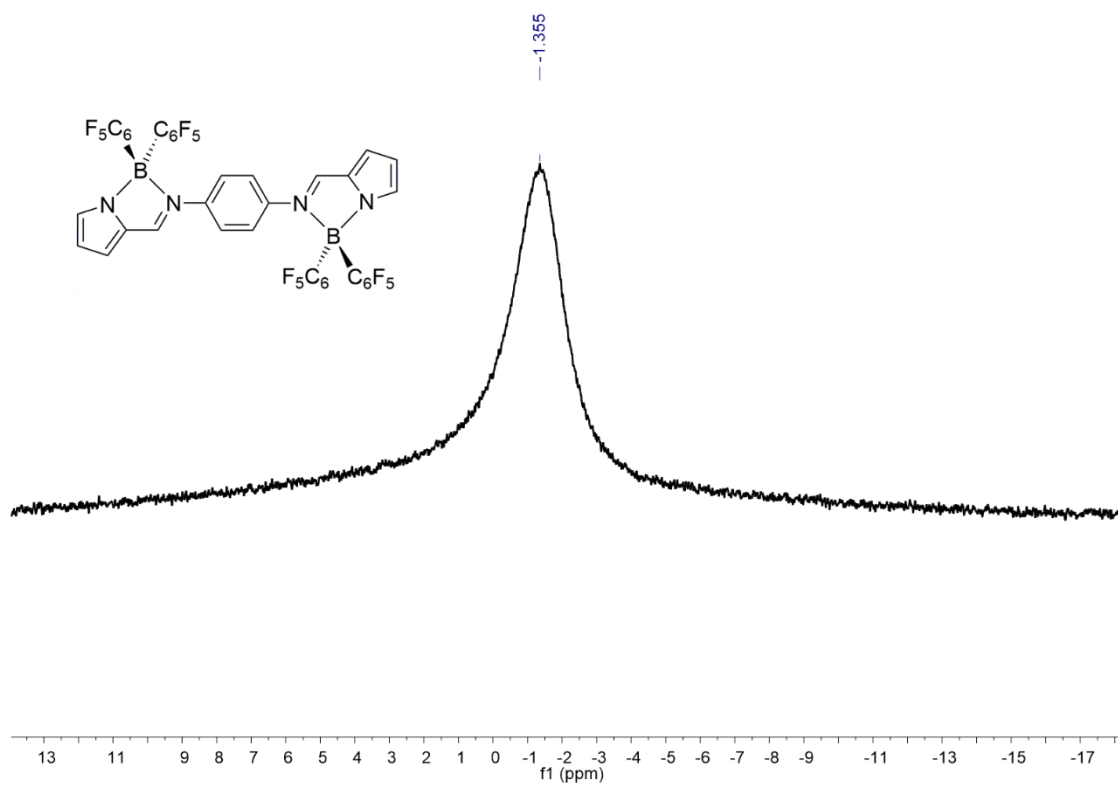


Figure S24. ^{11}B NMR spectrum (96.27 MHz, CD_2Cl_2) of complex **7**.

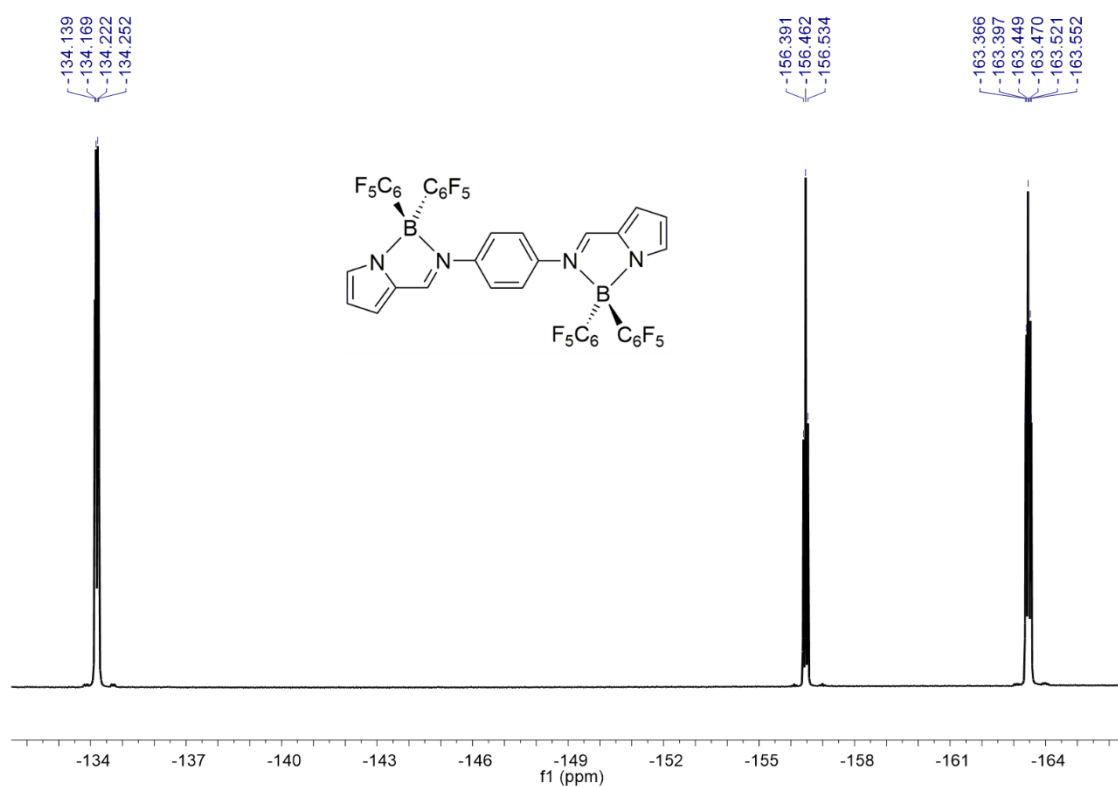


Figure S25. $^{19}\text{F}\{^1\text{H}\}$ NMR spectrum (282.40 MHz, CD_2Cl_2) of complex **7**.

Variable-temperature (VT) NMR spectra of complex **4**

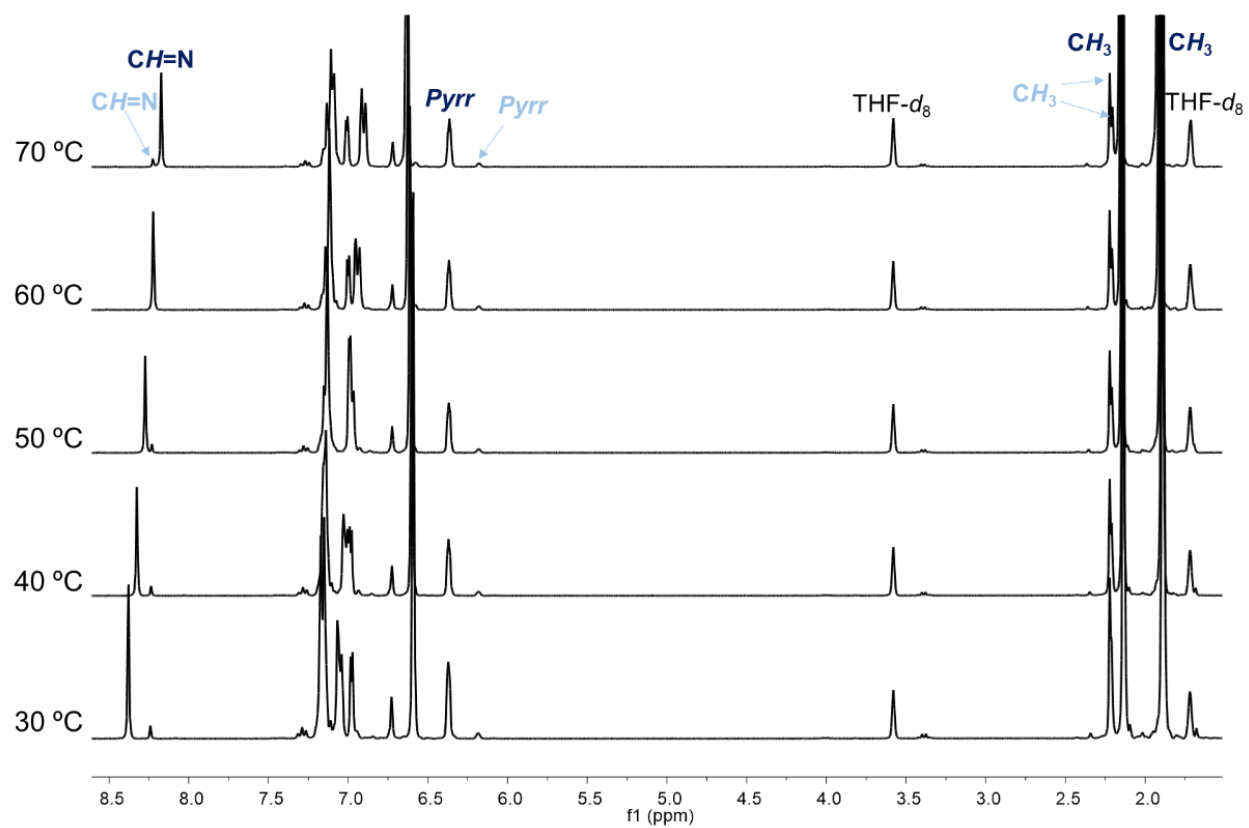


Figure S26. VT-¹H NMR spectra (300 MHz, THF-*d*₈) of complex **4**, showing the resonances of the tetracoordinate major isomer **4** (deep blue labels) and of the tricoordinate minor isomer **4**₃ (light blue labels).

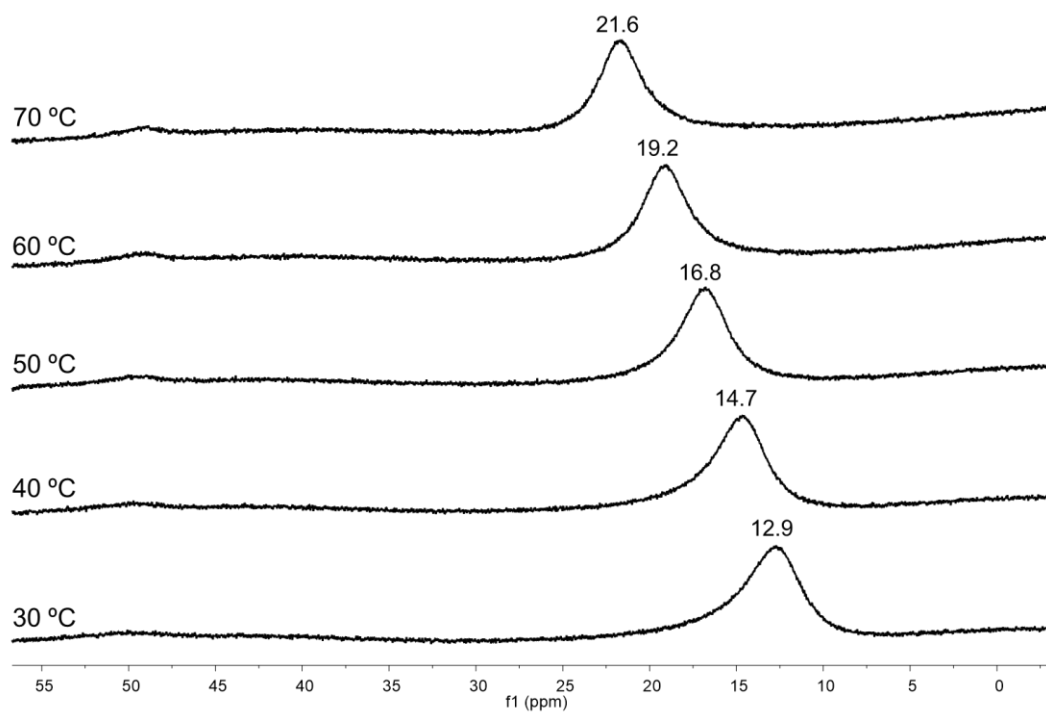


Figure S27. VT-¹¹B NMR spectra (96.29 MHz, THF-*d*₈) of complex **4**, showing the resonances of the tetracoordinate major isomer **4** (at lower fields) and the tricoordinate minor isomer **4**₃ (at higher fields), along with the respective chemical shifts.

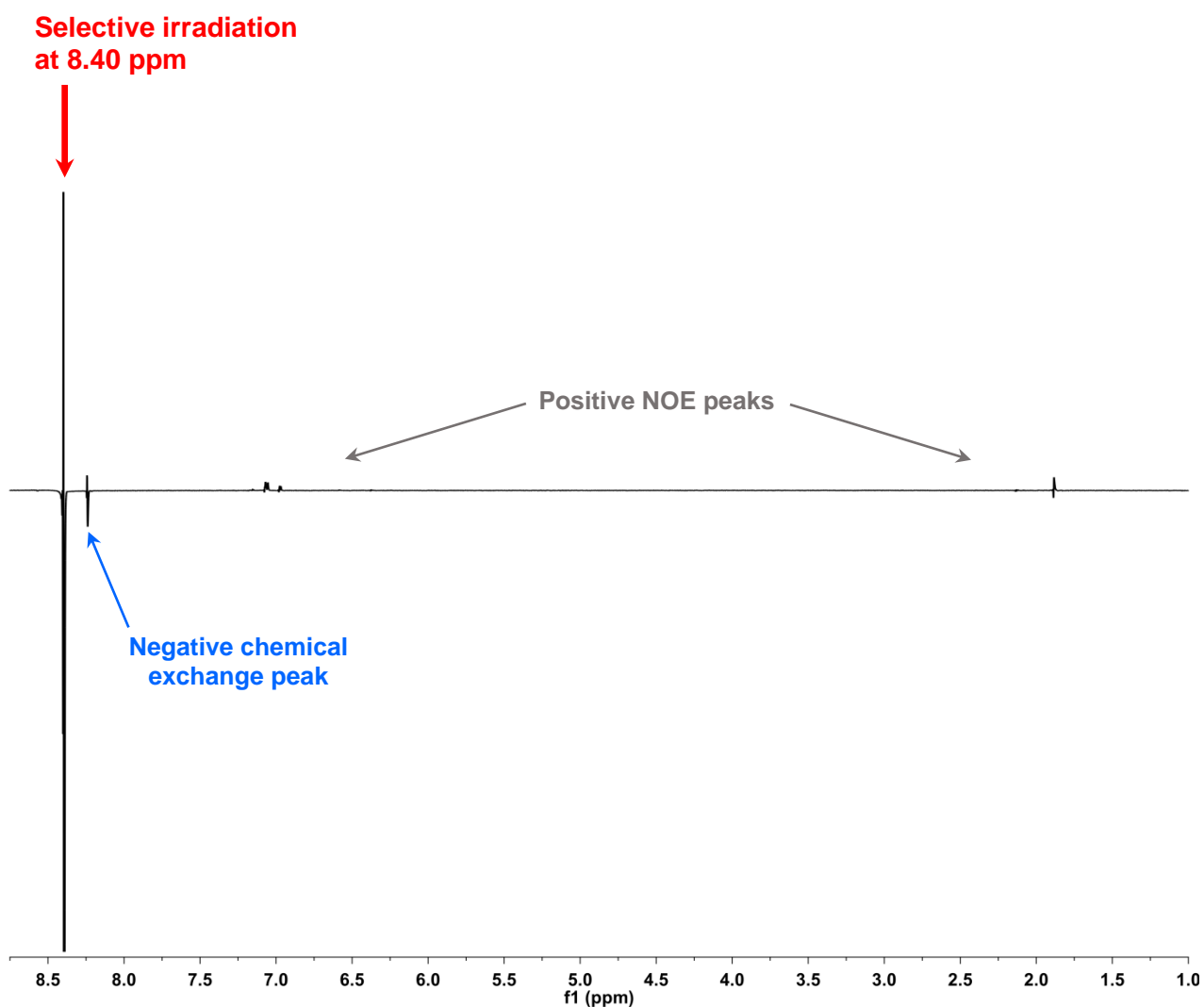


Figure S28. 1D-NOE NMR spectrum (300 MHz, THF-*d*₈, 29 °C) of complex **4**, with selective irradiation on the ¹H imine proton (-CH=N-) resonance of tetracoordinate major isomer **4**, at 8.40 ppm, showing its chemical exchange with the tricoordinate minor isomer **4**₃ (negative NOE peak) and positive NOE peaks with pyrrolyl, aromatic and methyl protons.

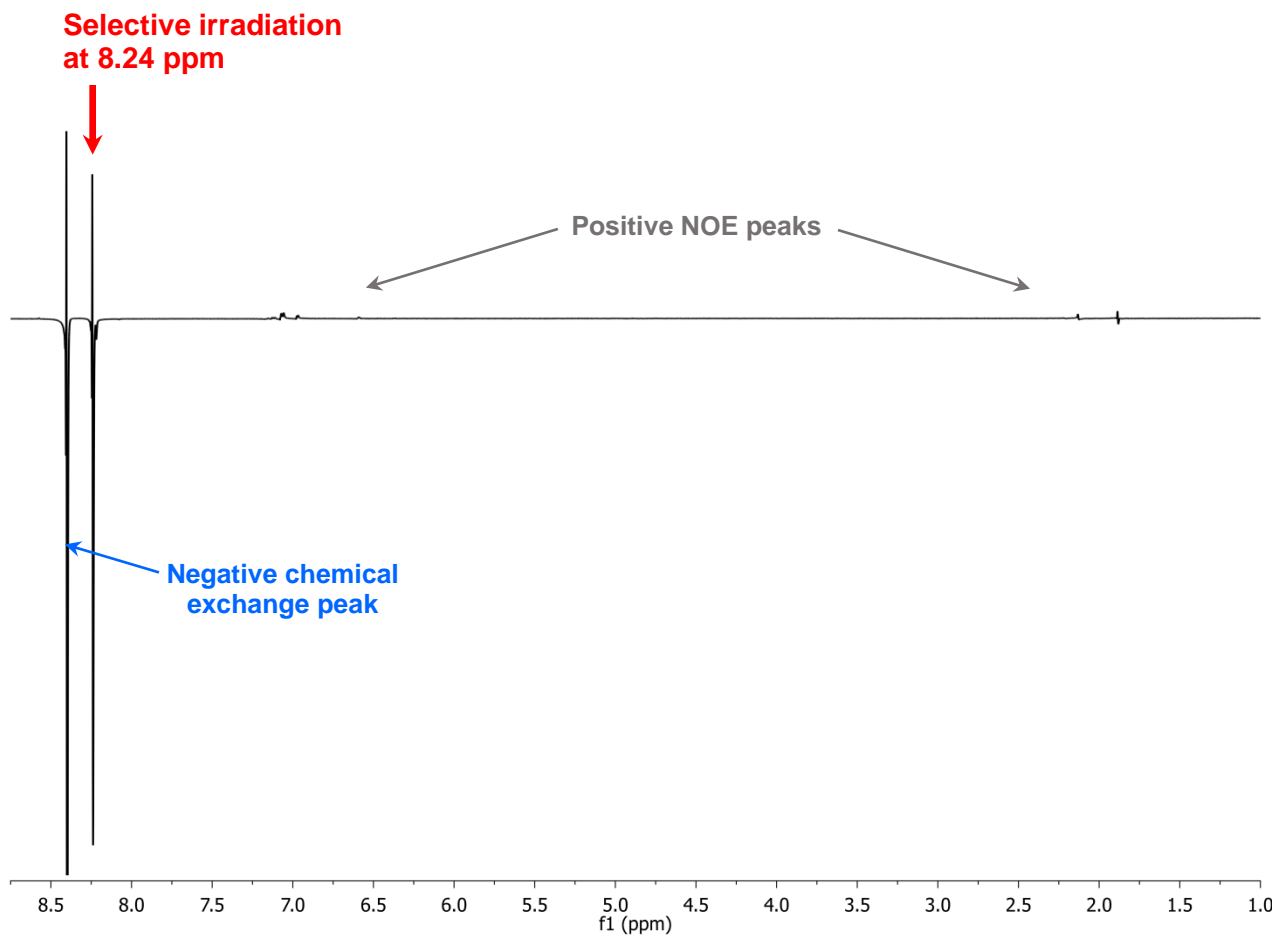


Figure S29. 1D-NOE NMR spectrum (300 MHz, THF-*d*₈, 29 °C) of complex **4**, with selective irradiation on the ¹H imine proton (-CH=N-) resonance of tricoordinate *minor isomer 4₃*, at 8.24 ppm, showing its chemical exchange with the tetracoordinate *major isomer 4* (negative NOE peak) and positive NOE peaks with pyrrolyl, aromatic and methyl protons.

Van't Hoff plot for the equilibrium between tetracoordinate and tricoordinate isomers of complex 4

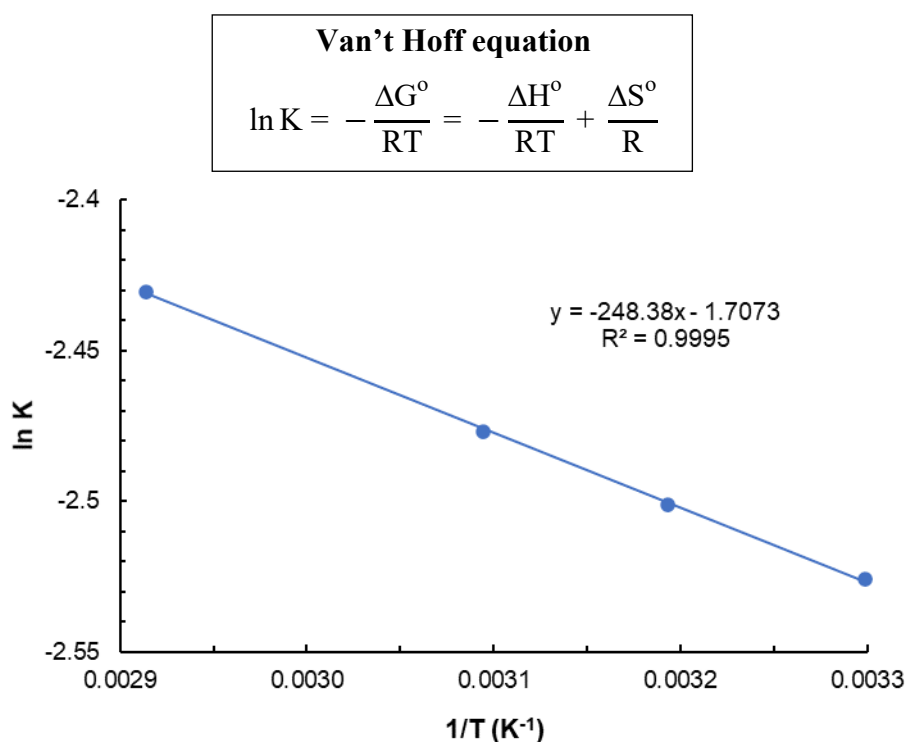


Figure S30. Van't Hoff plot for the equilibrium between tetracoordinate and tricoordinate isomers of complex 4.

T (°C)	T (K)	1/T	I _{tricoord} ^a	I _{tetracoord} ^a	K ^b
30	303.15	0.003299	0.080	1	0.080
40	313.15	0.003193	0.082	1	0.082
50	323.15	0.003095	0.084	1	0.084
60	333.15	0.003002	^c	1	^c
70	343.15	0.002914	0.088	1	0.088

^a Calculated from the relative area integration of the corresponding imine (-CH=N-) ¹H NMR resonances; ^b Equilibrium constant: K = [4₃]/[4] = I_{tricoord}/I_{tetracoord}; ^c Not calculated because both resonances are overlapping.

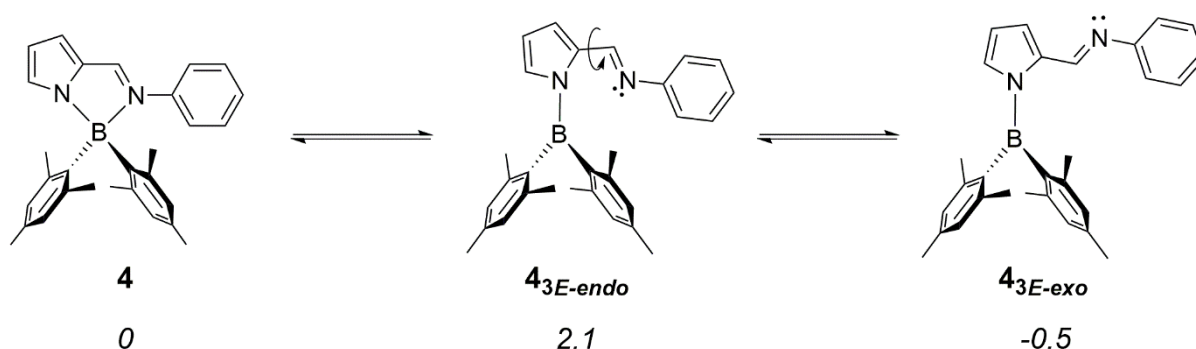
Thermodynamic parameters: $\Delta H^\circ = 0.49 \pm 0.04 \text{ kcal mol}^{-1}$

$\Delta S^\circ = -3.4 \pm 0.1 \text{ cal mol}^{-1} \text{ K}^{-1}$

$\Delta G^\circ (298.15 \text{ K}) = 1.51 \pm 0.07 \text{ kcal mol}^{-1}$

Computational studies – Energy profile for the conversion of complex **4 into the tricoordinate isomers **4**_{3E-endo} and **4**_{3E-exo} and comparison with mononuclear boron complexes **3**, **5**, **6** and **8****

It was shown in Scheme 2 of the article that the tetracoordinate 2-iminopyrrolyl boron complex **4** was involved in an equilibrium with the **4**_{3E-endo} isomer, which could further convert to **4**_{3E-exo}. Our calculations indeed show that the B-N_{imine} bond of complex **4** can be easily broken to yield a tricoordinate boron complex containing the monodentate iminopyrrolyl ligand in the *E-endo* form (**4**_{3E-endo}) with an energy 2.1 kcal mol⁻¹ higher. Rotation around the C_{pyrrolyl}-C_{imine} converts it to a 2.6 kcal mol⁻¹ more stable *E-exo* conformer (**4**_{3E-exo}) with almost the same energy of **4**, though slightly more stable. A new version of Scheme 2 with these energies is shown in Scheme S1.



Scheme S1. Schematic equilibrium between the tetracoordinate 2-iminopyrrolyl boron complex **4** and its tricoordinate isomers **4**_{3E-endo} and **4**_{3E-exo}, with their relative energies in kcal mol⁻¹ (in italics).

This result suggests that the long B-N_{imine} bond is weak, and its cleavage relieves the steric hindrance of the initial complex **4**. Nothing similar happens with the other four mononuclear complexes studied, where the energy differences are closer to 20 kcal mol⁻¹ (see Figure S31). The **6**_{3E-endo} isomer of **6** could not be obtained. Therefore, only tetracoordinate complex **4** may be involved in a decoordination-coordination equilibrium process in solution with its corresponding tricoordinate species as represented in Scheme S1.

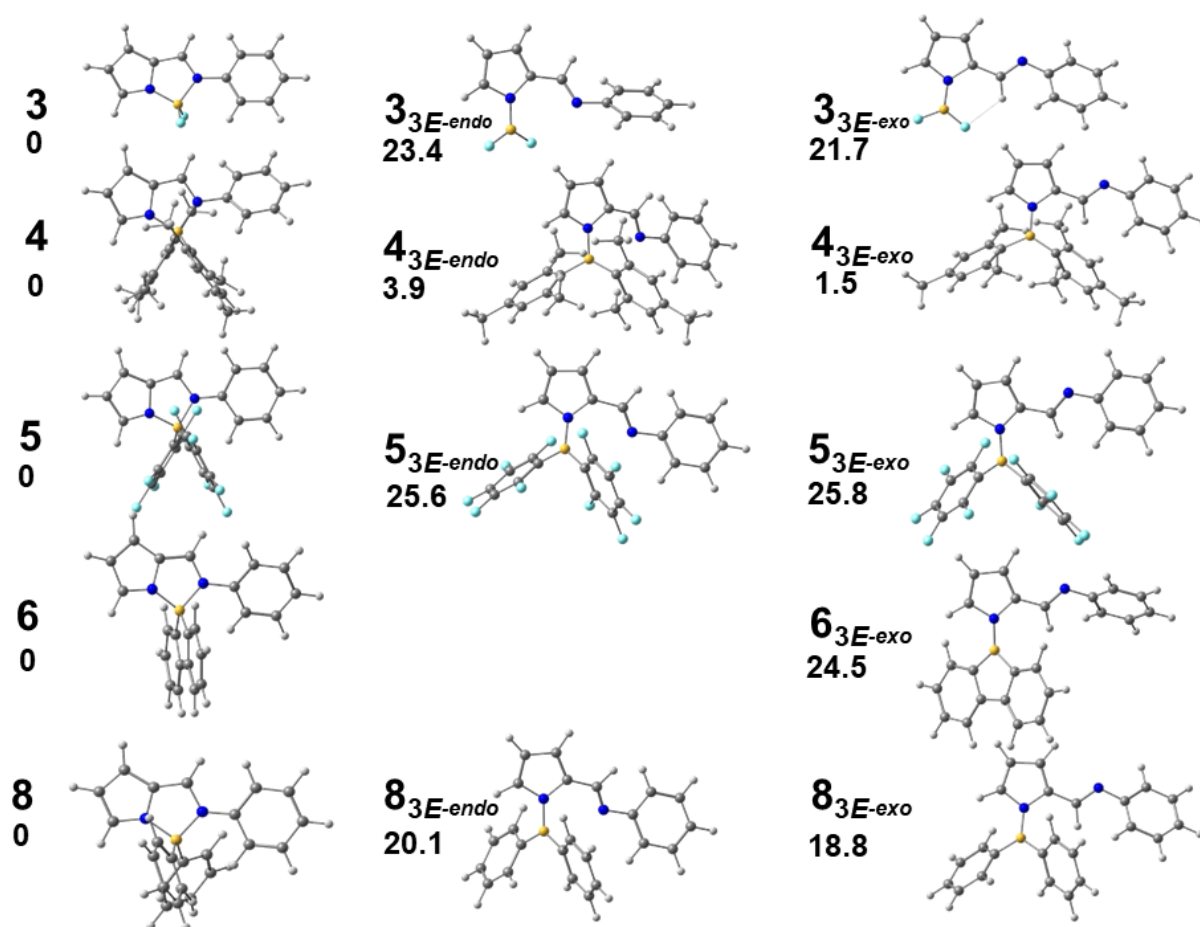


Figure S31. Optimised ground state structures of tetracoordinate mononuclear boron complexes **3-6** and **8** (left), of their tricoordinate *E-endo* conformers (center, except **6**_{3E-endo}) and tricoordinate *E-exo* conformers (right), with the relative energy difference (kcal mol⁻¹) below the complex label.

The previous observations led us to search for the energy profile of **4**, **4**_{3E-endo} and **4**_{3E-exo} (bottom) of the two reactions shown in Scheme S1 and to determine the two transition states, TS1 and TS2, respectively (see Computational details for the methodology). The description of the mechanism is presented in Figure S30 (displayed in the article as Figure 2, which is repeated here for facility).

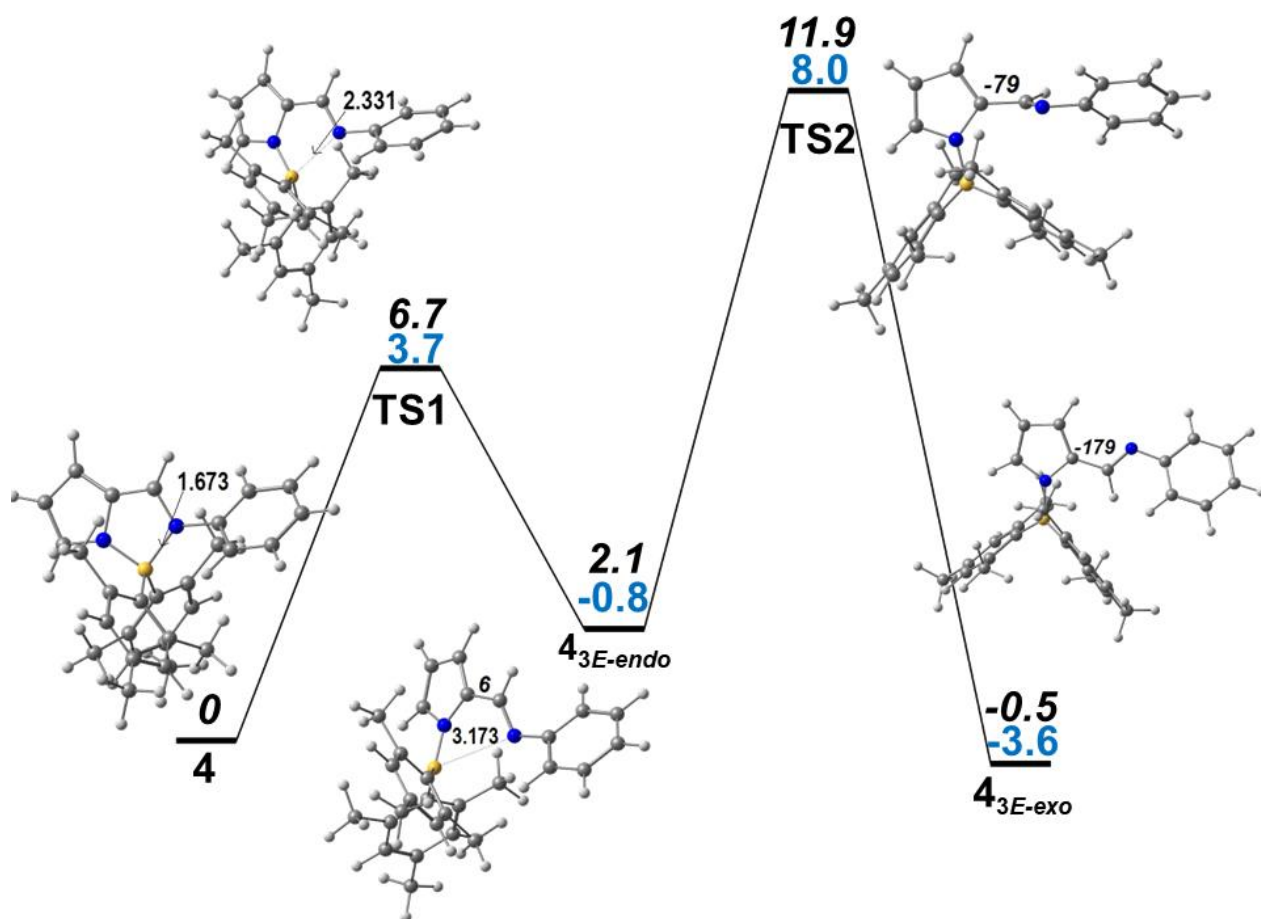


Figure S32. Energy profile (BP86 functional) for the conversion of complex **4** into the tricoordinate complex **4**_{3E-endo} and isomerization to **4**_{3E-exo} (bottom), with the relative energies (black) and Gibbs energies (blue) in kcal mol⁻¹, and the geometries of the five species with indication of the parameter changing in each step (distances in Å in TS1 and C-C-C-N dihedral angles in ° in TS2).

The stretching of the B-N_{imine} bond of **4** shows an energy maximum, which led to the transition state at a distance of 2.331 Å and to the tricoordinate boron complex **4**_{3E-endo} for $d(\text{B-N}_{\text{imine}}) = 3.173$ Å, which is well beyond any bonding distance. The small energy barrier is 6.7 kcal mol⁻¹. If we consider the Gibbs energies values, the tetra- and tricoordinate boron complexes differ by only 0.8 kcal mol⁻¹, the latter becoming more stable than **4**. It is therefore expectable that both species **4** and **4**_{3E-endo} could be seen in solution by NMR experiments, as discussed above. While looking for meaningful species, we envisaged also the **4**_{3E-exo} isomer, which is obtained by rotating the -C(H)=N-Ph imine group across the internal C_{pyrrolyl}-C_{imine} bond of the iminopyrrolyl. This angle starts as 2° in **4**, with the C=N imine bond almost coplanar with the pyrrolyl ring and is only 6° in **4**_{3E-endo}, reaching -79° in TS2 and finally -179° in **4**_{3E-exo}. The C=N imine bond of **4**_{3E-exo} is again coplanar with the pyrrolyl

ring but in the *exo* conformation. The energy barrier is significantly higher and may prevent its formation. These values are very small, and the conclusion is that both **4** and **4**_{3E-endo} should be observed species. The presence of **4**_{3E-exo} is not so clear.

This latter point is further reflected in the similar calculations obtained with another methodology (Figure S33). A comparison of experimental and calculated thermodynamic functions for the equilibrium between **4** and **4**_{3E-endo} reveals that the enthalpies are in very good agreement, with 0.6 (calc) and 0.5 (exp) kcal mol⁻¹, while the Gibbs energies, -0.8 (calc) and 1.5 (exp) kcal mol⁻¹ differ a little more, though being of the same order of magnitude. This not so good agreement is explained by the limitations in the calculations of the entropy.

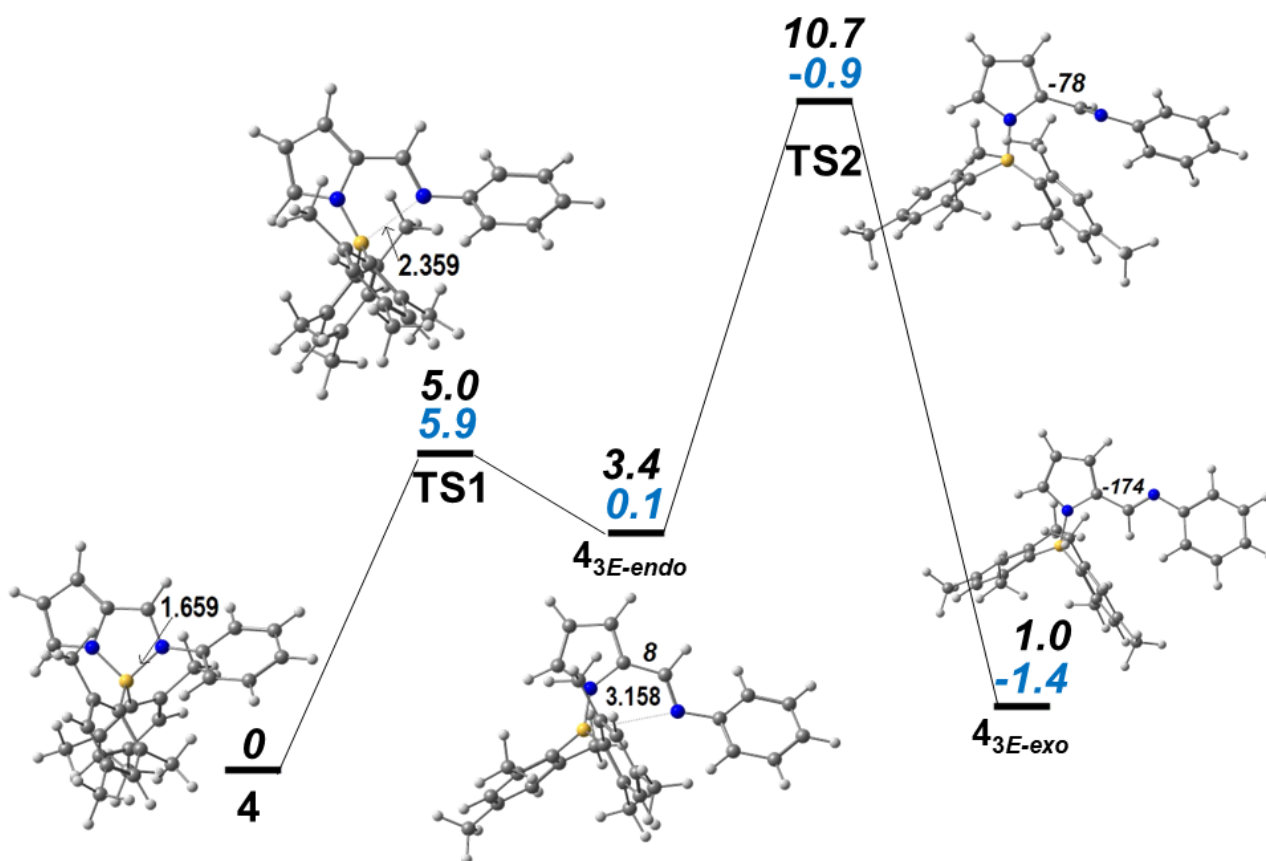


Figure S33 Energy profile (PBE functional) for the conversion of complex **4** into the tricoordinate complex **4**_{3E-endo} and isomerization to **4**_{3E-exo} (bottom), with the relative energies (black) and Gibbs energies (blue) in kcal mol⁻¹, and the geometries of the five species with indication of the relevant parameters (angles in ° and distances in Å).

**Computational studies – Ground state and first excited state optimised structure geometries
of boron complexes 3-9**

Table S4. Calculated (DFT) dihedral angles C6-N2-C7-C12 (°) for complexes **3-9** in the ground and first singlet excited state using different methods.

Angle	Ground state					First singlet excited state				
	A	B	A/D3	B/D3	GP	A	B	A/D3	B/D3	GP
	C6-N2-C7-C12									
3	-24	-27	-25	-28	-22	1	0	1	0	0
4	-49	-51	-53	-56	-48	13	13	14	15	9
5	23	25	23	24	23	8	8	8	8	9
6	30	33	30	29	30	5	5	5	5	0
7	22	24	21	23	22	10	11	10	11	10
	-22	-25	-21	-23	-21	-9	-11	-10	-11	-10
8	36	36	36	38	29	1	1	1	1	2
9	31	37	31	37	34	5	4	5	5	4
	-31	-37	-31	-37	-34	-5	-5	-5	-5	-4

A – PBE0, TZ2P (all electron), THF, SO

A/D3 – PBE0/D3, TZ2P (all electron), THF, SO

B – B3LYP, TZ2P (all electron), THF, SO

B/D3 – B3LYP/D3, TZ2P (all electron), THF, SO

GP – BP86 (small core, TZ2P)

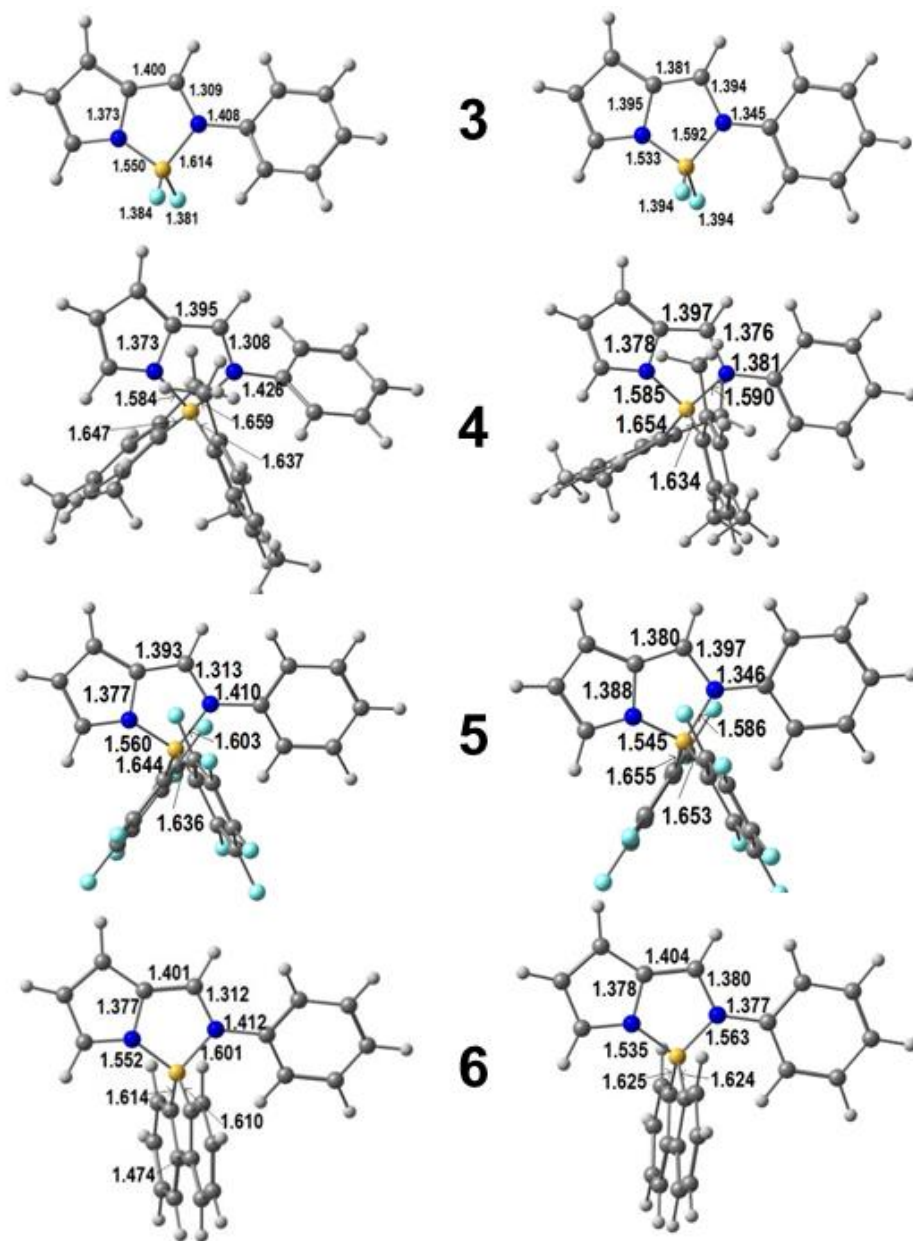


Figure S34. Optimised structures of tetracoordinate boron complexes **3-6** in the ground state (left) and in the first excited singlet state (right), with the most relevant distances (Å).

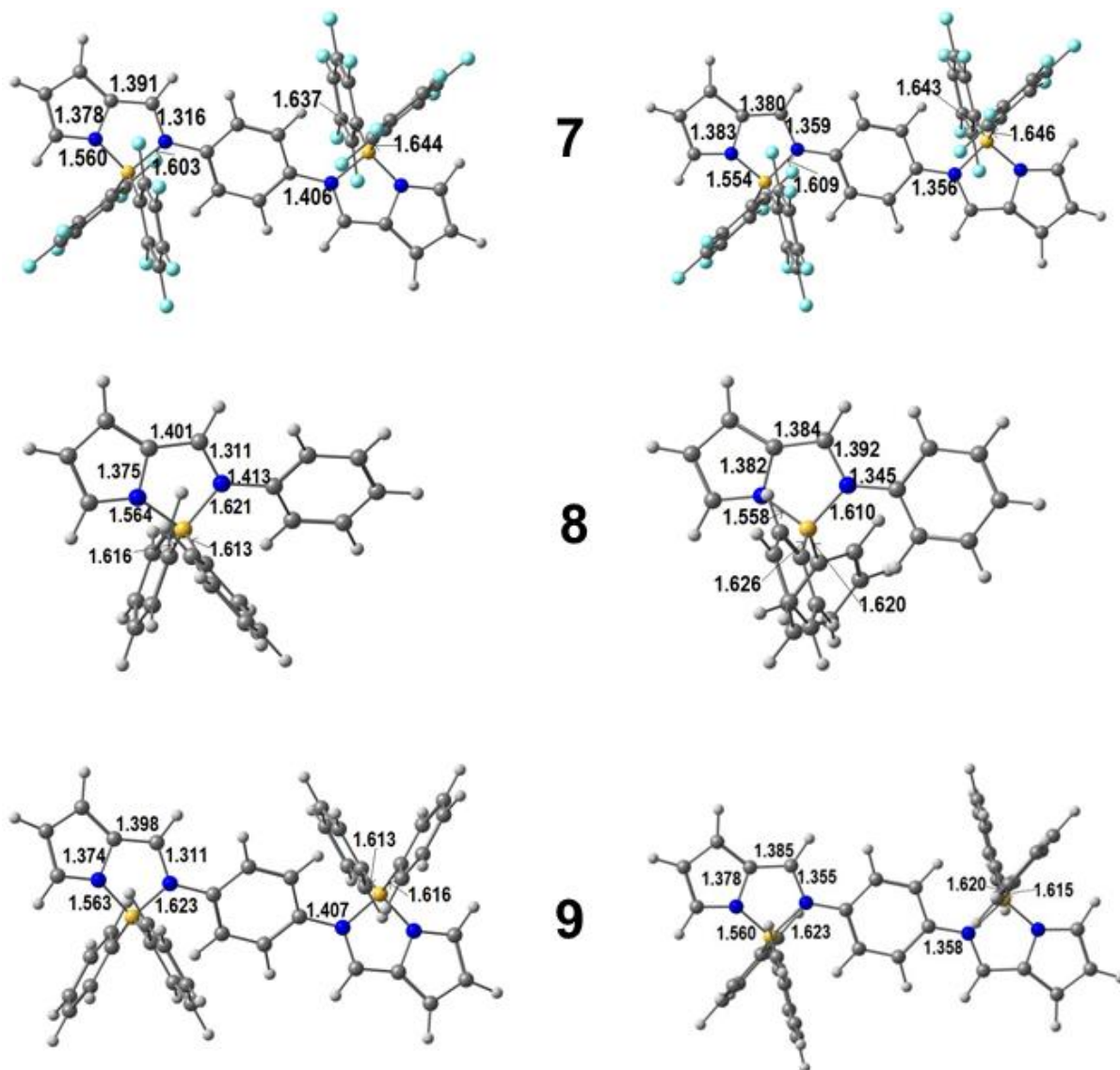


Figure S35. Optimised structures of tetracoordinate boron complexes **7-9** in the ground state (left) and in the first excited singlet state (right), with the most relevant distances (Å).

Computational studies – Frontier orbitals and composition of the lower energy electronic transitions in boron complexes **4** and **6**

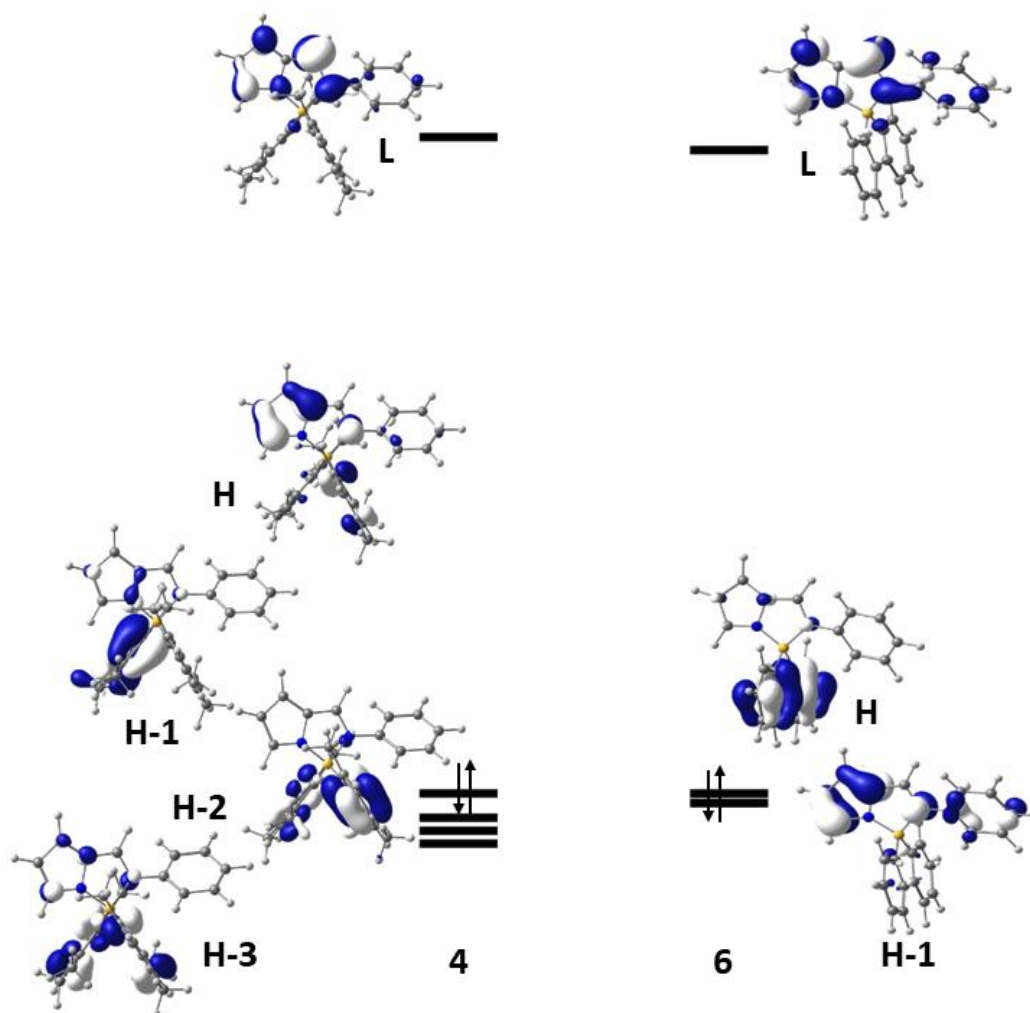


Figure S36. Three-dimensional representation of the frontier orbitals of mononuclear complexes **4** and **6** with relative energies (HOMO-LUMO gap: 4.24 (**4**), 3.71 (**6**) eV; the HOMO is identified by the arrows).

Computational studies – Calculated HOMOs and LUMOs energies for complexes 3-9 using different methods

Table S5. Calculated HOMOs and LUMOS energies (eV) for complexes **3-9** using different methods.

	A		A/D3		B		B/D3		GP		THF		CH ₂ Cl ₂	
	HOMO	LUMO	HOMO	LUMO	HOMO	LUMO	HOMO	LUMO	HOMO	LUMO	HOMO	LUMO	HOMO	LUMO
3	-6.490	-2.443	-6.488	-2.441	-6.184	-2.489	-6.182	-2.485	-5.722	-3.390	-5.540	-3.143	-5.632	-3.243
4	-6.277	-2.033	-6.268	-2.014	-5.959	-2.068	-5.944	-2.045	-5.342	-2.978	-5.373	-2.827	-5.424	-2.886
5	-6.532	-2.470	-6.526	-2.472	-6.230	-2.522	-6.219	-2.526	-5.880	-3.519	-5.617	-3.188	-5.691	-3.263
6	-6.249	-2.156	-6.249	-2.158	-5.899	-2.179	-5.897	-2.180	-5.251	-3.082	-5.440	-2.944	-5.445	-2.987
7	-6.335	-2.793	-6.320	-2.800	-6.057	-2.822	-6.034	-2.832	-5.830	-3.900	-5.442	-3.459	-5.509	-3.521
8	-6.355	-2.097	-6.352	-2.095	-6.038	-2.145	-6.040	-2.124	-5.396	-2.933	-5.414	-2.877	-5.511	-2.978
9	-6.133	-2.410	-6.129	-2.424	-5.876	-2.392	-5.869	-2.392	-5.224	-3.213	-5.201	-3.123	-5.309	-3.232

A – PBE0, TZ2P (all electron), THF, SO

A/D3 – PBE0/D3, TZ2P (all electron), THF, SO

B – B3LYP, TZ2P (all electron), THF, SO

B/D3 – B3LYP/D3, TZ2P (all electron), THF, SO

GP – BP86 (small core, TZ2P)

THF – BP86 (small core, TZ2P), THF (single point)

CH₂Cl₂ – BP86 (small core, TZ2P), dichloromethane (single point)

Computational studies – Calculated absorption energies and first excited state lifetimes for complexes 3-9 using different methods

Table S6. Calculated absorption energies (eV) and first excited state lifetimes (ns) for complexes **3-9** using different methods.

	A		A/D3		B		B/D3		GP
	λ_{abs}^{max}	τ_f	λ_{abs}^{max}	τ_f	λ_{abs}^{max}	τ_f	λ_{abs}^{max}	τ_f	λ_{abs}^{max}
3	3.36	1.94	3.36	1.97	3.29	2.13	3.29	2.13	2.16
4	3.79	7.24	3.80	15.0	3.72	11.2	3.80	14.47	3.39
5	3.41	2.02	3.40	2.03	3.33	2.17	3.32	2.19	3.14
6	3.50	1.80	3.50	1.83	3.46	1.85	3.41	1.87	3.29
7	2.88	1.59	2.86	1.61	2.80	1.80	2.77	1.82	2.39
8	3.45	1.84	3.59	1.77	3.39	1.94	3.54	1.87	3.29
9	3.04	1.41	3.04	1.42	3.03	1.57	3.03	1.58	2.47

A – PBE0, TZ2P (all electron), THF, SO

A/D3 – PBE0/D3, TZ2P (all electron), THF, SO

B – B3LYP, TZ2P (all electron), THF, SO

B/D3 – B3LYP/D3, TZ2P (all electron), THF, SO

GP – BP86 (small core, TZ2P)

Computational studies – Composition of the lower energy electronic transitions in complexes 4 and 6

Table S7. Composition and oscillator strength (OS) of the lower energy electronic transitions in complexes 4 and 6.

Transition	λ (nm)	E (eV)	Composition	OS
Complex 4				
1	352	3.52	H→L (56%), H-1→L (36%)	0.107
2	347	3.57	H-1→L (62%), H→L (27%)	0.251
3	331	3.75	H-2→L (89%), H→L (8%)	0.150
4	317	3.91	H-3→L (90%), H→L (5%)	0.448
Complex 6				
1	374	3.31	H→L (96%)	0.033
2	354	3.50	H-1→L (94%), H→L (3%)	1.039

Computational studies – Calculated energies of $S_1 \rightarrow S_0$ transition for complexes 3-9 using different methods

Table S8. Calculated energies (eV) of $S_1 \rightarrow S_0$ transition for complexes **3-9** using different methods.

	S_1				
	A	B	A/D3	B/D3	GP
3	2.57	2.476	2.56	2.45	1.80
4	2.37	2.21	2.35	2.15	1.815
5	2.64	2.53	2.64	2.60	1.87
6	2.57	2.37	2.57	2.35	2.09
7	2.25	2.17	2.26	2.17	1.52
8	2.70	2.60	2.70	2.60	1.89
9	2.55	2.15	2.55	2.45	1.50

A – PBE0, TZ2P (all electron), THF, SO

A/D3 – PBE0/D3, TZ2P (all electron), THF, SO

B – B3LYP, TZ2P (all electron), THF, SO

B/D3 – B3LYP/D3, TZ2P (all electron), THF, SO

GP – BP86 (small core, TZ2P)

Electrochemical properties

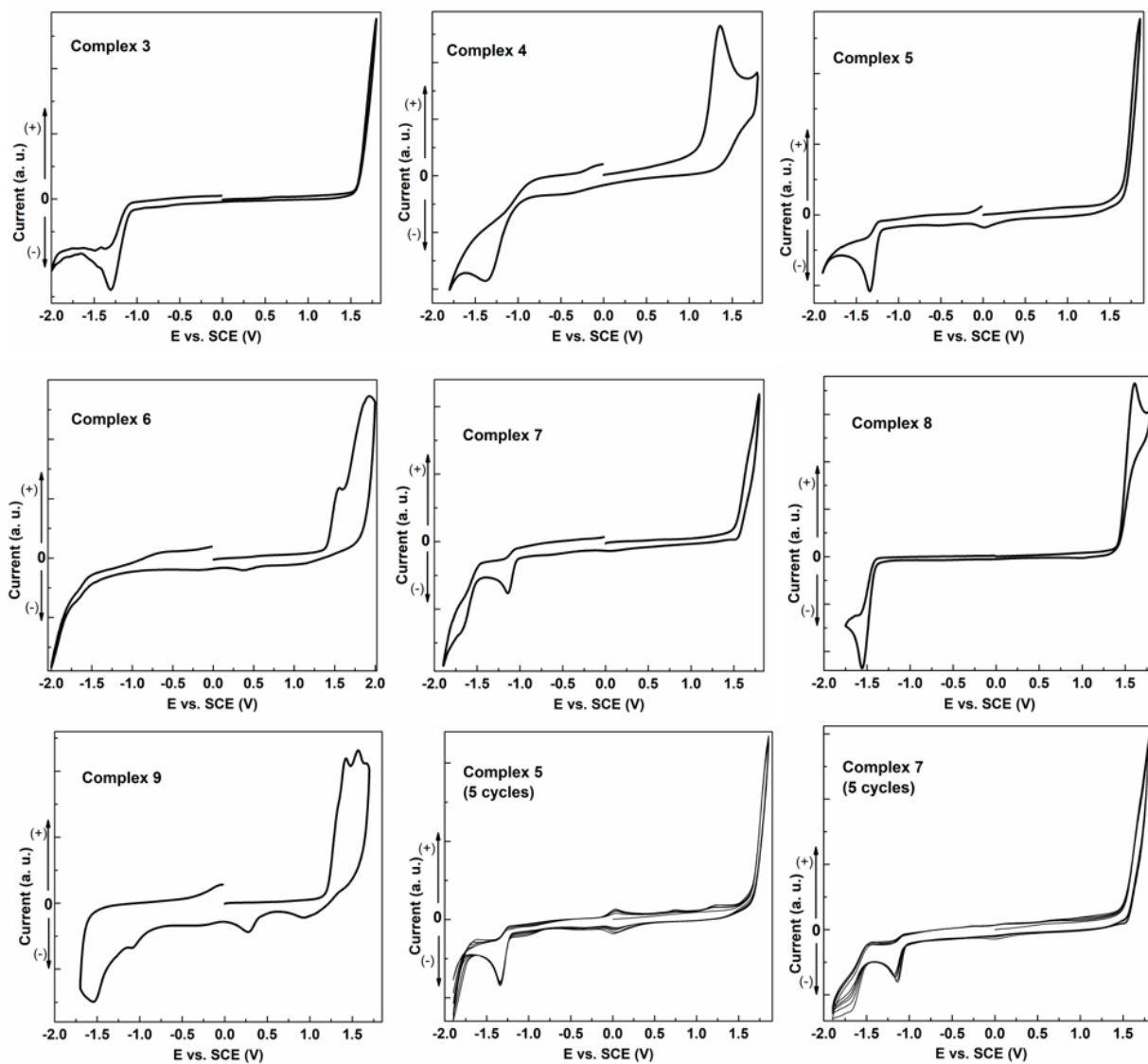
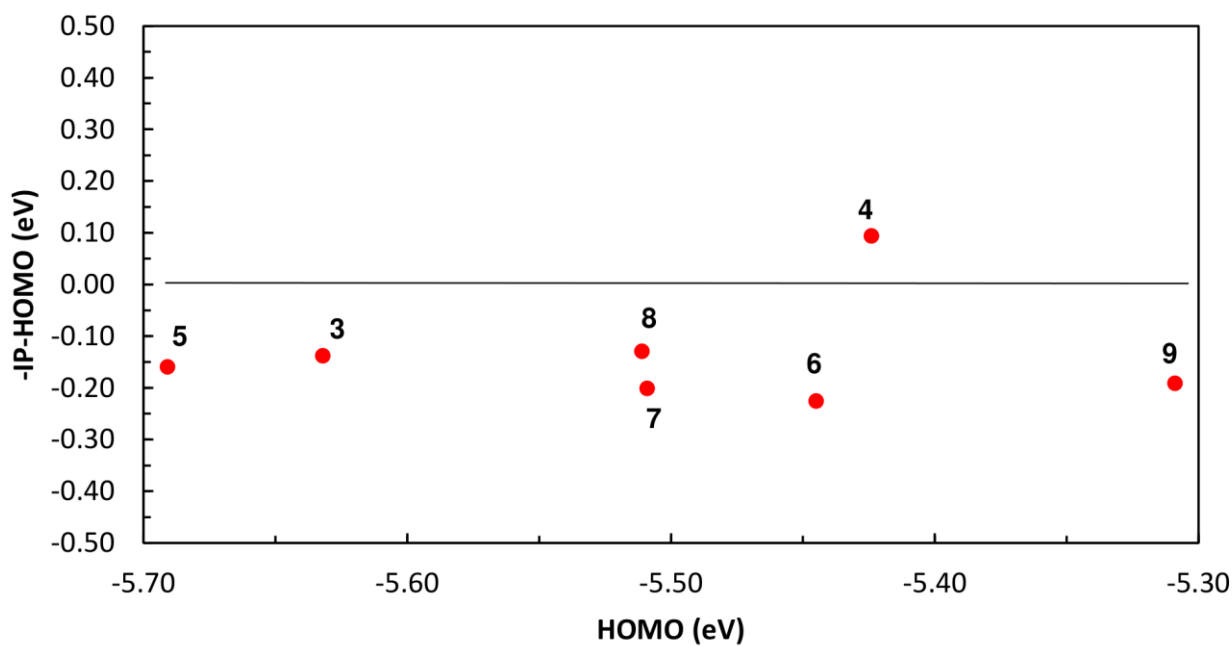
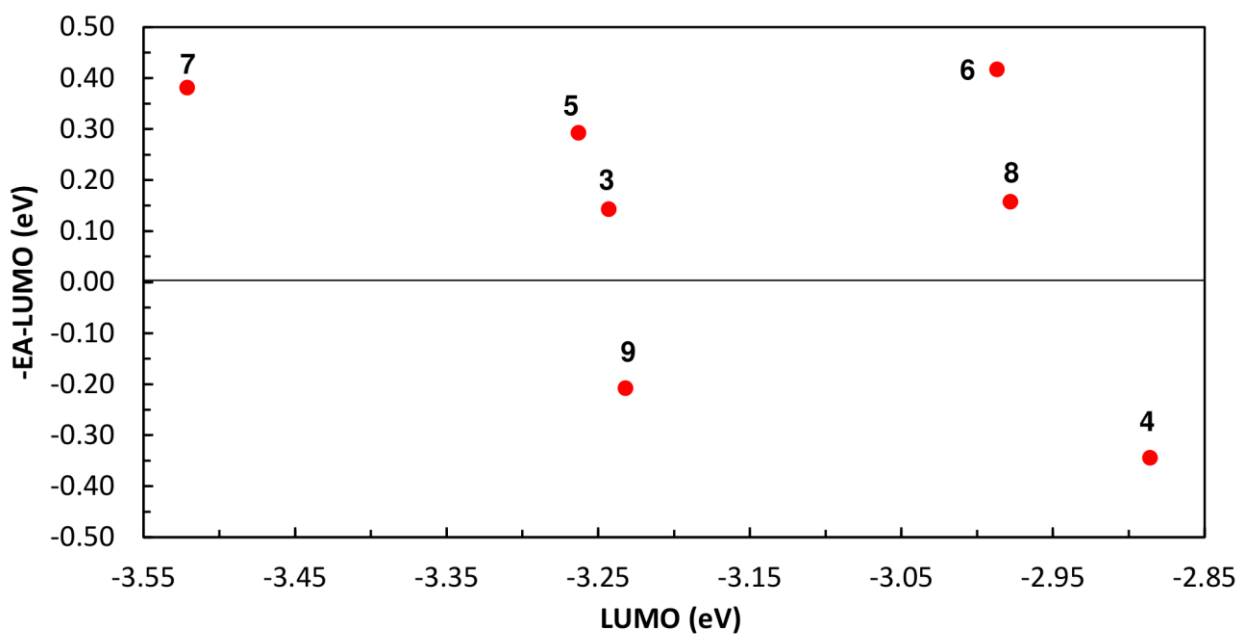


Figure S37. Cyclic voltammograms obtained for complexes **3-9** in this work, measured at scan rate of 50 mV/s in 0.1 M TBABF₄/CH₂Cl₂ (for complexes **3-8**) or 0.1 M TBAClO₄/CH₂Cl₂ (for complex **9**) as electrolytes.



(a)



(b)

Figure S38. Plots of (a) the difference between $-IP$ and HOMO versus the energies of the HOMOs, and of (b) the difference between $-EA$ and LUMO versus the energies of the LUMOs of compounds **3–9**. IP and EA were estimated from cyclic voltammetry measurements, and the energies of the HOMOs and LUMOs were determined by DFT (CH_2Cl_2).

Electroluminescence performance

Table S8 summarises the performance parameters of the various OLEDs fabricated with the new complexes deposited by spin coating. It also includes the previously reported results for the OLEDs based on neat **8** and **9**.

OLEDs based on neat complexes **3** and **4** showed negligible emission, a result consistent with the low or null photoluminescence (PL), and were not further investigated. Devices based on neat complex **5** showed also negligible emission. In view of the reasonable PL efficiency this was further studied in OLEDs upon dispersion in polyvinylcarbazole (PVK).

We also observed that films of neat complex **7** showed signs of crystallization, leading to rough surfaces.

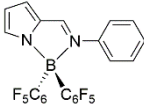
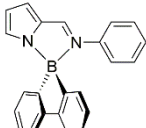
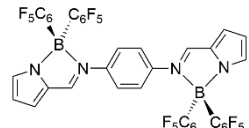
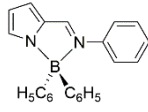
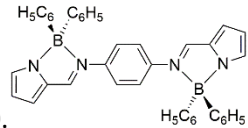
Figure S39 compares the recorded EL spectra for neat complexes and for the complexes dispersed in PVK with the corresponding PL spectra. A good agreement is observed. Small differences are likely due to interference effects inside the OLEDs (which resemble a microcavity). No additional peaks are observed in EL that could result from degradation or from lower energy emissive states (such as aggregates).

In view of the close molecular structure of complexes **7** and **9**, the similar solution fluorescence quantum yield, and the above mentioned tendency of crystallization of complex **7** films, we investigated the performance of OLEDs based on a 1:1 weight mixture of the two complexes. The devices had the structure ITO/PEDOT:PSS/**7+9**/Ca/Al, with a pixel area of 8 mm² and the active layer thickness (**7+9**) of *ca.* 60 nm. Figure S40 compares the performance of these devices with those of the neat complexes.

We found that the OLEDs combining the two complexes do not outperform that of the OLEDs based on neat **9**. The typical maximum luminance of the OLEDs based on the **7+9** mixture, 27 cd m⁻², is lower than those of the OLEDs based on neat **7** (43 cd m⁻²) or **9** (958 cd m⁻²), and the current efficiency (as shown in Fig S40B) is slightly higher than that of neat **7**-based OLEDs, but significantly lower than that of the neat **9**-based OLEDs. We found, however, that the film of the mixture is quite homogeneous, without crystallization signs, which is probably the reason why the current shows a smoother variation with the applied voltage when compared with that of neat **7**-based OLEDs. The EL spectra for the three devices structures are very similar, as shown in Figure S40C).

It should be mentioned that OLEDs based on the dispersion of this **7+9** mixture in PVK do not show improved performance (maximum luminance of 14 cd m⁻², maximum electroluminescence efficiency of 0.010 cd A⁻¹).

Table S9. Electroluminescence data for OLEDs prepared by spin coating of either THF solutions of the neat complexes or THF solutions of the complexes mixed with PVK. The general OLEDs structure was ITO/PEDOT:PSS/active layer/Ca/Al. Devices containing an interlayer (IL) of polyTPD, between PEDOT:PSS and the active layer, were also fabricated and tested. Pixel areas were 8 mm², except for some identified cases, where a 4 mm² area was used.

	5	6	7	8	9
					
ϕ_{r} (THF solution)	0.32	0.40	0.32	0.34 ^b	0.36
ϕ_{PL} (ZEONEX film)	0.31	0.40	0.31	0.37	0.36
Neat complexes	Negligible	$L^{\text{max}}=10 \text{ cd m}^{-2}$ $\phi_{\text{EL}}^{\text{max}}=0.003 \text{ cd A}^{-1}$ $\text{EQE}^{\text{max}}=0.001 \%$ $\text{EL}^{\text{max}}=485 \text{ nm}^a$	$L^{\text{max}}=43 \text{ cd m}^{-2}$ $\phi_{\text{EL}}^{\text{max}}=0.013 \text{ cd A}^{-1}$ $\text{EQE}^{\text{max}}=0.004\%$ $\text{EL}^{\text{max}}=564 \text{ nm}^a$	$L^{\text{max}}=0.35 \text{ cd m}^{-2}$ $\phi_{\text{EL}}^{\text{max}}=3.8 \times 10^{-4} \text{ cd A}^{-1}$ $\text{EQE}^{\text{max}}=1.5 \times 10^{-4} \%$ $\text{EL}^{\text{max}}=490 \text{ nm}^{a,b}$	$L^{\text{max}}=958 \text{ cd m}^{-2}$ $\phi_{\text{EL}}^{\text{max}}=0.30 \text{ cd A}^{-1}$ $\text{EQE}^{\text{max}}=0.084\%$ $\text{EL}^{\text{max}}=531 \text{ nm}^{a,c}$
PVK + 4% complexes	$L^{\text{max}}=79 \text{ cd m}^{-2}$ $\phi_{\text{EL}}^{\text{max}}=0.087 \text{ cd A}^{-1}$ $\text{EQE}^{\text{max}}=0.032\%$ $\text{EL}^{\text{max}}=502 \text{ nm}$	$L^{\text{max}}=41 \text{ cd m}^{-2}$ $\phi_{\text{EL}}^{\text{max}}=0.0065 \text{ cd A}^{-1}$ $\text{EQE}^{\text{max}}=0.0029 \%$ $\text{EL}^{\text{max}}=483 \text{ nm}$	$L^{\text{max}}=31 \text{ cd m}^{-2}$ $\phi_{\text{EL}}^{\text{max}}=0.020 \text{ cd A}^{-1}$ $\text{EQE}^{\text{max}}=0.0065\%$ $\text{EL}^{\text{max}}=524 \text{ nm}$	-	$L^{\text{max}}=94 \text{ cd m}^{-2}$ $\phi_{\text{EL}}^{\text{max}}=0.0281 \text{ cd A}^{-1}$ $\text{EQE}^{\text{max}}=0.0092\%$ $\text{EL}^{\text{max}}=522 \text{ nm}$
polyTPD_IL/PVK + 4% complexes	$L^{\text{max}}=31 \text{ cd m}^{-2}$ $\phi_{\text{EL}}^{\text{max}}=0.025 \text{ cd A}^{-1}$ $\text{EQE}^{\text{max}}=0.0093\%$ $\text{EL}^{\text{max}}=498 \text{ nm}$	$L^{\text{max}}=170 \text{ cd m}^{-2}$ $\phi_{\text{EL}}^{\text{max}}=0.037 \text{ cd A}^{-1}$ $\text{EQE}^{\text{max}}=0.016\%$ $\text{EL}^{\text{max}}=485 \text{ nm}$	$L^{\text{max}}=40 \text{ cd m}^{-2}$ $\phi_{\text{EL}}^{\text{max}}=0.0074 \text{ cd A}^{-1}$ $\text{EQE}^{\text{max}}=0.0023\%$ $\text{EL}^{\text{max}}=524 \text{ nm}$	-	$L^{\text{max}}=124 \text{ cd m}^{-2}$ $\phi_{\text{EL}}^{\text{max}}=0.026 \text{ cd A}^{-1}$ $\text{EQE}^{\text{max}}=0.0085\%$ $\text{EL}^{\text{max}}=522 \text{ nm}$

^a Pixel area of 4 mm²; ^b Ref. 11c; ^c Ref. 11d

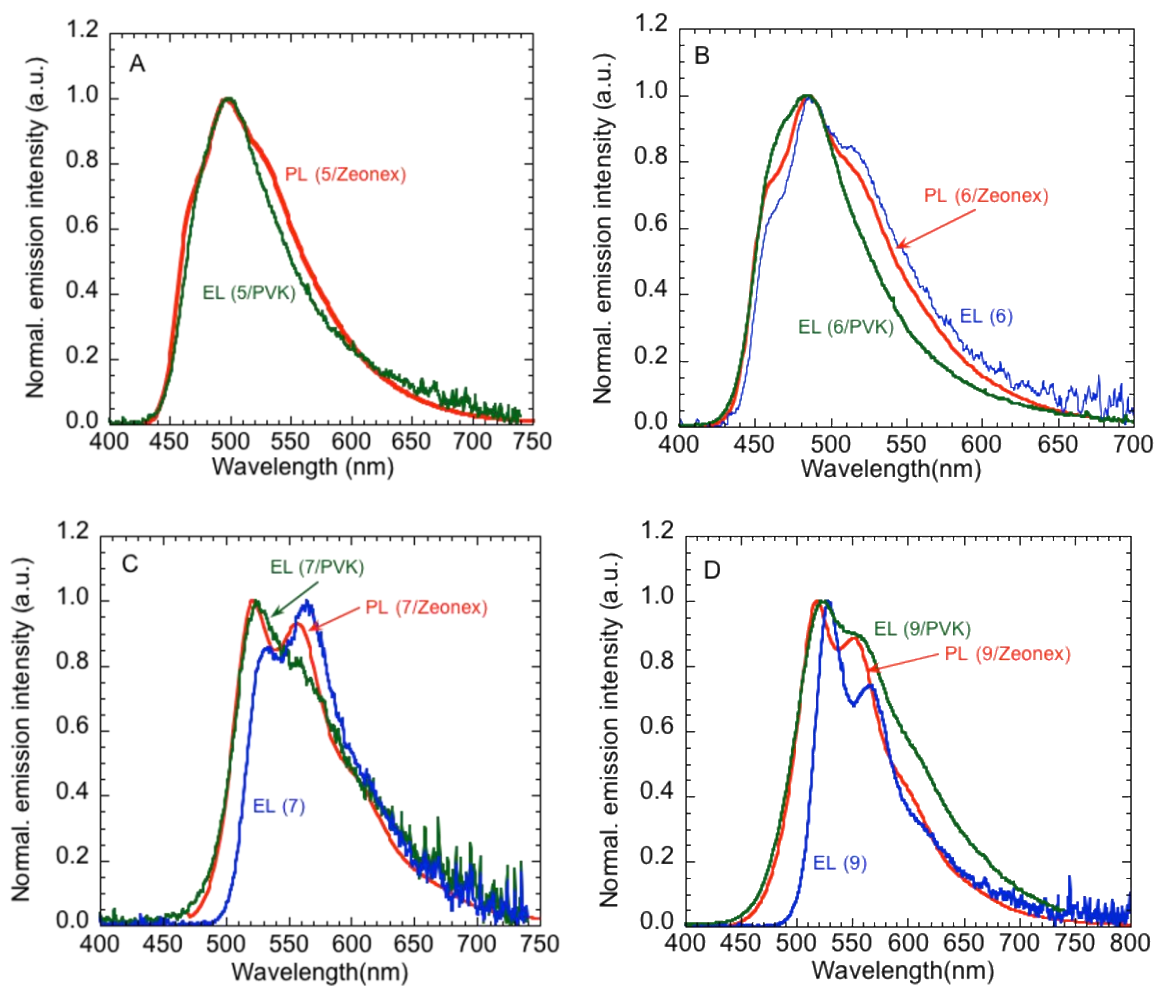


Fig. S39. Comparison between the EL spectra recorded from the OLEDs based on active layers made of both the complexes dispersed in PVK and the neat complexes and the PL spectra recorded for the complexes dispersed in ZEONEX.

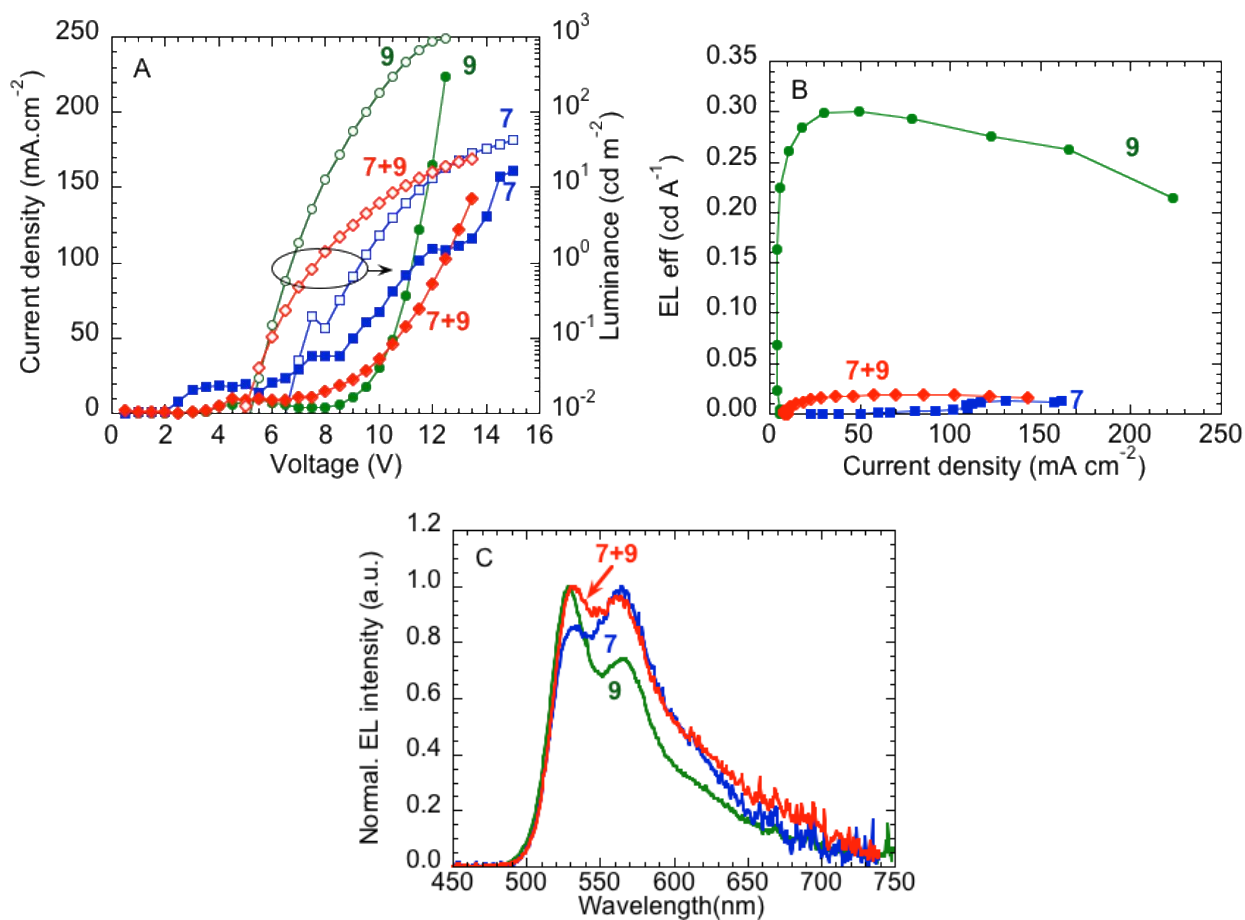


Fig. S40. Characteristics of the OLEDs based on neat complexes **7** and **9** with those of the OLED based on their mixture. A) Current density (closed symbols) and luminance as a function of the applied voltage; B) Electroluminescence efficiency as a function of the current density in the devices; and C) EL spectra.